



HAL
open science

New physical insights on time periodic systems: from extreme parametric resonance to synchronized dynamic stabilization

Alvaro Anzoleaga Grandi

► **To cite this version:**

Alvaro Anzoleaga Grandi. New physical insights on time periodic systems: from extreme parametric resonance to synchronized dynamic stabilization. Structural mechanics [physics.class-ph]. Sorbonne Université, 2022. English. NNT: 2022SORUS303. tel-03888989

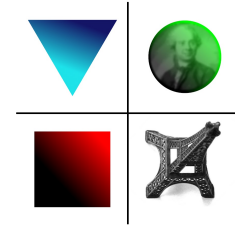
HAL Id: tel-03888989

<https://theses.hal.science/tel-03888989>

Submitted on 7 Dec 2022

HAL is a multi-disciplinary open access archive for the deposit and dissemination of scientific research documents, whether they are published or not. The documents may come from teaching and research institutions in France or abroad, or from public or private research centers.

L'archive ouverte pluridisciplinaire **HAL**, est destinée au dépôt et à la diffusion de documents scientifiques de niveau recherche, publiés ou non, émanant des établissements d'enseignement et de recherche français ou étrangers, des laboratoires publics ou privés.



Sorbonne Université

Ecole Doctorale 391 : Sciences Mécaniques, Acoustique, Electronique et Robotique

Thèse de Doctorat

Présentée par

Alvaro Anzoleaga Grandi

Pour obtenir le grade de

Docteur de Sorbonne Université

New physical insights on time periodic systems: from extreme parametric resonance to synchronized dynamic stabilization

Sous la direction de

Arnaud Lazarus & Suzie Protière

à l'Institut Jean le Rond d'Alembert, Sorbonne Université, CNRS, UMR7190

Devant le jury composé de :

Emmanuel Fort	Professeur à ESPCI	Rapporteur
Cyril Touzé	Professeur à ENSTA Paris	Rapporteur
Claude-Henri Lamarque	Professeur à ENTPE	Examineur
Sébastien Neukirch	Directeur de recherche CNRS	Examineur
Finn Box	Professeur assistant Manchester University	Examineur
Suzie Protière	Chargée de recherche CNRS	Directrice de thèse
Arnaud Lazarus	Maître de conférence à Sorbonne Université	Directeur de thèse

ACKNOWLEDGEMENT

In every challenging adventure, the main protagonist cannot do it alone. They always need help, advice, comfort or sometimes just a warm beverage from the people who care about them. This section is my opportunity to honor and acknowledge the people who helped me during *my adventure*.

First, I want to thank my two advisors: Arnaud Lazarus & Suzie Protière. They are two of the most engaged and nice people I had the pleasure to meet. They were always available in times of need and during complicated situations they were always relaxed and understanding. Every meeting we had they passed me their love for science, their good attitude when things did not work (specially when a new experiment was built), their willingness to push a problem and only called it "finished" if we can explain it in a "simple" way. But the most important thing they taught me is to enjoy my scientific journey and appreciate the grain of sand we are bringing to the ocean that is time periodic systems. Secondly, I want to thank my colleagues, the administrative team of the lab and the friends I made in my staying in France. The life in this laboratory was one of a kind. People from all over the world converged into this lab and we created a very unique vibe that I am glad to have been able to experience. Every discussion I had either helped me to improve my scientific knowledge or to have a good laugh. In my books, both are equally important. I want to specially thank: Nicolas Baranowski (El Polaco) and Mahshid Sharifi. They both are very special people who I am lucky to have met and developed an honest friendship which I am sure will last for all of our lives.

Next, undoubtably, I want to thank my parents (Evelyn Grandi & Patricio Ocampo) and my brother Alejandro A. Grandi. Ma y Pato siempre estuvieron para mí y les agradezco eternamente todo lo que hicieron por mí y para que yo pueda llegar donde estoy. Son una gran inspiración para mí. Con ustedes aprendí que el trabajo duro siempre da frutos y nunca hay que bajar los brazos. Este manuscrito y mi vida son la prueba constante que eso es verdad. Ale, tú siempre estuviste para mí desde que era pequeño y no me imagino poder llegar hasta a este punto de mi vida sin todos tus consejos y ayuda. Tú fuiste la persona que me enseñó que ningún sueño es imposible y que siempre confíe en mí. Gracias por siempre ayudarme y aconsejarme de la manera más honesta que vi en mi vida.

Finally, the last person I want to acknowledge is Ana-Luna Py. Eres la persona que vivió conmigo toda esta aventura y estoy inmensamente agradecido por tu apoyo, consejos, comprensión, sonrisas, cariño, cocinadas y sentido del humor que tuviste en mis momentos de estrés máximo (throwback a Lyon 2022). Este manuscrito y trabajo es tanto mío como tuyo. Gracias por ser como eres y ser parte de mi vida.

ABSTRACT

In this thesis we bring new physical insights in parametric instabilities that can occur in dynamical systems with a natural cycle which natural time scale could be periodically modulated. Our approach is based on the development of experimental and theoretical proofs of concept.

In a first part, we study parametric instabilities as parametric amplifiers. We develop a new experimental setup at the macroscopic scale to go beyond the tip of the instability tongues. As a result of experimental and numerical observations, a geometrical design rule is developed to control high order parametric instabilities. This geometrical design is experimentally validated, and high order parametric instabilities are triggered and observed. Finally, by changing the shape of the modulation function, we show that it is possible to use parametric instabilities to trigger and sustain the natural oscillation of a dynamical system.

In the second part, we revisit the concept of dynamic stabilization. An experimental and numerical proof of concept is developed to show that it is possible to stabilize a system with a driven frequency closer to the natural time scale of a naturally diverging system and even go over the first stability region, unlike the classic Kapitza approach. By way of a numerical study, we show that we can dynamically stabilize a system by synchronizing the period of modulation to its natural time scales. However, this region is difficult to observe with the classical stability analysis. To access it in a simpler way, we pass by an analogy between initial and boundary value problem and this way develop pseudo-analytical master curves to predict dynamical stabilization. Finally, these pseudo-analytical solutions are validated by experimental observations.

Keywords:

Parametric instabilities, dynamical systems, instabilities for functionalities, dynamical stabilization, parametric oscillators

RÉSUMÉ

Dans cette thèse, nous apportons de nouvelles connaissances physiques dans le domaine des instabilités paramétriques qui peuvent survenir dans des systèmes dynamiques dont les échelles de temps naturelles sont périodiquement modulées. Notre approche se base sur des preuves de concept théorique et expérimentale.

Dans une première partie, nous développons un nouveau setup expérimental (à l'échelle macroscopique) pour aller au-delà de la pointe des langues d'instabilité. Grâce aux observations expérimentales et à un modèle numérique associé, une règle de conception géométrique est déduite pour contrôler les instabilités paramétriques d'ordre élevé. Cette conception géométrique est validée expérimentalement, et des instabilités paramétriques d'ordre élevé sont déclenchées et observées. Finalement, en changeant la forme de la modulation, nous montrons qu'il est possible d'utiliser les instabilités paramétriques pour déclencher et maintenir les oscillations naturelles d'un système dynamique.

Dans la deuxième partie, nous revisitons le concept de stabilisation dynamique. A partir d'une preuve de concept expérimentale et numérique, nous observons qu'il est possible de stabiliser un système avec une fréquence de modulation plus proche de l'échelle de temps naturelle du système et même d'aller au-delà de la première région de stabilité, contrairement à l'approche classique dite de Kapitza.

Avec une étude numérique, nous montrons que nous pouvons stabiliser un système en synchronisant simplement la fonction de modulation avec les échelles de temps naturelles du système à stabiliser. Cependant, cette limite asymptotique est difficile à observer avec l'analyse classique de stabilité de système dynamique. Pour y accéder de manière plus simple, nous faisons l'analogie entre problème aux conditions initiales et problème aux limites et développons ainsi des courbes maîtresses pseudo-analytiques pour prédire cette stabilisation dynamique synchronisée. Finalement, ces solutions théoriques sont validées par des observations expérimentales.

Mots clés:

Instabilités paramétriques, système dynamique, instabilités pour des fonctionnalités, stabilisation dynamique, oscillateur paramétrique

CONTENTS

Introduction	1
1 Beyond the tips of the parametric instabilities tongues	15
1 Rationalizing parametric instabilities in a variety of experimental systems	16
1.1 The parametric pendulum: the classical example of a parametric system	17
1.2 Faraday waves, the pioneer of parametric instabilities	19
1.3 Microscopic example: Micro Electro Mechanical Systems	21
1.4 Discussion	22
2 Going beyond the tip of the parametric instability regions	24
2.1 Experimental setup	25
2.2 Characterization of the system	26
2.3 Experimental observation of extreme parametric instabilities	29
3 Controlling high order parametric instabilities	33
3.1 Rationalizing the instability regions for a square wave modulation	33
3.2 Triggering and sustaining a natural oscillation	39
	46
2 Anti-resonance tongues: stabilising in synchrony a naturally unstable system	47
1 Physical framework: systems with a naturally unstable equilibrium	49
1.1 Linear stabilization using parametric modulations	49
2 Classical attempts to stabilize a natural equilibrium system using parametric modulations	51
2.1 Macroscopic example: inverted pendulum	51
2.2 Microscopic example: Ion trap	53
2.3 Discussion	55
3 Experimental stabilization beyond the Kapitza approach	56
3.1 Experimental setup	56
3.2 Experimental stabilisation	61
4 Numerical study of the tip of the stability regions	64
4.1 Basin of attraction	64
4.2 Study of the responses	65
4.3 Resolution in a unit cell	67
5 Pseudo-analytical solutions at the tip of the stability tongue	69

5.1	Analog problem	69
5.2	Pseudo-analytical solutions near the tip of the stability tongue . . .	72
5.3	Re-introducing the second time scale to the master curves	73
6	Experimental validation of the master curves: synchronized dynamical stabilization	75
6.1	Experimental stabilization at $T_D = 25\%T$	76
6.2	Experimental stabilization at $T_D = 70\%T$	77
		80
3	Conclusions & perspectives	81
	Bibliography	91

INTRODUCTION

A dynamical system consists of two main components: a starting point or initial “state” and a specific rule or “dynamics” which describes its evolution through time. The most successful types of rules to describe physical phenomena are differential equations. We are particularly interested in the family of dynamical systems which have a natural time scale that can be periodically modulated. This family of system is extensive: trapping and levitating particles, a child on a swing, the sinking of ships, cardiac rhythms, or business cycles, just to name a few.

Depending on the system, the periodic modulation can do two things: either amplifying the motion of the system at rest, this is parametric resonance, or decreasing existing high amplitudes of motion and make it steady, this is dynamical stabilization. Both functionalities have been studied and implemented in this family of dynamical systems. However, as any physical phenomenon, there is still a lot to be studied. In this manuscript, we will show that there still exist limitations to their implementations at the macroscopic scale and we will provide new physical insights on how we can overcome these limitations and extend our use of parametric instabilities for functionalities.

A brief history of dynamical systems and instabilities

The subject of dynamical systems was introduced in the mid-1600s when Newton invented differential equations, discovered his laws of motion, universal gravitation and combined them to solve the problem of calculating the motion of the Earth around the Sun, solving the two-body problem [1]. Trying to translate his theory to the three-body problem did not give the same results and for years the three-body problem was thought impossible to solve until the late 1800s with Henri Poincaré. Poincaré realised this problem was essentially impossible to solve in the sense of obtaining explicit formulas for the motions of the three bodies. Instead of focusing on the explicit formulas and doing the usual quantitative approach, he proposed a qualitative approach focusing on the global stability behaviour of the system [2]. Poincaré’s novel qualitative approach introduces the notion of phase portrait. A phase portrait is a geometric representation of the trajectories of a dynamical system in the phase space and each set of initial conditions is represented by a different curve, or point [2, 3]. The study of these different trajectories helps deduce important properties of the system. For example Fig 1.a showcases the phase portrait of an undamped pendulum defined by $\ddot{\theta}(t) + \omega_0^2 \sin \theta(t) = 0$. For some initial conditions the trajectories are circles, these circles correspond to the oscillatory motion of a pendulum. If the initial conditions surpass a certain limit, the trajectories show how the pendulum will lose the oscillatory motion and how it will continuously turn through the vertical planar circle. Besides describing the motion of

the system, the phase portrait showcases the different equilibrium points of the system and gives the nature of each one. When one or more trajectories converge to a given equilibrium, this equilibrium is said stable (blue dots in Fig 1.a). On the contrary, if the trajectories are escaping the equilibrium point, that equilibrium is said to be unstable (red dots in Fig 1.a). At higher dimensions in the phase space, new behaviours can appear in the system. For example Fig 1.b shows a dynamical system with a chaotic behaviour, the famous Lorenz attractor [4]. The Lorenz attractor is obtained with the Lorenz equations which are a three-dimensional simplified model of convection rolls in the atmosphere. This simple-looking deterministic system has extremely erratic dynamics: the trajectories oscillate irregularly, never exactly repeating but always remaining in a bounded region of the phase space. This bounded region is a strange attractor (the first one ever observed) and it is represented in Fig 1.b.

These are some examples of the versatility and importance of Poincaré's approach. Besides introducing this novel qualitative (geometrical) theory to study differential equations, he developed the basis for the local and global analysis of nonlinear differential equations and the importance of the sensitivity to initial conditions of the behaviour of a deterministic system (possibility of chaos). These ideas are considered the cornerstone of the interdisciplinary study of today's dynamical systems. Because of the importance of his work and their applications, Henri Poincaré is recognised as the true founder of the study of dynamical systems [5, 6].

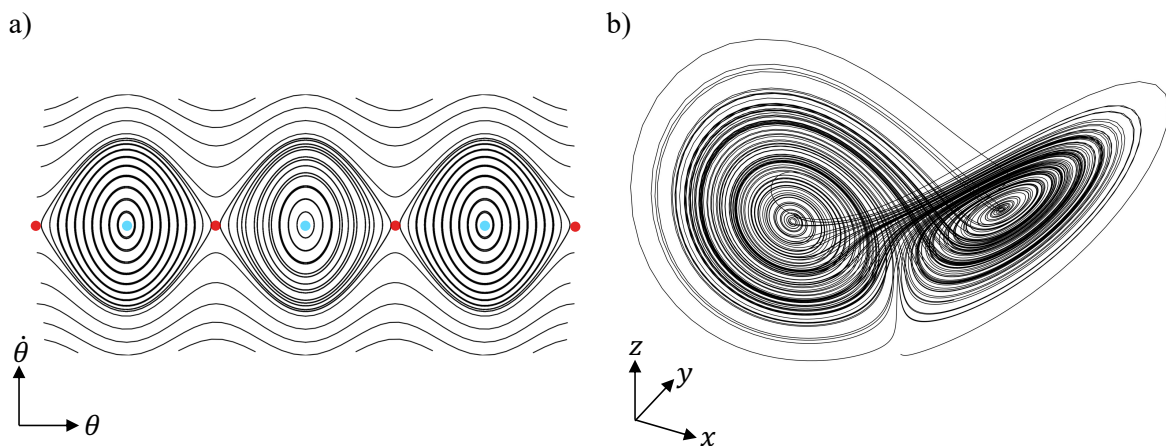


Figure 1: Examples of a qualitative study of dynamical systems a) Two dimensional phase portrait of the dynamical motion of a pendulum showcasing stable and unstable equilibrium points in blue and red respectively. b) Three-dimensional phase portrait of the first strange attractor, the Lorenz attractor.

On a day-to-day basis nobody likes unpredictable events. If you go to the doctor for your yearly check-up, you never want them to find an unexpected black mass. Or if you study for an exam, you do not want to be the one the teacher asks his famous questions out of topic just to see if you really understood the lesson. No, you expect everything to go according to plan. Physics and engineering are not the exception. We want to prevent any unpleasant surprise. And in a system the source of an unpredictable behaviour is often an instability. For example one classical example of an instability can be the buckling of a beam or shell: if a slender structure is under some important constraint (compression, tension or thermal

effects) the system can buckle making the structure unstable and dangerous [7]. The repercussions of these phenomena are catastrophic and can lead to the destruction of the entire system. A storage tank collapsed because of a buckling instability induced by the pressure inside the tank (Fig 2.a). Another example to show the danger of instabilities can be the fall of the Tacoma Narrows bridge in 1940 [8]. The Tacoma Narrows bridge in Washington state was at the time the lighter and one of most flexible bridges in the world. The one of a new set of bridges to be build. However, the 7th of November 1940 a strong wind put the bridge into a series of torsional oscillations. The amplitude of the oscillations steadily increased until the convolutions tore several suspenders and the span broke up, resulting in the complete collapse of the bridge (Fig 2.b).

One last example of the fatalities of instabilities can be seen in the navy, more specifically in the transport of large container ships. The 9th of October 2011, the container ship MV RENA, which can carry a capacity of 3351 containers and has an approximative length of 236 meters and a depth of 18.8 meters, experienced periodic high amplitude rolls over 20° while sailing from Napier to Tauranga (northern coast of New Zealand). This high amplitude coupled with an unfavourable periodicity of the waves made the system unstable and several containers collapsed (Fig 2.c). This incident provoked the breaking in half of the ship, the loss of 88 containers and the leak of 130 to 350 tonnes of oil, declaring it as New Zealand's worst ever maritime environmental disaster [9, 10].



Figure 2: Examples of the risk of instabilities a) Buckling of liquid storage tanks under uniform pressure at Penuelas, Puerto Rico. Image credit: Luis A. Godoy [7]. b) Collapsing of the Tacoma Narrows bridge due to strong winds. Image credit: The United State Government, retrieved from the data of the 7th of November 1940. c) MV Rena cargo ship broken in half and loss of containers due to the periodicity and high amplitude of the waves. Image credit: Maritime New Zealand.

To work around these problems and avoid any instability to appear we had to study them. One of the most important theories to study buckling was introduced at the end of the 18th century, the Euler-Bernoulli theory [11]. Ignoring the effects of shear deformation and rotary inertia, this theory let us calculate the load-carrying and deflection characteristics of beams. Since then, various models were introduced but one of the major improvements of the Euler-Bernoulli theory was developed by Timoshenko in the 1920s [12, 13]. The Timoshenko model proposed a beam theory taking in consideration shear as well as the effect of rotation to the Euler-Bernoulli theory, making it applicable for slender and non-slender beams and for high-frequency responses where rotary effects or shear are not negligible.

The Euler-Bernoulli and Timoshenko theories for the dynamics of beams and shells are used widely in engineering [14, 15, 16, 17] and thus the buckling of storage tanks can now be avoided. However, the cause of the collapse of the Tacoma bridge was a topic of debate and confusion for years [8, 18]. After further studies it was understood that the cause of the instability was aeroelasticity which is the coupling between aerodynamics and elastic forces on deformable bodies subject to a flow [19]. This field of research has been vastly applied in aerospace engineering [20]. For instance, to avoid the flutter instability, composite materials are used as a better alternative to build the structures [21, 22].

Finally, the example of the rolling of a ship was thought as a resonance case but the actual reason of this instability is the amplitudes and the timing of the waves which modulate the metacentric height of the ship (distance between the centre of gravity of a ship and its metacentre, a measurement of the initial static stability of a floating body). The vessel will roll over to one side but when the wave reaches the middle of the ship, the increased stability will push the vessel quickly to its upright position. At this point the wave's crest reaches the middle of the ship again and the metacentric height value is again reduced which results in rolling the vessel in the opposite direction. Provided that few consecutive waves will be of the same length the vessel will develop a parametric resonance. To avoid it, areas of navigation investigated where parametric rolling is important [23, 24], and different numerical and experimental works have been conducted to avoid parametric rolling [25, 26].

Towards the end of the 20th century, the study of instabilities started to focus on how they can be used to bring new functionalities in mechanical systems. Buckling can be used to adapt the characteristics of different systems and provide new mechanical properties [27, 28, 29, 30]. For example it can bring robustness to a structure [31, 32] or on the contrary the use of a buckling-induced kirigami on a sheet can provide stretchability and higher bending rigidity [33] (Fig 3.a). Another important method to use instabilities as a functionality are geometrical re-organization systems, for example shape-morphing structures [34, 35, 36, 37]. A morphable structure is a system capable of changing shape to improve its performances or enable new functions. The action to modify the structure can be of many sorts. For example Siefert et al. [38] can control complex shape transformations using buckling transitions in elastomers under pressure (Fig 3.b).

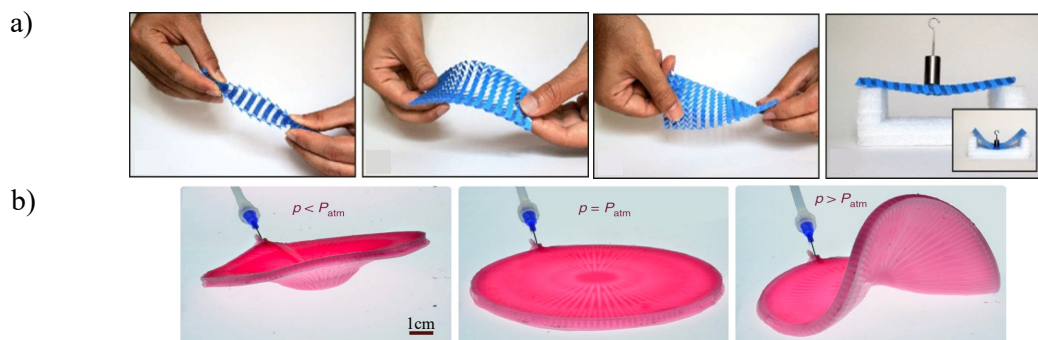


Figure 3: Examples of instabilities for functionalities a) Buckling-Induced Kirigami increases stretchability and higher bending rigidity. Image credit: Rafsanjani [33]. b) 3D shape-morphing elastomers induced by pressure. Image credit: Siefert [38].

Geometrical re-organization and controlled buckling are not the only candidates to exploit instabilities. Controlling parametric instabilities can also lead to exploiting them. They can be used as parametric resonance for example to trigger and sustain the motion of a system [39], or as dynamical stabilization for example to suppress aeroelastic flutter [40] or in mass spectrometry [41]. For example, Fig 4.a shows a linear electrodynamic Ion Trap where charged molecules are trapped along a central line by sending a dc voltage which is then periodically modulated by a precise rf voltage at a particular frequency. Finally, parametric instabilities have even been used to observe analogies between quantum mechanics and the macroscopic scale: waves formed spontaneously when a bath of liquid is vibrated periodically offers a new framework to study a particle-wave interaction at a macroscopic scale. Indeed, drops placed on such a bath form “dual walkers” which enable the study of classical orbits [42, 43] or the phenomenon of interference [44] (Fig 4.b).

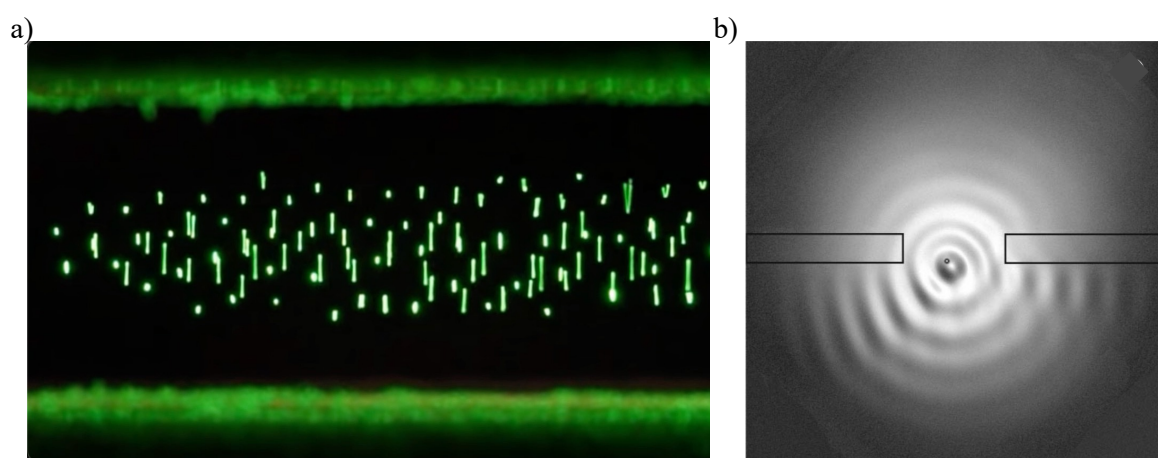


Figure 4: Examples of parametric instabilities for functionalities. a) Photograph of charged particles trapped by periodically modulating the electric field surrounding them. Image credit: Newtonian Labs [45]. b) Photograph of a droplet in a vertically vibrated bath (a “walker”) showing how its trajectory is deflected by the interference with reflected waves. Image credit: Y. Couder [44].

Parametric instabilities

Parametric instabilities occur in a dynamical system whose natural time scales are periodically modulated in synchrony with one of its natural time scales [46]. The first experimental observation of parametric instabilities was made by M. Faraday in 1831 [47]. His experiment consisted in creating a surface wave spontaneously in fluids by vertically vibrating a layer of a fluid on top of a membrane. Since then, parametric instabilities were observed in a plethora of dynamic systems, at the macroscopic scale [48, 49] and the microscopic scale [39, 50].

The most frequent equation to study them is a linear second order differential equation with periodic coefficient that reads

$$\frac{d^2y(\tau)}{d\tau^2} + (\alpha^2 + \beta^2 g(\tau)) y(\tau) = 0, \quad (1)$$

where α^2 represents a constant portion of the coefficient of y , β^2 accounts for the magnitude of the time variation and $g(\tau) = g(\tau + \mathcal{T})$ expresses the \mathcal{T} -periodic modulation function. Eq (1) is most commonly known as Hill's equation [51, 52] and can be found in a plethora of physical examples. The periodic modulation function $g(\tau)$ can be of any shape. The most known example is when $g(\tau)$ is a harmonic modulation, i.e $g(\tau) = \cos(\tau)$. In this case Eq (1) is known as Mathieu equation in reference to Emile Mathieu who theoretically showed in 1868 that the surface waves in elliptic-shaped lakes are governed by an ordinary differential equation (ODE) with periodic coefficients [48]. Another important contribution in the domain of parametric instabilities was done by E. Meissner in 1918 [53]. He showed that when $g(\tau)$ is a square wave modulation function, Eq (1) has an analytical solution because it can be viewed as a pair of constant coefficient equations each valid in alternating time intervals. Finally, the mathematical theory to study the stability of Eq (1) was introduced in the nineteenth century by Gaston Floquet [54]. He introduced the foundation to study the stability of any ODE with periodic coefficients which is today known as Floquet theory. In this thesis we will study both types of modulations.

Floquet theory

In 1883, Gaston Floquet introduced an elegant method to analyze the stability of time-periodic systems [54]. We present here the explanation for the particular 2-dimensional system which we will focus on throughout this manuscript. However, this theory can be generalized to N -dimensional systems [54, 55, 56, 57].

Let's define the state vector $\mathbf{y} = [y, \dot{y}]^\top$ and introduce it into Eq (1). The dynamical equation then reads

$$\dot{\mathbf{y}}(\tau) = \mathbf{J}(\tau)\mathbf{y}(\tau), \quad (2)$$

where $\mathbf{J}(\tau)$ is the Jacobian matrix defined as $\mathbf{J}(\tau) = \begin{bmatrix} 0 & 1 \\ -(\alpha^2 + \beta^2 g(\tau)) & 0 \end{bmatrix}$.

Floquet's theory [54] says that for a time-periodic equation of the shape $\dot{\mathbf{y}}(\tau) = \mathbf{J}(\tau)\mathbf{y}(\tau)$ with a \mathcal{T} -periodic Jacobian matrix the solutions can be sought in the form

$$\mathbf{y}(\tau) = \sum_{n=1}^2 c_n \mathbf{y}_n(\tau) \quad (3)$$

where $\mathbf{y}_n(\tau)$ are called the fundamental solutions and c_n are two constants determined by the initial conditions. We remind the reader that in Eq (3) the summation goes until 2 because it is the dimension of our state vector \mathbf{y} . Furthermore using the \mathcal{T} -periodicity of the Jacobian matrix we have

$$\dot{\mathbf{y}}_n(\tau + \mathcal{T}) = \mathbf{J}(\tau + \mathcal{T})\mathbf{y}_n(\tau + \mathcal{T}) = \mathbf{J}(\tau)\mathbf{y}_n(\tau + \mathcal{T}), \quad (4)$$

so that the $\mathbf{y}_n(\tau + \mathcal{T})$ also verifies equation (2). This shows that the solutions $\mathbf{y}_n(\tau + \mathcal{T})$ can be expressed as a linear combination of the two independent fundamental solutions $\mathbf{y}_n(\tau)$. Therefore it exists a 2×2 constant matrix Φ , called the Monodromy matrix, that maps a

particular set of fundamental solution $\mathbf{Y}(\tau) = [\mathbf{y}_1(\tau), \mathbf{y}_2(\tau)]^\top$ at time τ into their respective values at time $\tau + \mathcal{T}$:

$$\mathbf{Y}(\tau + \mathcal{T}) = \mathbf{Y}(\tau)\Phi. \quad (5)$$

The matrix Φ called the Monodromy matrix maps the solution from τ to time $\tau + \mathcal{T}$. It is used to study the stability of the trivial solution by computing its eigenvalues ρ_n and eigenvectors $\mathbf{y}_n(\tau)$. For an eigenvector of Φ we have:

$$\mathbf{y}_n(\tau + \mathcal{T}) = \mathbf{y}_n(\tau)\rho_n. \quad (6)$$

The ρ_n are therefore called Floquet multipliers [46, 54] which are independent on the choice of the fundamental matrix Φ . This property will be very useful for the numerical study because by putting the initial condition as $\mathbf{Y}(0) = \mathbb{1}$ and using Eq (5) the Monodromy matrix simply reads $\Phi = \mathbf{Y}(\mathcal{T})$.

Finally Floquet's theory [54] tells us that we can express the fundamental solutions $\mathbf{y}_n(\tau)$ in the so-called Floquet normal form :

$$\mathbf{y}_n(\tau) = \mathbf{r}_n(\tau)e^{s_n(\tau)} \quad (7)$$

where $\mathbf{r}_n(\tau + \mathcal{T}) = \mathbf{r}_n(\tau)$ is a 2-dimensional complex vector of period \mathcal{T} and s_n is a complex number called the Floquet exponent. Then, from Eq (6) and from the \mathcal{T} -periodicity of \mathbf{r}_n we have

$$\mathbf{y}_n(\tau + \mathcal{T}) = \mathbf{r}_n(\tau + \mathcal{T})e^{s_n(\tau + \mathcal{T})} = \mathbf{y}_n(\tau)e^{s_n\mathcal{T}}. \quad (8)$$

By identifying Eq (6) with Eq (8), we have a direct relation between the Floquet exponents s_n and the Floquet multipliers ρ_n that reads

$$\rho_n = e^{s_n\mathcal{T}} \iff s_n = \frac{1}{\mathcal{T}} \ln \rho_n + i\omega m \quad (9)$$

where ω is the fundamental frequency defined as $\omega = 2\pi/\mathcal{T}$, i is the imaginary number and m is an integer from $0, \pm 1, \pm 2, \dots$. So, we can determine the stability of the equilibrium state by studying the value of the Floquet multiplier ρ_n or the values of the Floquet exponent s_n .

The stability of the equilibrium state for a system described by $\dot{\mathbf{y}}(\tau) = \mathbf{J}(\tau)\mathbf{y}(\tau)$ can be determined either by the absolute value of the Floquet multipliers ($|\rho_n|$) or the real part of the Floquet exponents ($\Re(s_n)$). The following statements are very similar to Lyapunov's theory [58] except that, in the present case of Floquet theory [54], the nature of the instability we encounter are different since Eq (1) has a periodic coefficient and are no more constant in time:

- If $\Re(s_n) < 0$ (or $|\rho_n| < 1$) : for all n , all fundamentals solutions $\mathbf{y}_n(\tau)$ converge towards zero as time increases, so does any perturbation $\mathbf{y}(\tau)$. The trivial equilibrium state is said to be asymptotically stable.
- If $\exists k$ such that $\Re(s_k) > 0$ (or $|\rho_k| > 1$), the corresponding fundamental solution increases exponentially, so does the perturbed $\mathbf{y}(\tau)$. The trivial equilibrium state is in this case unstable and three different scenarios must be considered:

- If $\Im(s_k) = m\omega$ for $m = 0, \pm 1, \pm 2, \dots$ (or $\Im(\rho_k) = 0$ and $\Re(\rho_k) > 0$) : the perturbed motion will be a \mathcal{T} -periodic oscillation that will exponentially grow in the direction of the k^{th} mode $r_k(\tau)$.
- If $\Im(s_k) = \omega/2 + m\omega$ for $m = 0, \pm 1, \pm 2, \dots$ (or $\Im(\rho_k) \neq 0$ and $\Re(\rho_k) < 0$): the perturbed motion will be a $2\mathcal{T}$ -periodic oscillation that will exponentially grow in the direction of the k^{th} mode $r_k(t)$.
- If $\Im(s_k) \neq \omega/2 + m\omega$ for $m = 0, \pm 1, \pm 2, \dots$ (or $\Im(\rho_k) \neq 0$) the perturbed motion is a periodic or quasi-periodic oscillation that exponentially grows in the direction of the the k^{th} mode $r_k(\tau)$.

Stability diagrams

The eigenvalues of the Monodromy matrix depend on the parameters (α^2, β^2) . To study them, we use a stability diagram [46, 59]. A stability diagram shows the evolution of the maximum value of the real part of the Floquet exponent $\Re(s_n)$ in the (α^2, β^2) space. As we have seen with Floquet theory, the system is stable only if $\Re(s_n) < 0$. The stability diagram for the Mathieu equation ($g(\tau) = \cos(\tau)$) is represented in Fig 5.a and the stability diagram for the Meissner equation ($g(\tau) = +1$ during $\mathcal{T}/2$ and -1 during the remaining $\mathcal{T}/2$) is represented in Fig 5.b.

Figure 5 shows that the stability of the equilibrium state depends on the modulation parameters (α^2, β^2) . For any diagram there is an alternation between unstable and stable tongues represented by coloured and white regions respectively. For the one degree of freedom system we are studying in Eq (1), these tongues never cross or overlap, even at high values of β^2 [46, 52]. Finally, we observe that the shape of the tongues depends on the type of modulation. Fig 5.b shows that for a square wave modulation, the instability tongues are tailored in discrete pockets meanwhile the instability tongues for the harmonic modulation are continuous tongues (Fig 5.a).

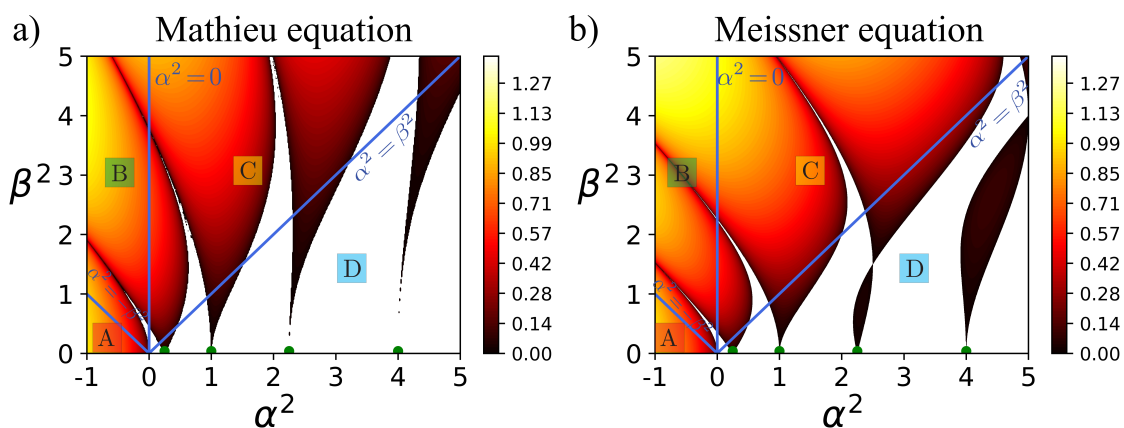


Figure 5: Stability diagram of a time-varying dynamical system without dissipation in the modulation parameter space (α^2, β^2) . The colour bar represents the evolution of $\max(\Re(s_n))$. Coloured regions are the instabilities tongues and white regions are the stability tongues. Green dots: tip of the instability regions defined by $\alpha^2 = (0.5k)^2$ with $k \in \mathbb{N}^*$.

Let's discuss the variations of α^2 and β^2 in these stability diagrams. Depending on α^2 and β^2 we have different physical scenarios (cases A-D in Fig 5). To interpret them, let's consider a mass in a potential energy which is defined as $\mathcal{E}_p = \frac{1}{2}(\alpha^2 + \beta^2 g(\tau))y^2$ (black line in Fig 6).

The particular case $\beta^2 = 0$ corresponds to the classic harmonic oscillator where the system is either marginally stable when $\alpha^2 > 0$ (harmonically oscillating with natural period $2\pi/\alpha$) or locally unstable when $\alpha^2 < 0$. The generalized case $\beta^2 > 0$ models parametric oscillators. For $\alpha^2 < 0$, it is eventually possible to dynamically stabilize a naturally unstable equilibrium but only if $\beta^2 > |\alpha^2|$, i.e. if the curvature of the potential \mathcal{E}_p is at least shortly positive (see cases A and B in Fig 6). The other case is when $\alpha^2 > 0$. The region where $\alpha^2 > \beta^2$ (case D in Fig 6) corresponds to classic parametric resonance where a response is enhanced. Finally, when $\alpha^2 > 0$ and $\beta^2 > \alpha^2$ corresponds to periodic modulations that are so large, that the curvature of the potential is shortly negative (case C in Fig 6). So, the two main physical functionalities of parametric instabilities are either parametric resonance, focusing on the instability tongues in cases D and C in Fig 5, or dynamical stabilization focusing on the stability tongues in case B in Fig 5.

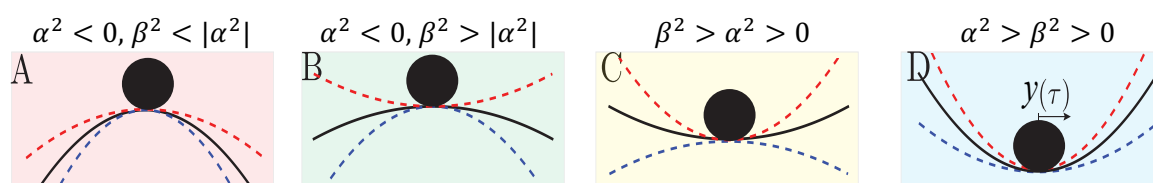


Figure 6: Four qualitative physical scenarios for a mass in a varying potential $\mathcal{E}_p = \frac{1}{2}(\alpha^2 + \beta^2 g(\tau))y^2$. Black lines show $\mathcal{E}_p = \frac{1}{2}\alpha^2 y^2$, red dashed lines $\mathcal{E}_p = \frac{1}{2}(\alpha^2 + \beta^2)y^2$ and blue dashed lines $\mathcal{E}_p = \frac{1}{2}(\alpha^2 - \beta^2)y^2$.

Damping in parametric instabilities

By ways of an asymptotic study [60, 61, 62], the beginning of the instability regions can be deduced. For $\beta \rightarrow 0$, the tips of the instability regions are defined as $\alpha^2 = (0.5k)^2$ with k a positive integer (green dots in Fig 5). The k^{th} instability region indicates the emergence of $2\mathcal{T}$ or \mathcal{T} -periodic motions if k is odd or even, respectively [46]. Having a simple access to the tip the unstable regions, parametric resonance can be used in various physical domains: from a child on a swing [49] to Micro Electro Mechanical Systems (MEMS) [39, 63] or plasma [64].

In a real system there are dissipations that tend to stabilize a system. Dissipation can be introduced in the system with the term $2\zeta dy/d\tau$ added to the left-hand side of Eq (1) where ζ is the damping factor. Figure 7.a represents the stability diagram for the damped Mathieu equation and Fig 7.b the stability diagram for the damped Meissner equation, both for $\zeta = 0.1$. Figure 7 shows that, compared to the undamped case in Fig 5, the instability regions start to vanish at low values of β^2 and by consequence the stability regions grow larger in the (α^2, β^2) space. This means the possible use of high order instability regions seems very difficult in domains with dissipation, at least for low values of β^2 or globally in case D.

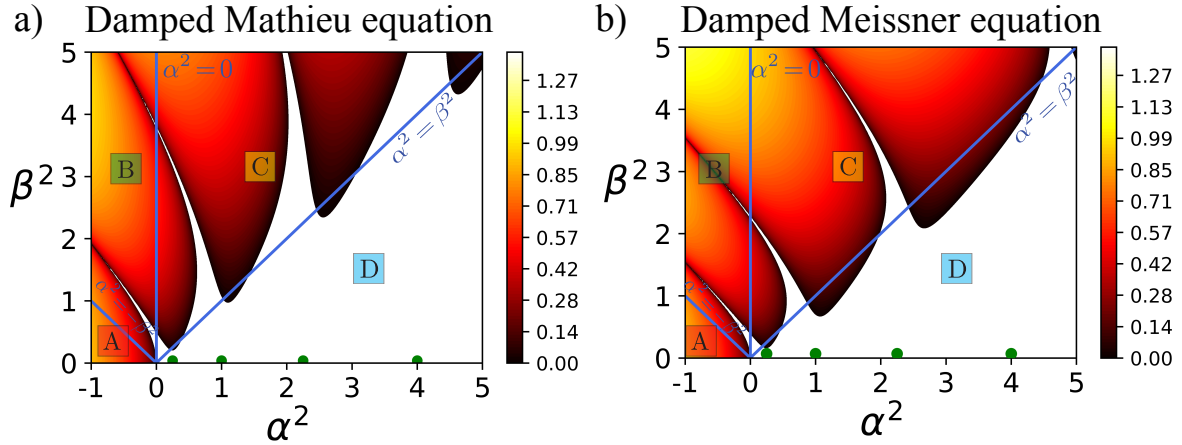


Figure 7: Using parametric instabilities for parametric resonance. Green dots are the tip of the unstable regions defined by $\alpha^2 = (0.5k)^2$ with $k \in \mathbb{N}^*$. a) Undamped stability chart for the Mathieu equation. b) Damped Mathieu equation for damping ratio $\zeta = 0.1$. Damping in the domain limits instabilities pushing the tip of the unstable tongues to higher values of β^2 .

The presence of dissipation in macroscopic systems is one of the most important limitations to exploit parametric instabilities. Dissipation drastically changes the stability diagram at small β^2 reducing the instability tongues. However, at large modulations β^2 , there are still a predominance of instability tongues (case “C” in Fig 7). To overcome the drawbacks of dissipation and expand the use of parametric instabilities at the macroscopic scale we propose to explore the region of large β^2 : high order parametric resonance.

Dynamical stabilization

Instead of enhancing a response using the instability regions, we can use the stability regions to stabilize a naturally unstable equilibrium. We focus here on the stable tongues for $\alpha^2 < 0$ (white regions in Fig 8). The most famous and first theoretical approach to stabilize a system using parametric instabilities was by Kapitza [65] in the Mathieu case ($g(\tau) = \cos(\tau)$). In 1951, he showed that the upward position of a pendulum can be stabilized if the suspension point is oscillated vertically at a sufficiently fast frequency. By using a fast frequency of modulation he studied Eq (1) dividing it in two times scales (one slow and one fast) and deduced a theoretical approximation of the bottom of the first stability region [65] which is famously known as the Kapitza limit. In the (α^2, β^2) space the Kapitza limit is $\beta^2 = \sqrt{2\alpha^2}$ and is represented by a green curve in Fig 8 for $\alpha^2 < 0$. This theoretical limit is exploited in a plethora of systems from the stabilization of microscopic inverted pendulums [66] to the development of ion traps [67].

Nevertheless, this theoretical approximation is only valid for fast frequencies of modulations compared to the natural time scale of the system and for small modulations ($\beta^2 \rightarrow 0$) as we can see in both stability diagrams in Fig 8. Beyond $\beta^2 \approx 0.75$ the theoretical limit does not longer describe the bottom of the first stability region for the harmonic modulation (Fig 8.a) and it is no longer valid for $\beta^2 \approx 0.2$ for the square wave modulation (Fig 8.b).

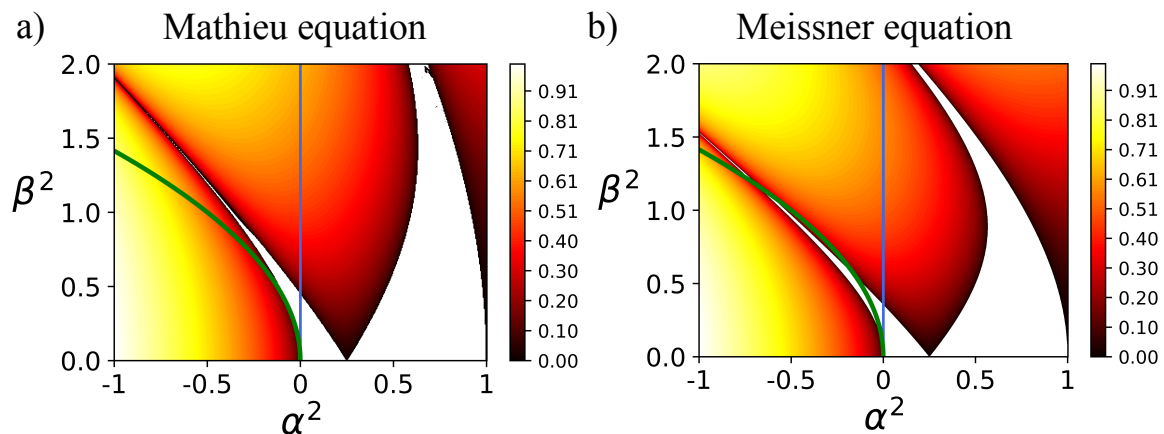


Figure 8: Using parametric instabilities for dynamical stabilization: focus on the white regions. Green curve is the theoretical Kapitza limit which follows the lower edge of the first stability region. It is limited to fast frequency of modulation and small amplitude of modulation β^2 .

For dynamical stabilization, dissipation does not have a strong influence as a limitation. Indeed, case B in Fig 7 is almost not affected by dissipation. For dynamic stabilization, the limitation is that at large values of β^2 the stability regions are thinner and thinner, so it is more difficult to deduce the set of parameters (Fig 8). Moreover, the only theoretical approach currently existing is limited to a specific region: small β^2 and fast frequencies of modulation with respect to the natural time scale of the system (Fig 8). We think this approach might be preventing us from exploring stabilization for higher modulations or even explore other stability regions.

Instead of using fast modulation frequencies to dynamically stabilize a system, we propose to use frequencies of modulations close to the natural time scale of the system and investigate if it is possible to stabilize a system for higher values of β^2 or if we can observe other stability regions with this approach.

Outline of the manuscript

Throughout this thesis we wish to provide new physical insights to overcome the existing limitations in parametric instabilities to extend the domain of use in the macroscopic scale. Our investigations are based on the development of experimental and theoretical proofs of concept. For parametric resonance we will explore the feasibility of triggering and exploiting large values of modulations in macroscopic systems. For dynamic stabilization, we propose to investigate the use of frequencies closer (or synchronized) to the natural time scale of the system to explore dynamical stabilization outside of the Kapitza approach.

In chapter 1 we focus on exploring the idea of using high modulations (large values of β^2) to exploit parametric resonance in macroscopic systems. By physical understanding different systems governed by parametric instabilities we want to infer what are the current limitations preventing us to achieve large β^2 , i.e explore high order of parametric resonance. We observe that the systems are currently limited at the tip of the unstable regions. We develop and

validate a new experimental setup at the macroscopic scale to go beyond the tip of the instability tongues. Then, a geometrical design rule is developed and experimentally validated to observe, control and trigger high order parametric instabilities. Finally, by changing the shape of the modulation function, we show that it is possible to use parametric instabilities to trigger and sustain the natural oscillation of a dynamical system.

In chapter 2 we revisit the current approach to dynamic stabilization. We analyze different experiments where we observe how dynamic stabilization is possible using Kapitza's approach. An experimental and numerical proof of concept is developed and we show that it is possible to stabilize a system with a modulation frequency closer to the natural time scale of the naturally diverging system and even go beyond the first stability region. However, the complete access to this region is difficult due to the small size of the stability regions. To access it in a simpler way, we use an analogy between initial and boundary value problem. By doing so, we introduce a pseudo-analytical resolution giving us a discrete number of master curves to deduce the parameters to stabilize an unstable system. Finally, these master curves are validated with our experimental setup.

1| Beyond the tips of the parametric instabilities tongues

Contents

1	Rationalizing parametric instabilities in a variety of experimental systems	16
1.1	The parametric pendulum: the classical example of a parametric system	17
1.2	Faraday waves, the pioneer of parametric instabilities	19
1.3	Microscopic example: Micro Electro Mechanical Systems	21
1.4	Discussion	22
2	Going beyond the tip of the parametric instability regions	24
2.1	Experimental setup	25
2.2	Characterization of the system	26
2.3	Experimental observation of extreme parametric instabilities	29
3	Controlling high order parametric instabilities	33
3.1	Rationalizing the instability regions for a square wave modulation	33
3.2	Triggering and sustaining a natural oscillation	39

One important functionality of parametric instabilities is parametric resonance. They appear when a parameter of the dynamical system is periodically varied in synchrony with one of its natural time scales, typically a multiple from the natural frequency of the system [46]. A typical example is observed when a person is on a swing and periodically stands and squats to increase the amplitude of the oscillations [49]. In this case the "up-and-down" movement vary the moment of inertia of the swing and amplifies the oscillations.

At the macroscopic scale the use of high order parametric instabilities is limited. To the best of our knowledge, the most common explanation is the presence of dissipation in the system. Dissipation tends to stabilize a system and reduce the presence of the unstable regions, as seen in Fig 7 of the Introduction. Nevertheless, dissipation may not be the only limitation on the use of high order parametric resonance. It is possible that the usual experimental setups for parametric resonance are also not facilitating the use of high order parametric resonances. To observe if the limitations to explore high order parametric resonance are not only caused by dissipation, we analyze the implementation of parametric instabilities in a variety of mechanical systems: solid and fluid mechanics at the macroscopic scale as well as one example at the microscopic scale. After the analysis, we will highlight that there are other physical and/or geometrical limitations preventing systems to trigger high order parametric resonance.

These limitations are rationalized and a new experimental concept is proposed to overcome these limitations and explore higher parametric resonances. This general concept is then implemented in a macroscopic experimental setup. We explain in detail our experimental proof of concept and show that we can observe high order parametric resonance at the macroscopic scale in the presence of dissipation. Moreover, studying the different experimental responses we deduce a geometrical relation to control and trigger a precise parametric resonance for the square wave modulation.

Finally, by changing the shape of the square wave it is possible to control and explore new and exciting dynamical responses using parametric resonances. For instance, by approximating the square wave modulation to an "impulse" train it is possible to trigger and sustain a natural oscillation.

1 Rationalizing parametric instabilities in a variety of experimental systems

As presented in the Introduction, Fig 5 shows how the stability of a linear parametric oscillator needs a complex stability diagram to be studied (numerous instability and stability regions strongly dependent on the parameters). The most used linear equation to describe the evolution of a position y which is periodically modulated is:

$$\frac{d^2y(\tau)}{d\tau^2} + (\alpha^2 + \beta^2 g(\tau)) y(\tau) = 0, \quad (1.1)$$

where α^2 represents a constant portion of the coefficient of y , β^2 accounts for the magnitude of the time variation and $g(\tau) = g(\tau + \mathcal{T})$ represents the \mathcal{T} -periodic modulation parameter.

Experimentally, in the presence of dissipation, the easiest instability tongue to reach is the first one (Fig 7 of the Introduction). Thus, parametric resonance is limited to appear only

if the driving frequency is two times faster than the natural frequency of the system. We want to show that there are other physical and/or geometrical reasons preventing us from going over the tip of the instability regions, besides dissipation.

To fully understand the scope of parametric instabilities we examine a variety of examples: one example in a macroscopic system (the parametric pendulum [68]), one example in fluid mechanics (Faraday waves [47, 69, 70, 71]) and one last example in microelectronics, to enhance the response of a Micro Electro Mechanical Systems (MEMS) [72, 73].

1.1 The parametric pendulum: the classical example of a parametric system

The most typical parametric oscillator we might use to illustrate this phenomenon is a parametric pendulum. An example of a parametric pendulum is a child pumping a playground swing by periodically standing and squatting to increase the amplitude of the swing's oscillations. In this case the standing and squatting motion is modulating the center of mass so that at the correct frequency the oscillations will increase [49, 74]. Instead of modulating the center of mass, one can modulate the length of the pendulum. An example can be a pendulum which is attached over a pivot point and it is cyclically pumped by pulling at the supporting rope [68]. The methods are different, but the outcome is the same, in both cases parametric instabilities are used to enhance the motion of the pendulum.

A classic experimental setup of the modulation of the length is presented in Fig 1.1.a: a pendulum is attached to a pivot point and its length is modulated by pulling at the supporting rope. The natural frequency of the system is defined as $\sqrt{g/L}$, so by modulating the length of the pendulum L the natural frequency of the system is modified. If the modulation is performed with the correct frequency the amplitude of the oscillations will increase, providing the pumping energy overcomes dissipation.

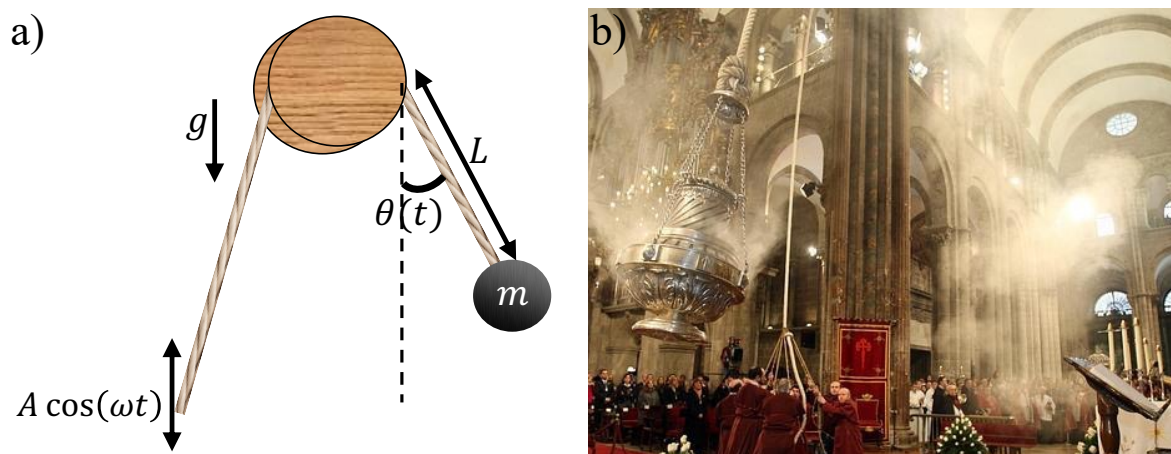


Figure 1.1: Parametric pendulum. a) Classical experimental setup of the modulation of the length of a pendulum. With L and m the length and the mass of the pendulum, ω the frequency of excitation, A the amplitude of excitation and g the gravitational acceleration. b) Apostles are modulating the rope to swing the Botafumeiro during the mass in the Cathedral of Santiago de Compostela. Image credit: © Catedral de Santiago de Compostela.

The dynamics of a parametric pendulum has been extensively studied [46, 49, 68, 74]. Based on these studies, the classical undamped nonlinear equation of motion describing the dynamics of this system reads

$$I \frac{d^2\theta(t)}{dt^2} + mL \left(g - A\omega^2 \cos \omega t \right) \sin \theta(t) = 0, \quad (1.2)$$

where $\theta(t)$ is the angular displacement measured from the vertical position, L is the length of the pendulum, m the mass and I the moment of inertia. The parametric modulation is characterized by the frequency of modulation ω and the amplitude of modulation A . We linearize Eq (1.2) near the equilibrium position $\theta = 0$ (approximation of small angles for the angular displacement $\theta(t)$). We approximate the moment of inertia as $I \approx mL^2$ and upon the change of variable $\tau = \omega t$, we are able to write Eq (1.2) in the standard dimensionless form of Eq (1.1) with a harmonic modulation, giving us the Mathieu equation [46, 48]

$$\begin{aligned} \frac{d^2\theta}{d\tau^2} + \left(\alpha^2 - \beta^2 \cos(\tau) \right) \theta(\tau) &= 0, \\ \text{with } \alpha^2 &= \frac{g}{L} \frac{1}{\omega^2}, \text{ and } \beta^2 = A \frac{1}{L}. \end{aligned} \quad (1.3)$$

An example of a parametric pendulum described by Eq (1.3) is the giant censer (O Botafumeiro) that hangs in the roof of the cathedral of Santiago de Compostela [68]. The censer has a mass m of 56.5 kg and a rope of length L equal to 20.6 m. To put it in motion by applying an external force is not a possible solution. Instead, several monks modulate the length of the pendulum (Fig 1.1.b). They have to pull and let go at the correct frequency to obtain the best energy transfer and trigger the motion.

To rationalize this type of systems we take the experimental values from [68]: the length of the pendulum is $L = 20.6$ m, the mass is $m = 56.5$ kg and the gravitational acceleration is $g = 9.81$ m.s⁻², and for a given modulation (frequency of modulation $\omega = 2\pi f$ and amplitude of modulation A) we rewrite them in the dimensionless modulation parameter (α^2, β^2) defined by Eq (1.3). The dimensionless parameters used by San Martin [68] are presented in Table 1.1 and the corresponding experimental point is reported in the stability diagram of Fig.1.4.

Table 1.1: Experimental parameters used by San Martin [68] and the corresponding values of the dimensionless modulation parameters α^2 and β^2 . This experimental data is presented in Fig.1.4.

Experimental parametric parameters	α^2	β^2
$f = 0.22$ Hz ; $A = 2.9$ m	0.244	0.141

Using the experimental values we deduce the proper frequency of the giant censer $\omega_0 = \sqrt{g/L} \approx 0.69$ rad.s⁻¹ which give us $f_0 \approx 0.11$ Hz. We observe that the frequency of excitation is twice the proper frequency of the pendulum (Table 1.1). This explains why San Martin data is in the first instability region in the stability diagram in Fig 1.4. With the expression of α^2 and β^2 in Eq (1.3) and the value of the experimental parameters we infer that the limitation we have in this system is related to the value of amplitude of modulation i.e

the value of β^2 : $A = 2.9$ m. If we keep the same length of pendulum and we want to reach $\beta^2 = 0.25$ (which is close to doubling the current value of β^2), using Eq (1.3) we deduce that the amplitude of excitation should be close to 5.9 m, a value that seems difficult to obtain manually. Furthermore, for this value of β^2 we are still in the first instability region, we are still unable to escape from it.

This first study shows that even if we do not consider dissipation, the modulation of the system performed by a geometrical parameter (in this case the modulation of the length of the pendulum) brings some physical limitations to the exploration of high order parametric instability regions.

1.2 Faraday waves, the pioneer of parametric instabilities

Although the parametric pendulum is one of the most common examples to explain parametric instabilities, it is not the first system where they were observed. The first experimental observation of a parametric modulation was made by M. Faraday in 1831 [47]. The experiment consists in spontaneously creating a surface wave by vertically vibrating a layer of a fluid on top of a membrane, thus modulating the effective local gravity felt by the perturbed surface waves [70, 71]. A classical experimental setup to observe Faraday waves is presented in Fig.1.2.

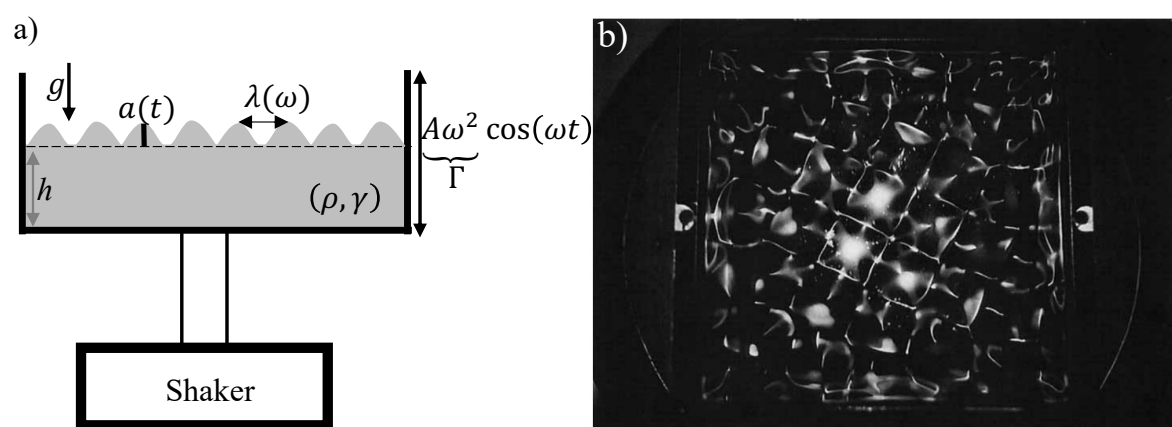


Figure 1.2: Faraday waves. a) Classical experimental setup: A fluid is placed on a cell over a shaker with a frequency of excitation ω and an acceleration of the excitation Γ . The fluid is characterized by: $a(t)$ the amplitude of displacement of the surface, h the depth of the fluid, γ the surface tension, ρ the density of the fluid, λ the wavelength and g is the gravitational acceleration. b) Observation of Faraday Waves for water containing Kalliroscope. Image credit: S. Douady [70].

Considering only the first mode of the waves and based on the work of Sir. Taylor [69], the evolution of the amplitude of displacement of the surface of the fluid in Fig 1.2.a reads

$$\frac{d^2 a(t)}{dt^2} + k \tanh(kh) \left(\frac{k^2 \gamma}{\rho} + g - \Gamma \cos(\omega t) \right) a(t) = 0 \quad (1.4)$$

and the dispersion relation for capillaro-gravitational waves is

$$\omega_0 = \sqrt{k \tanh(kh) \left(g + \frac{k^2 \gamma}{\rho} \right)}, \quad (1.5)$$

where ω_0 is the proper frequency of oscillation, k is the wavenumber, h is the depth of the fluid, γ is the surface tension and ρ is the density of the fluid. The modulation is defined by the frequency of excitation ω and the acceleration of excitation Γ . By implementing a change of variable $\tau = \omega t$ and using Eq (1.5) we write Eq (1.4) in the standard dimensionless form of Eq (1.1) with a harmonic modulation, giving us the classical Mathieu equation [48, 61]

$$\begin{aligned} \frac{d^2 a(\tau)}{d\tau^2} + (\alpha^2 - \beta^2 \cos(\tau)) a(\tau) &= 0 \\ \text{with } \alpha^2 &= \frac{k \tanh(kh)}{\omega^2} \left(g + \frac{k^2 \gamma}{\rho} \right), \text{ and } \beta^2 = \frac{k \tanh(kh) \Gamma}{\omega^2}. \end{aligned} \quad (1.6)$$

An experimental study of Faraday waves is presented for example in the work of Protière [71]. The fluid used is silicone oil with the following physical properties: surface tension $\gamma = 0.0209 \text{ N.m}^{-1}$, density $\rho = 0.965 \times 10^3 \text{ kg.m}^{-3}$, the depth of the fluid is $h = 4 \times 10^{-3} \text{ m}$ and the gravitational acceleration is $g = 9.81 \text{ m.s}^{-2}$. Using the dispersion equation of capillaro-gravitational waves Eq (1.5), the relation between the wavelength and the wavenumber ($k = 2\pi/\lambda$) and the experimental parameters (f, Γ) used by Protière [71] we calculate the dimensionless parameters (α^2, β^2) using Eq (1.6). The experimental parameters used by Protière [71] and their corresponding values in our (α^2, β^2) space are presented in Table 1.2. Finally they are reported in the stability diagram in Fig 1.4 with green dots.

Table 1.2: Experimental parameters for the Faraday waves used by Protière [71] with the corresponding dimensionless modulation parameters α^2 and β^2 . Data points are presented in Fig.1.4.

Experimental parametric parameters	α^2	β^2
$f = 20 \text{ Hz} ; \Gamma = 1g \text{ m.s}^{-2}$	0.249	0.196
$f = 80 \text{ Hz} ; \Gamma = 4g \text{ m.s}^{-2}$	0.250	0.201
$f = 120 \text{ Hz} ; \Gamma = 7.5g \text{ m.s}^{-2}$	0.251	0.232
$f = 160 \text{ Hz} ; \Gamma = 12.5g \text{ m.s}^{-2}$	0.250	0.267

In this example the relation between the experimental parameters and the dimensionless (α^2, β^2) parameters is more complicated. Because of the nature of the experiment we have a more intertwined expression of (α^2, β^2). With Protière's study [71] we find that all the experimental points in Fig 1.4 are in the first unstable region. But surprisingly with this setup one is capable of reaching $\beta^2 > \alpha^2$, as it can be seen in the last line of Table 1.2 and in Fig 1.4. This is remarkable because it means that the effective gravity is negative for a short time, i.e. the fluid tends to vertically escape the recipient against gravity. For this particular point we entered the "C" domain in Fig 1.4. Looking at the values of the parameters, we

can safely assume we are at the limit of the acceleration of excitation before the fluid is spilled over the experiment, the acceleration is already at $12.5g$. So we observe that going to larger values of (α^2, β^2) can be difficult with this experimental setup due to the complicated dependence of the parameters.

1.3 Microscopic example: Micro Electro Mechanical Systems

For now, we have focused on experimental examples at the macroscopic scale, but parametric instabilities have been exploited at the microscopic scale as well. Notably, they are used to amplify the movement of micro electro mechanical systems (MEMS) [72, 73].

In [73], the authors place a microscopic membrane (radius of 3.5mm) inside a vacuum to reduce friction and dissipation in the environment (the viscous damping ratio is $\zeta = 0.1$). The final fabricated MEMS chip is 12 mm by 12 mm and it is placed on top of a vibrational platform where the movement of the system is enhanced by vertically vibrating the membrane. A sketch of a MEMS and a photograph are presented in Fig 1.3. The interest in parametric modulations at the microscopic size is well-founded since at this scale, the vacuum packing makes it possible to remove dissipation. By eliminating dissipation in the environment, the tip of high order parametric regions is reachable at lower values of β^2 (Fig 5 in the Introduction).

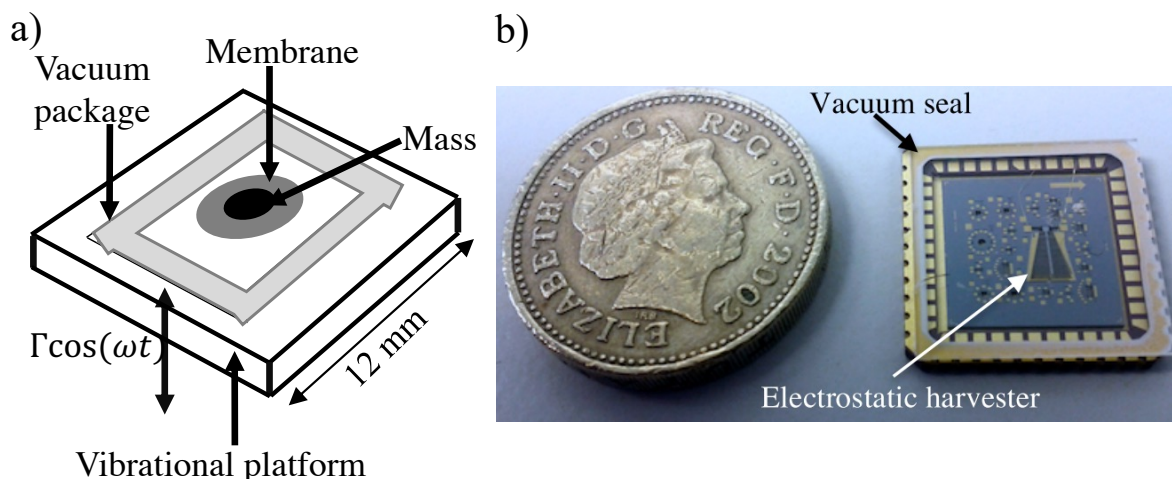


Figure 1.3: MEMS. a) Schematic representation of a MEMS. The system is a chip composed of a mass installed over a disk membrane which is then sealed by a vacuum package. The system is placed over a vibrating platform with a frequency of excitation ω and acceleration of excitation Γ . b) Photograph of a MEMS system besides a crown coin for scale. Image credit: Y. Jia et al. [63].

The equation to describe the motion of the MEMS is presented for example in the work of Jia et al. [73], where the motion of the membrane is described using a Duffing oscillator:

$$\frac{d^2x(t)}{dt^2} + 2\zeta_1\omega_m \frac{dx(t)}{dt} + \zeta_2 \left| \frac{dx(t)}{dt} \right| \frac{dx(t)}{dt} + bx^3(t) + (\omega_0^2 - \xi\Gamma \cos \omega t) x(t) = 0, \quad (1.7)$$

where $x(t)$ is the vertical displacement of the membrane, ω_0 is the natural frequency of the system, ζ_1 is the viscous damping ratio, ζ_2 is the nonlinear quadratic damping coefficient,

b is the mass normalized Duffing coefficient, ξ is a standard coefficient relating the external excitation to the parametric excitation, ω is the frequency of excitation and Γ is the acceleration of the excitation.

To adapt this equation to our framework we make the same assumptions presented in Jia et al. [73]. We consider no damping, and we neglect non-linear terms, i.e we consider only small displacements around the equilibrium position. Taking these considerations into account and upon the change of variable $\tau = \omega t$, Eq (1.7) can be written in the standard dimensionless form of the Mathieu equation:

$$\frac{d^2x(\tau)}{d\tau^2} + (\alpha^2 - \beta^2 \cos(\tau)) x(\tau) = 0 \quad (1.8)$$

with $\alpha^2 = \frac{\omega_m^2}{\omega^2}$ and $\beta^2 = \Gamma \frac{\xi}{\omega^2}$.

The experimental parameters we focus on are the one presented in Jia et al. [73]. The natural frequency of the membrane is $f_0 = 980$ Hz and the value of the standard coefficient is $\xi = 1.7744 \times 10^6$. The dimensionless experimental parameters are calculated using the experimental values of Jia et al. [73] and Eq (1.8). The corresponding experimental points are reported in Table 1.3 and shown in the stability diagram in Fig 1.4 with red crosses. The experimental data in Table 1.3 correspond to the first four unstable regions. This is confirmed with the experimental points in Fig 1.4. It also interesting to point out, the frequencies of modulations in Table 1.3 are respectively 2 times the proper frequency f_0 , then equal to f_0 , followed by $f = 2/3f_0$ and finally $f = 1/2f_0$, showing that the theoretical approximation of the tip of the instability regions is a very useful experimental tool.

Table 1.3: Experimental parameters used by Jia et al. [73] and values of the corresponding dimensionless modulation parameters α^2 and β^2 . Data points are presented in Fig 1.4.

Experimental parametric parameters	α^2	β^2
$f = 1960$ Hz ; $\Gamma = 0.4$ m.s ⁻²	0.25	0.0047
$f = 980$ Hz ; $\Gamma = 0.5$ m.s ⁻²	1.0	0.023
$f = 650$ Hz ; $\Gamma = 6$ m.s ⁻²	2.27	0.64
$f = 480$ Hz ; $\Gamma = 8$ m.s ⁻²	4.17	1.56

1.4 Discussion

As presented with those three examples, classic parametric instabilities can appear in various physical domains. The macroscopic examples are limited to the first instability tongue (green dots and blue triangle in Fig 1.4). This means that to trigger a response at the macroscopic scale the frequency of modulation is approximatively two times faster than the natural frequency of the system. In the case of the Faraday waves [71], because the relation between the dimensionless parameters (α^2, β^2) and the experimental parameters is complicated, reaching further stability regions can be challenging.

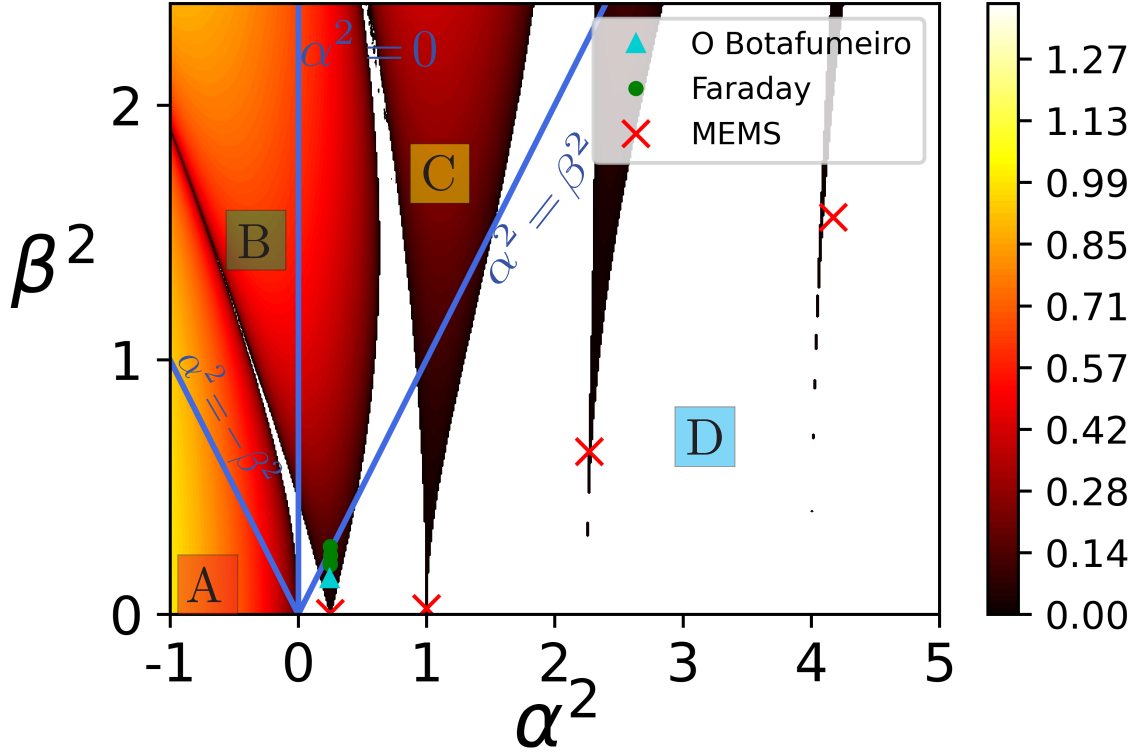


Figure 1.4: Linear stability diagram of the Mathieu equation in the dimensionless modulation (α^2, β^2) space with experimental data points. Blue triangle represent the experimental result for a parametric pendulum [68], green dots are the experimental results for Faraday waves [71] and red crosses are the experimental results for a MEMS resonator [73].

To explore further instability regions, one first practical idea is to put the frequency of modulation equal to the proper frequency of the system ($f = f_0$). By doing so we know we should reach the second instability region [46]. Then because we know the properties of the fluid, we can use the relation on Eq (1.6) to deduce the acceleration of the excitation. Taking the experimental values of Protière [71] for this example we deduced that the acceleration of the vibrating pot has to be higher than 12.5 times the gravitational acceleration. By imposing a higher acceleration, the fluid will start to spill out of the cell and be ejected all over the setup making it impossible to properly perform the experiment.

So, to access further instability regions, the other route is to increase the depth of the fluid bath, i.e we need a huge shaker, making the experiment unfit to explore high order of parametric instabilities. This shows that to be able to explore the full stability diagram we need a system where the dependence of parameters is easy to modulate.

In a similar way, this reasoning can be translated to the example with the O Botafumeiro. The experimental amplitude used by San Martin [68] in Table 1.1 is near the maximum physical limit for a human being. The monks are performing an amplitude of modulation close to three meters and they are six people pulling the rope (Fig 1.1.b). If we would like to reach the second instability region we should have the modulation frequency equal to the proper frequency of the system [46]. Let's suppose we do it for the experimental values of San

Martin [68] (same mass and length of the pendulum). This means that to be in the second unstable region $\alpha^2 \approx 1$ and using Eq (1.3) it can be deduced that the amplitude of excitation should be close to the length of the pendulum ($A \approx L = 20$ m). It has to be at least equal to the length of the pendulum because the dissipation in the domain “erases” the tip of the instability regions at small values of β^2 , so we should need to have $\beta^2 \approx 1$. This new value is close to seven times the current amplitude they are imposing, we should pass from $A = 3$ m to $A \approx 20$ m. So, the implementation is not feasible. The reasoning is also valid for a small pendulum, making amplitudes of modulation of the same length of the geometry of the system is difficult.

This shows that if we modulate the evolution function of the system with a geometrical parameter (change of length in this example) this could lead to important limitations. Can we modulate the evolution function of the system with an external component instead of changing its geometry?

At the microscopic scale it is possible to go beyond the first unstable region because they can work at low damping [63]. This has been observed in MEMS systems [72, 73] and their experimental results are presented by red crosses in Fig 1.4. We show only the first four instability regions but it is important to point out that working in a undamped environment allowed them to explore the 28th instability region [73] (an actual record established in 2016). Currently, MEMS experiments can be done in ultrahigh vacuum chamber where the quality factor $Q \approx 2 \times 10^6$ giving us a damping ration $\zeta = 1/2Q \approx 2.5 \times 10^{-7}$ [75]. For comparison at the macroscopic scale, in a classical experimental setup the quality factor is $Q \approx 1 \times 10^3$ giving $\zeta = 5 \times 10^{-4}$ [76]. By working at extremely low values of damping we can trigger high order parametric resonances. The vacuum packaging is feasible at the microscopic scale, but it is not a viable solution at the macroscopic scale. A second characteristic is that MEMS systems use an external component to trigger parametric instabilities. Indeed, they do not change the geometry of the membranes.

We have learned about the various physical limitations to trigger high order parametric instabilities at the macroscopic scale. To be able to explore them, we know the modulation should not be a geometrical modulation it should be an external field and the control of the external field must be independent form the primary setup. Finally, it is easier for this implementation if the relation between parameters is simple and direct.

2 Going beyond the tip of the parametric instability regions

In this section we are presenting an experiment inspired by the previous analysis. In particular, the goal is to experimentally observe high order of parametric instabilities at the macroscopic scale.

Firstly, we present the experimental setup, followed by the characterization of our system. Then, we present our experimental approach to explore high order (extreme) parametric resonances. Based on the experimental responses and physical arguments we develop a geometrical relation to control and trigger a precise instability region. We validate this geometric relation experimentally and we reach the 36th instability tongue.

Finally, by reshaping the square wave modulation into an impulse train we observe that it is possible to trigger a “natural” limit cycle sustained with a small amount of energy input. This use of parametric resonance could bring new and exciting implementations to dynamical systems.

2.1 Experimental setup

After analyzing the experimental limitations of previous setups for triggering parametric instabilities (Section 1), we know that to achieve high order of parametric resonance we need a system where its natural time scale can be drastically modulated with ease, without changing its geometry and the modulation should be from an external component. So, the setup is composed of one main mechanical system which natural time scale is modulated.

The main mechanical system we choose is a pendulum with a metallic marble (Fig 1.5). The pendulum is one, if not, the most well-known mechanical oscillator. The natural frequency of the system is defined as $\omega_0 = \sqrt{g/l}$ (and natural time scale $T_0 = 2\pi/\omega_0$) where g is the gravitational acceleration and l it is the length of the string. As previously said, we cannot change the length of the pendulum. As we have seen, a geometrical modulation brings limitations to the exploration of high order parametric regions (Table 1.1). So instead of changing the length of the pendulum to modulate ω_0 we are going to modulate the local gravitational field near the pendulum.

For this, we symmetrically place the metallic marble, of radius $r = 0.6$ cm, in the middle of two attracting electromagnets (with typical holding force of 1000 N) that are separated by a distance $d = 4$ cm (Fig 1.5). The pendulum is attached with two strings in V-shape, to ensure the oscillations remain in a plane, and has an effective length of $l = 4.3$ cm. The electromagnets are connected to a generator which fixes the value of the electrical current I . The electrical current is responsible of the intensity of the local electromagnetic field surrounding the pendulum. The stronger the value of I the stronger the electromagnetic field. Using a Controllino card we can turn ON and OFF the electromagnets by sending a T -periodical square wave function. Finally, to record the motion of the electromagnetic pendulum we use a Basler camera capable to record until 120 frames per second. To follow the marble, we place it in front of a white LED light to have a nicer contrast image (Fig 1.5). In order to obtain reproducible experiments, it is crucial to respect the following constraints:

- 1) The pendulum is placed symmetrically between the two electromagnets and the initial position has to be the same at each experience (closest possible).
- 2) The electromagnets have to be parallel and equidistant from the marble. This assure to have an homogenous electromagnetic field surrounding the marble.

To fulfill the first constraint, we put a stabilizer below the marble every time a new experimental observation or recording is made. The stabilizer is then pulled back down manually to keep the pendulum in its initial position. The second constraint is taken in account using the camera. Once connected to the computer we have access to a grid, and we can correctly place the electromagnets parallel and equidistant from the marble. Finally, to assure we have the same ω_0 and we are only modulating the gravitational field and not the geometry of the system, the string is fixed (taped) to the support and well tied on the pendulum.

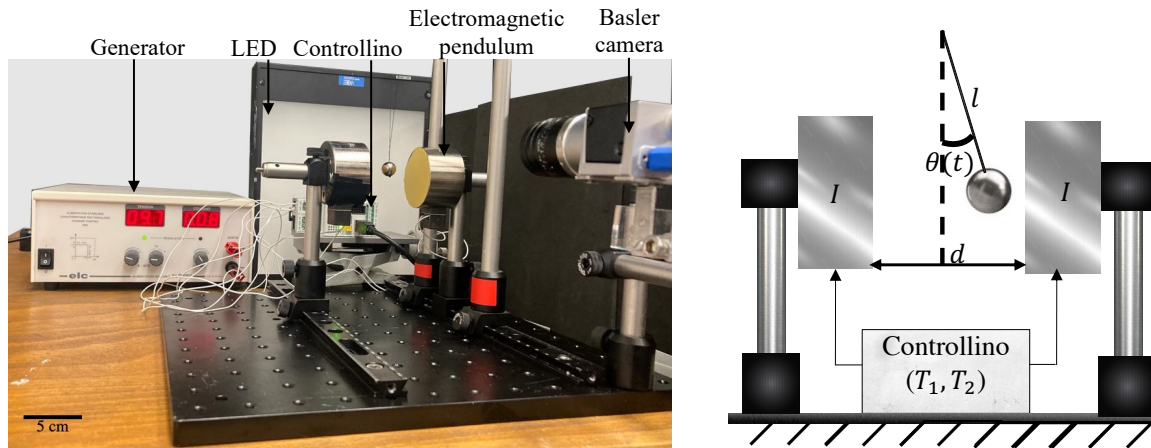


Figure 1.5: Experimental macroscopic setup to explore high order parametric instabilities. The system is a planar pendulum of length l with a metallic marble that is symmetrically placed between two identical attracting electromagnets whose attracting force depends on the imposed electrical current I . A Controllino card is used to send T -periodic square wave modulations.

2.2 Characterization of the system

Before exploring parametric instabilities, we need to understand how the modulation parameter affects the system. The electromagnets are both using an attracting force pulling the pendulum towards them, i.e there will be a competition between the electromagnetic force (pulling up the marble) and the gravitational force (pushing down the marble).

This competition between forces can be interpreted as a variation of the local gravitational field surrounding the pendulum. Once the electromagnets are turned ON, the pendulum is under a local effective gravitational field, g_{eff} . The natural frequency of a pendulum is defined by the gravitational acceleration, so in presence of an effective gravitational field the natural frequency should change. We investigate how the electromagnetic field, controlled by the electrical current I , affects the natural frequency. The evolution of the electromagnetic field around the pendulum is not our main interest for this study, it is a tool to implement a strong modulation of the time scale.

The experimental protocol is the following: the geometry of the pendulum is intact and does not change over the set of the experiments (the length of the pendulum is fixed). With the Controllino card we send a continuous signal, the electromagnets are turned ON (Figure 1.6). We fix a value of the electrical current I and locally perturb the pendulum from its vertical equilibrium position with a small initial angle $\theta(0)$ at time $t = 0$. Then we record the motion of the pendulum and obtain a response for every value of I .

To obtain an experimental response, first we turn ON the white LED and take a photograph of the background without the marble. Then, we follow the protocol described above. We record the motion of the marble using the Basler camera and having the white LED ON. We obtain a sequence of images well contrasted where the motion of the marble can be tracked. Before tracking the motion of the marble, we subtract the photograph of the background to every image to eliminate any potential reflection and only have the marble at each image.

Finally, we track the motion of the marble and obtain the response of the pendulum for a fixed value of the electrical current I .

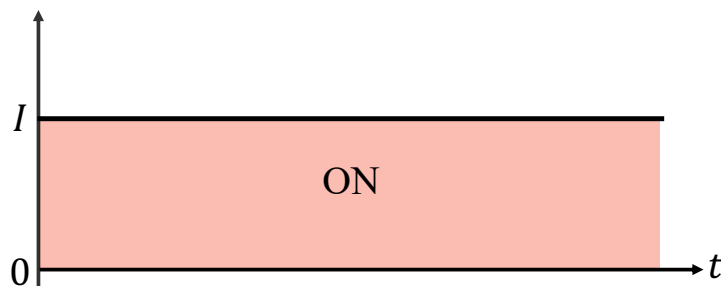


Figure 1.6: Continuous signal to characterize the effect of the electrical current I in the natural frequency of the system. The electromagnets are always ON.

We introduce the scalar $\omega(I)$ to characterize the experimental evolution of the frequency of oscillation for this given value of I . This scalar represents the natural time scale of the electromagnetic pendulum and gives us the effect of the modulation of the local gravitational field in our system. The value of $\omega(I)$ is obtained by doing a Fast Fourier Transformation (FFT) of the response.

To validate our protocol and our post processing, we will first observe the motion for $I = 0\text{A}$. Without electrical current there is no local electromagnetic field, so the local gravitational field is equal to the gravitational acceleration. The system should be a simple pendulum oscillating at its natural frequency $\omega_0 = \sqrt{g/l} \approx 15.1 \text{ rad.s}^{-1}$. To validate our post-process, we should track correctly the oscillatory motion and obtain an experimental frequency close to 15.1 rad.s^{-1} . The experimental response is presented in Fig 1.7.

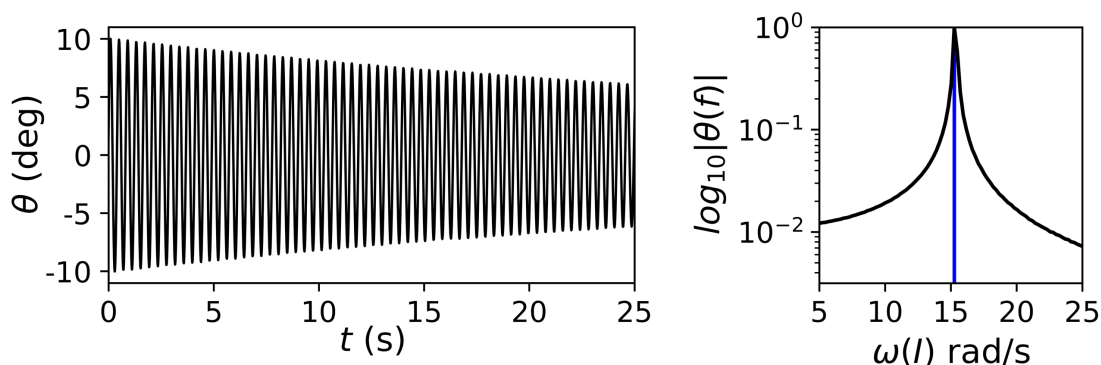


Figure 1.7: Experimental validation and post-processing for the natural response of the pendulum ($I = 0\text{A}$). We obtain an oscillatory harmonic response validated with a FFT having only one peak at 15 rad.s^{-1} .

The experimental response in Fig 1.7 shows an oscillatory motion of a pendulum and with the corresponding FFT the response has one peak, confirming the harmonic motion. Finally the peak is placed at $\omega(0) \approx 15 \text{ rad.s}^{-1}$, which is in perfect agreement with the value found with the geometrical parameters. Thus, our protocol to obtain the motion of the pendulum is validated. Figure 1.8 presents the experimental responses for three different values of the electrical current I .

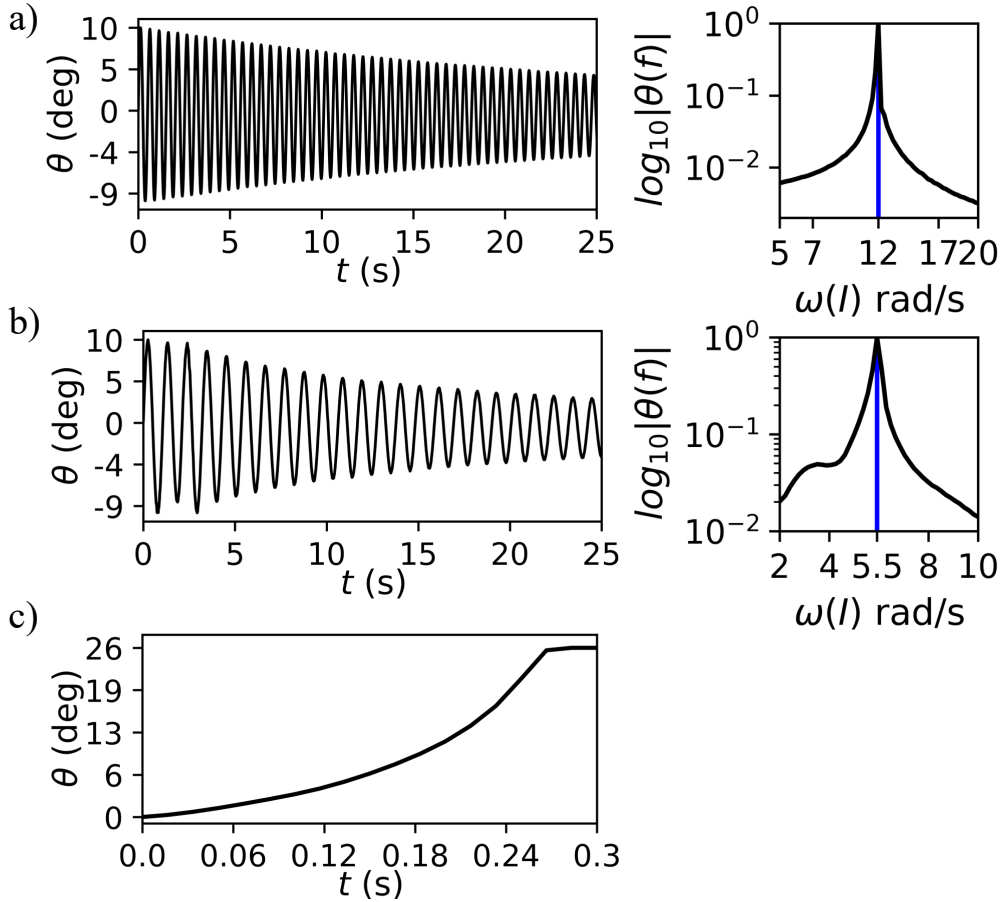


Figure 1.8: Experimental responses of the electromagnetic pendulum for different values of the control parameter I using a continuous signal. The FFT is performed for each oscillatory response to obtain the value of $\omega(I)$. a) $I = 0.4$ A. Slower oscillatory response with $\omega(0.4) \approx 12 \text{ rad.s}^{-1}$. b) $I = 0.65$ A. Even slower oscillatory response with $\omega(0.65) \approx 5.5 \text{ rad.s}^{-1}$. c) $I = 0.75$ A. No longer an oscillatory response but a divergent response, the value of $\omega(I)$ is deduce using an exponential fitting, we have $\omega(0.75) \approx i0.5 \text{ rad.s}^{-1}$.

In Fig 1.8 we have $I \neq 0$, i.e the system is under an effective gravitational field g_{eff} . Figure 1.8.a presents the experimental response for $I = 0.4$ A. It is an oscillatory response but this time it is slower than before. With the FFT we deduce that $\omega(0.4) \approx 12 \text{ rad.s}^{-1}$ which is smaller than $\omega(0)$. So, we do have a variation on the frequency of the system depending on the control parameter I . Physically, as said before, the impact of the electromagnetic force can be translated as the effective gravitational field. Let's define them by $\omega(I) = \sqrt{g_{eff}/l}$. Then, from the value of $\omega(0.4)$, and because the length of the pendulum is not changed, we can deduce that $g_{eff}(0.4) \approx 6.2 \text{ m.s}^{-2}$. As expected, when $I \neq 0$, the effective gravitational field decreases due to the competition of the electromagnetic force and the gravitational force. Then we have the experimental response for $I = 0.65$ A in Fig 1.8.b. We have an even slower experimental response characterized by $\omega(0.65) \approx 5.5 \text{ rad.s}^{-1}$ and this is translated by a corresponding $g_{eff}(0.65) \approx 1.3 \text{ m.s}^{-2}$. The electromagnets are pulling more strongly the system as I increases. Finally, Fig 1.8.c shows the experimental response for $I = 0.75$ A. This time the pendulum does not have an oscillatory response. For this value of I the electromagnetic force is stronger than the gravitational force making the pendulum attach to

one of the electromagnets. Thus, the system does no longer oscillates but instead it locally diverges. This shows that the control parameter I allows the system to change to different types of responses. To take in consideration both responses (oscillatory and divergent) the linear angular responses of the system can be written in the form $\theta(t) = \theta(0)e^{-i\omega(I)t}$. For a divergent response, we fit an exponential into our experimental response to deduce the value of $\omega(I)$. Therefore for the response in Fig 1.8.c we deduce that $\omega(0.75) \approx i0.5 \text{ rad.s}^{-1}$. With the control parameter I we can strongly modulate the natural time scale of the electromagnetic pendulum and the scalar $\omega^2(I)$ can characterize this evolution. To have a proper evolution of $\omega^2(I)$ we do the previous analysis for more values of I (Fig 1.9).

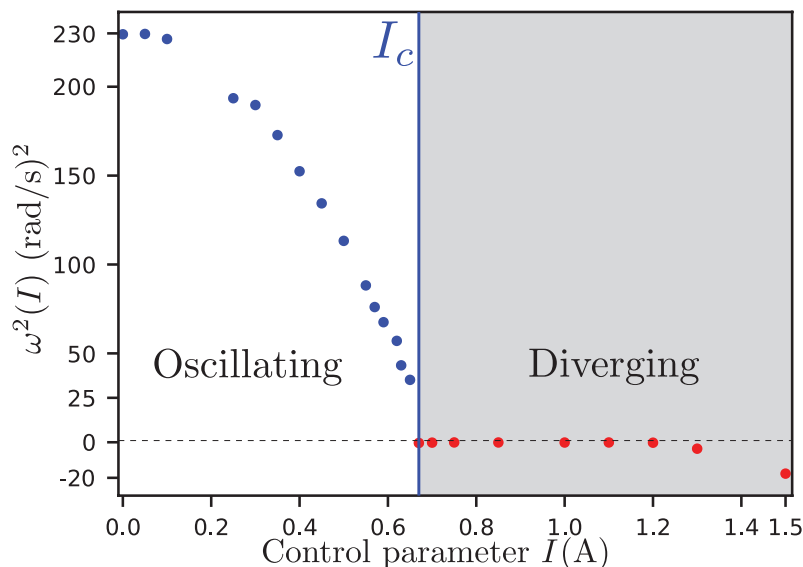


Figure 1.9: Characterization of the system as a function of the control parameter I . The scalar $\omega^2(I)$ characterizes the local evolution function of the electromagnetic pendulum which drastically depends on I . There is a specific value of the electrical current I_c where we pass from an oscillatory system ($I < I_c$) to a diverging system ($I > I_c$).

With the diagram in Fig 1.9 we observe indeed the existence of a critical value I_c of the electrical current for which the system is no longer oscillating ($I < I_c$) but is now a diverging system ($I > I_c$). As presented with the experimental responses in Fig 1.7 and Fig 1.8.a.b when $I \rightarrow I_c$ we have an oscillatory response with a decreasing $\omega^2(I)$. Above this critical electrical current I_c , the pendulum locally diverges eventually choosing one electromagnet depending on initial symmetry imperfections, as we can see in Fig 1.8.c. Finally, for $I \approx I_c$ the bifurcation is sub-critical, there is always a “jump” of $\omega^2(I)$ around I_c , making the recording of responses difficult.

2.3 Experimental observation of extreme parametric instabilities

In this second set of experiments, we want to observe and trigger high order parametric instabilities. To do so we modulate $\omega^2(I)$ in a square wave fashion using the Controllino (Fig 1.5). The electromagnets are turned OFF ($I = 0$) and ON ($I \neq 0$) during T_1 and T_2

seconds respectively, so that the modulation period is $T = 2\pi/\omega = T_1 + T_2$ (Fig 1.10). We need to have $I < I_c$ (Fig 1.8) to be in the case “D” of the stability diagram in Fig 1.4. This means our system is an oscillator with frequency $\omega^2(0)$ during T_1 (electromagnets are OFF so the system oscillates at the natural frequency $\omega^2(0)$) and $\omega^2(I)$ during T_2 (electromagnets are ON with a particular value of I and the system oscillates with a frequency $\omega^2(I)$ deduced from Fig 1.9).

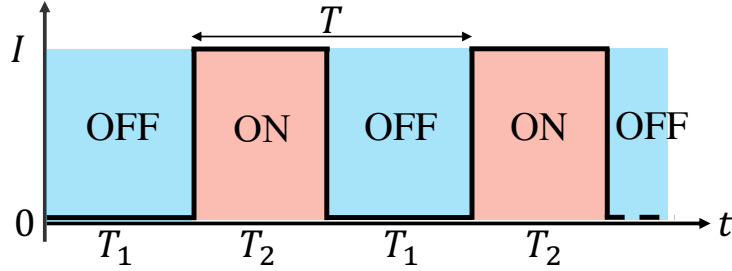


Figure 1.10: Experimental T -periodic square wave modulation to investigate parametric instabilities. The electromagnets are turn OFF and ON during T_1 and T_2 respectively.

To study the onset of instabilities we need linear equations about equilibrium $\theta = 0$. In our case of a two-state oscillator it reads

$$\begin{aligned} \frac{d^2\theta(t)}{dt^2} + \omega^2(0)\theta(t) &= 0 \quad \text{during } T_1, \\ \frac{d^2\theta(t)}{dt^2} + \omega^2(I)\theta(t) &= 0 \quad \text{during } T_2, \end{aligned} \quad (1.9)$$

where $\theta(t)$ is the angular displacement of the pendulum placed in the middle of the electromagnets (Fig 1.5). With this model we can study the experimental values of the couple (I, T) to trigger parametric instabilities. Equation (1.9) can be cast in the dimensionless form

$$\frac{d^2\theta(t)}{dt^2} + (\alpha^2 + \beta^2 g(\tau))\theta(t) = 0, \quad (1.10)$$

by introducing the dimensionless time $\tau = \omega t$, the square wave modulation function $g(\tau) = +1$ during $\mathcal{T}_1 = 2\pi T_1/T$ and $g(\tau) = -1$ during $\mathcal{T}_2 = 2\pi T_2/T$ and the dimensionless modulation parameters

$$\alpha^2 = \frac{\omega^2(0) + \omega^2(I)}{2\omega^2}, \quad \beta^2 = \frac{\omega^2(0) - \omega^2(I)}{2\omega^2}. \quad (1.11)$$

To observe parametric instabilities, we fix a value of the electrical current I and then vary the value of the period of modulation T and observe if we are able to trigger the response. It is important to emphasize that for this set of experiments $T_1 = T_2$, i.e the time spent in each oscillatory state is equally distributed during the period of modulation T . By fixing the period of modulation T we ensure the values of T_1 and T_2 . We fix $I = 0.6\text{A}$ and infer $\omega(I) \approx 6.8 \text{ rad}\cdot\text{s}^{-1}$ from Fig 1.9 and we have $\omega(0) = 15.15 \text{ rad}\cdot\text{s}^{-1}$ so the proper period of the system is $T_0 \approx 0.41\text{s}$.

The first experimental tests we perform are for T close to half of T_0 . If an instability is triggered, it should be the first (principal) instability region. For the majority of T values we tested, the response of the system is not enhanced, we have a harmonically damped oscillatory response (Fig 1.8). We increase the period of modulation to $T = 0.33\text{s}$ and then we observe an amplification of the response. This experimental response is presented in Fig 1.11.a. We observe that the response is amplified after 1.2 seconds and it reaches its maximum at $t = 2\text{s}$, where the marble has been attached to the pendulum. After the 2 seconds the response reaches a $2T$ -periodic limit cycle (the pendulum is alternately attached between the left and the right electromagnet). A $2T$ periodicity is a property of the first instability region [46] so this is a first good indicator that we trigger in fact the first instability region.

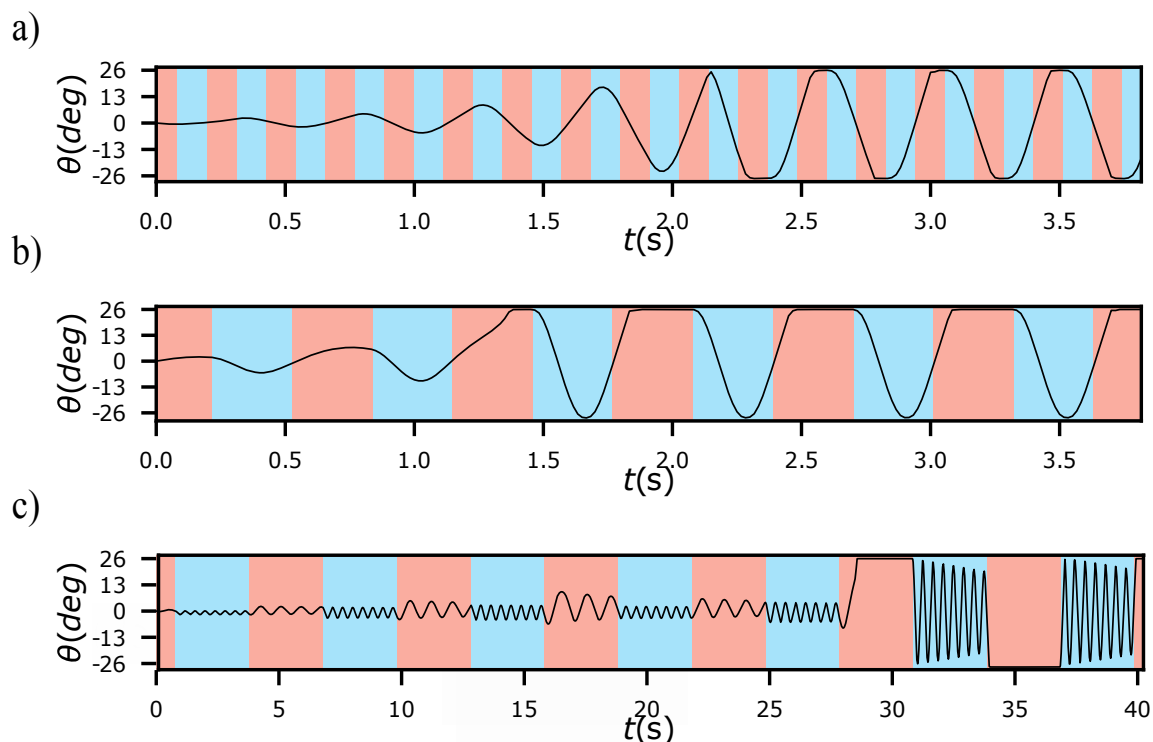


Figure 1.11: Experimental observation of high orders parametric resonances when $\omega^2(I)$ is modulated in a square wave fashion with $T_1 = T_2 = T/2$. Red background represents the electromagnets are turned ON and blue background represents when the electromagnets are turned OFF. a) Classical first parametric amplification obtained for $\omega(I) \approx 6.8 \text{ rad.s}^{-1}$ and $T \approx 0.33\text{s}$. b) Second parametric amplification obtained for $\omega(I) \approx 6.8 \text{ rad.s}^{-1}$ and $T \approx 0.62\text{s}$. c) Extreme parametric pumping obtained for $\omega(I) \approx 6.5 \text{ rad.s}^{-1}$ and $T \approx 6.02\text{s}$.

Trying to explore the second instability tongue is not a problem with this setup: we keep the same value of the electrical current I , i.e we have the same $\omega(I) \approx 6.8 \text{ rad.s}^{-1}$ but this time we need to have a period of modulation T close to the T_0 value. We try multiple values of T close to T_0 but, compared to the first region, it is much more complicated to find an amplified response. The values of the parameters (I, T) need to be very accurate. We finally obtain an amplification of the response for $I = 0.58\text{A}$ and $T \approx 0.62\text{s}$. This experimental response is presented in Fig 1.11.b. With these parameters, the parametric response triggers a T -periodic limit cycle which is a characteristic of the second instability region (there is an

alternation of $2T$ and T periodicity over the instability regions [46]).

Having been able to trigger the second unstable region at the macroscopic scale is already an achievement but our goal is to try to observe even higher order of parametric resonances. This time we are trying to observe a parametric response where the period of modulation is at least ten times the proper period of the system. Our quest starts at $I = 0.6$ A and the period of modulation $T = 5$ s $> 10 \times T_0$. We need to give the system more time to see if the amplification would manifest because the modulation period is longer. After lots of trials and errors for different values of (I, T) we were able to trigger a high order parametric response for $I = 0.62$ A and $T = 6.02$ s. This experimental extreme parametric pumping is presented in Fig 1.11.c. Compared to the two previous responses (Fig 1.11.a-b), we had to record the responses 10 times longer before the nonlinear regime is established. We observe that during T_1 (blue background) the system does 7.5 oscillations and during T_2 (red background) the systems does 3.5 oscillations. Once the pendulum becomes close enough to one of the electromagnets the metallic marble attaches to the electromagnet and the system enters in a $2T$ -periodic limit cycle.

Finally, the last proof to validate that we correctly trigger the first, the second and an extreme parametric resonance is to observe them in a stability diagram. We can determine the corresponding values of (α^2, β^2) for each experimental response using Eq (1.11) and then represent them in the stability diagram in Fig 1.12.

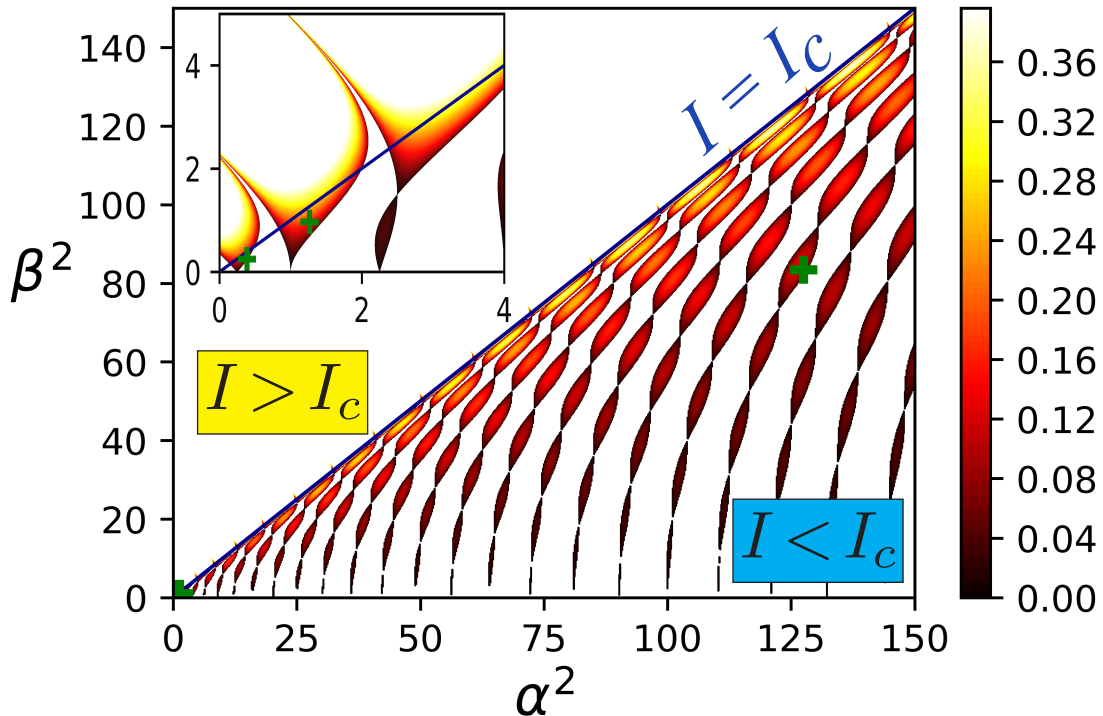


Figure 1.12: Stability diagram of the Meissner equation in the extended (α^2, β^2) space. Coloured regions represent the instability tongues. Green crosses represent the experimental parameters of Fig 1.11 expressed in the (α^2, β^2) space. Inset zooms on the classic first instability regions.

For the experimental response in Fig 1.11.a we have $\alpha^2 = 0.39$ and $\beta^2 = 0.24$. This experimental point is in the inset in Fig 1.12 and we validate that the given parameters are in fact in the primary instability region $k = 1$. So, we triggered the first parametric instability with our experiment setup. Secondly, for the experimental response in Fig 1.11.b we have $\alpha^2 = 1.24$ and $\beta^2 = 0.99$. This experimental point is also in the inset in Fig 1.12 and we observe that the experimental point is located precisely in the second instability region $k = 2$. Proving that with this experimental setup we are able to go beyond the first instability region. Finally, for the last experimental response in Fig 1.11, we have $\alpha^2 = 128.4$ and $\beta^2 = 82.5$. In this case, the values of (α^2, β^2) are higher. To observe this experimental point, we have to go beyond the classic first instability regions (inset in Fig 1.12). We have to observe it in the extended stability diagram in Fig 1.12. At large values of (α^2, β^2) we observe the stability diagram is different from the usual classic stability diagram in the inset. When we explore further instability regions (for the square wave modulation) the tongues are tailored into pockets. We observe the experimental point is in one instability pocket. For this experimental response we can not deduce to which region it corresponds because in the extremely extended domain we have a large number of instability pockets (Fig 1.12). So, for the moment we are not sure which k unstable region we have triggered. We know we have triggered an extreme parametric instability making a mode $(7.5, 3.5)$ (the number of oscillations in the respective T_1 and T_2 periods).

These experimental results validate our concept of extreme parametric oscillators. By implementing a symmetrical external component capable of strongly modulating the natural time scale of the system with ease (Fig 1.9) we are capable of eliminating the previous limitations found in macroscopic systems and trigger extreme parametric resonance, even in the presence of dissipation. Compared to the experimental points in the stability diagram in Fig 1.4 which were limited to the tip of the first instability region, we show in Fig 1.12 that we are no longer limited to the tip of the parametric regions (green cross in Fig 1.12). Nevertheless, navigate this new type of charts is not evident or simple. A strategy to navigate them is essential. For the particular modulation we are studying (the square wave), we believe that rationalizing the emergence of the pockets could be a great way to navigate the chart. It will be interesting to be able to go over the different instability regions with ease.

3 Controlling high order parametric instabilities

3.1 Rationalizing the instability regions for a square wave modulation

From the extensive theoretical work done in parametric instabilities we know that to be at the tip of the k^{th} instability region the frequency of modulation needs to be $0.5k$ the natural frequency of the system [46, 48, 54]. This is observed for the harmonic modulation with the experimental results of Jia et al. [73] presented in Table 1.3 where the authors used $0.5k$ multiples of the proper frequency of the membrane to trigger the first four parametric modes (red crosses in Fig 1.4 respectively placed in the first four instability regions for the harmonic modulation).

For the square wave modulation this relation is also valid. To trigger the first two parametric instabilities regions, we fixed the period of modulation as a multiple of the natural period of

the system (Fig 1.11). This property for the tip of the instability regions gives us an important insight: there is a proper timing well defined for each parametric region. So, to rationalize the instability pockets in the stability diagram of the square wave modulation and have a broader understanding on how to control extreme parametric instabilities we need to understand this timing (or synchronization) between the frequency of modulation and the proper time scale of the system. We believe the appearance of these pockets must be connected to the number of oscillations the system is doing during the corresponding periods of the square wave (Fig 1.11).

To understand this relation between the frequency of modulation and the natural time scale of the system we use our electromagnetic pendulum as an example. We have observed that to trigger parametric instabilities we modulate the natural frequency of the system by periodically turning ON and OFF the electromagnets. With Eq (1.10), we deduce that the dimensionless modulating frequencies of the system are $\sqrt{\alpha^2 + \beta^2}$ during \mathcal{T}_1 and $\sqrt{\alpha^2 - \beta^2}$ during \mathcal{T}_2 as presented in Fig 1.13.

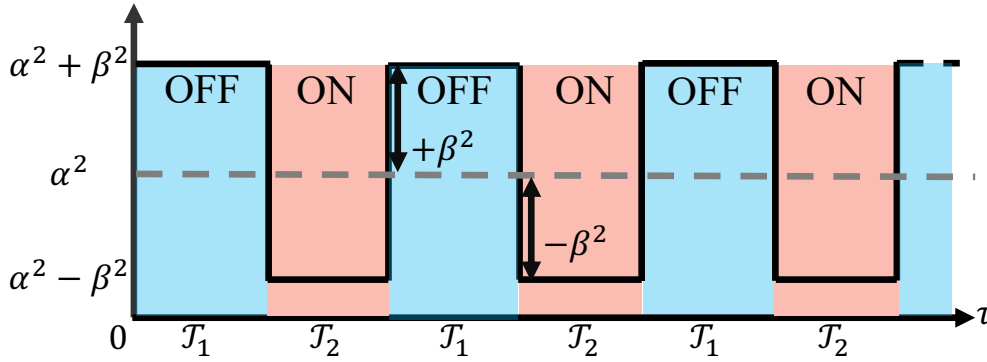


Figure 1.13: Dimensionless parameters of the electromagnetic pendulum modulated by a \mathcal{T} -periodic square modulation function between $+1$ and -1 where \mathcal{T}_1 and \mathcal{T}_2 represent when the electromagnets are turned OFF and ON respectively.

Physically, this modulation directly affects the potential energy of the system. Which can be defined as $\mathcal{E}_p = \frac{1}{2}(\alpha^2 + \beta^2 g(\tau))\theta^2$ with $g(\tau)$ the square wave modulation function. Let's analyze the potential energy evolution during one oscillation of the electromagnetic pendulum. At its equilibrium position, a small perturbation sets the system in motion. In terms of potential energy, this indicates that the system will climb a potential ("hill") of a particular slope. The system needs to ascend a potential with a mild slope in order to maximize its amplification. Thus, it is preferable for the mass to go up when the electromagnets are turned ON since the curvature has a flatter slope ($\alpha^2 - \beta^2$), as the red curvature in Fig 1.14 shows. Once the potential energy \mathcal{E}_p is at its maximum value, the mass has reach its maximum amplitude. The curvature must have the steepest slope to return to the center most efficiently. This is the case when the electromagnets are turned OFF and the curvature is defined by ($\alpha^2 + \beta^2$), as shown by the blue curve in Fig 1.14.

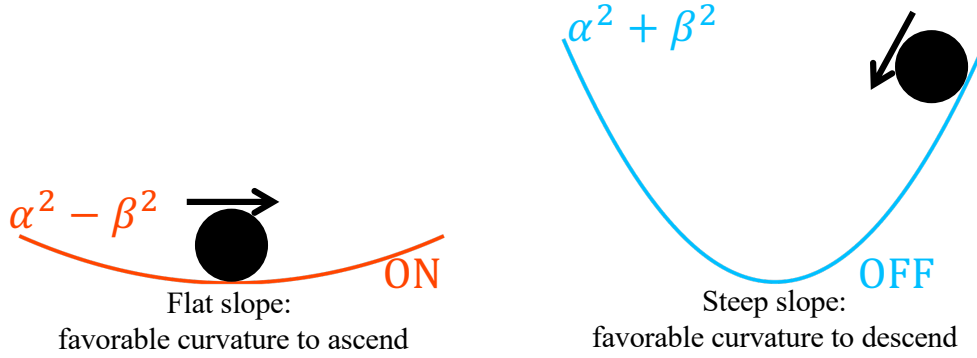


Figure 1.14: Schematic representation of the evolution of the curvature of the potential energy of the system $\mathcal{E}_p = \frac{1}{2}(\alpha^2 + \beta^2 g(\tau))\theta^2$ during the square wave modulation.

So, this analysis of the potential's curvature to amplify the motion shows that every time the pendulum passes the center position (minimum value of \mathcal{E}_p) the electromagnets should be turned ON (flatter slope: easier to ascend) and every time it reaches its maximum amplitude (maximum value of \mathcal{E}_p) the electromagnets should be turned OFF (steeper slope: improve the descend).

The first synchronization to enhance the amplification of the response during one oscillation is presented in Fig 1.15. Each time the pendulum passes the center the electromagnets should be turned ON physically meaning we are locally decreasing the value of the effective gravitational field surrounding the pendulum, helping the pendulum to ascend (red colour background in Fig 1.15). Each time the pendulum reaches its maximum amplitude, the electromagnets should be turned OFF physically meaning we are eliminating the help to go up and we are now helping it to descend by putting back the effective gravitational field at its maximum value: $g_{eff} = g$ (blue colour background in Fig 1.15).

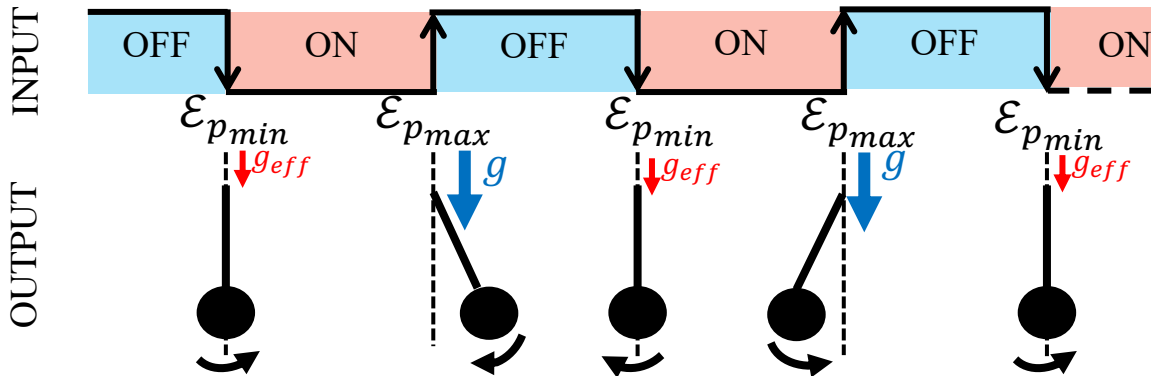
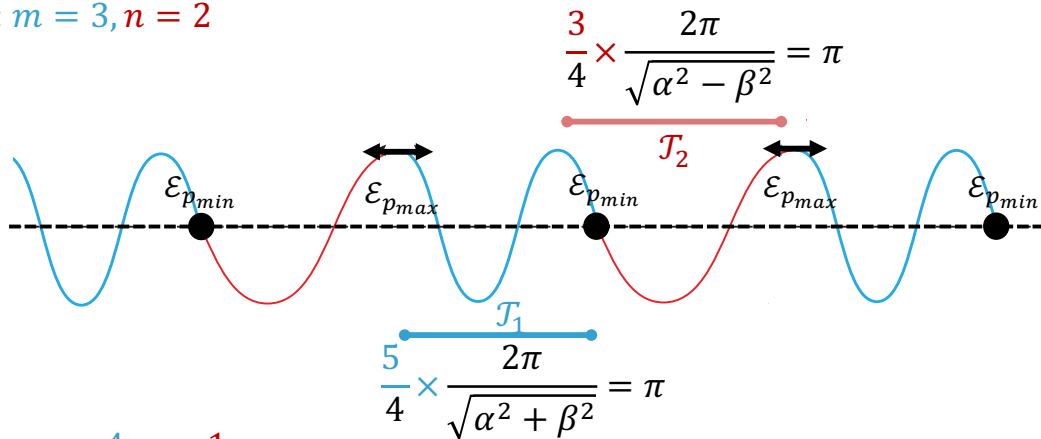


Figure 1.15: Schematic representation of the first input-output synchronization required for parametric pumping. One needs to decrease effective gravity (turn the electromagnets ON) when the potential energy is at its minimal (before the mass goes up) and put back a strong gravity (turn the electromagnets OFF) when the potential energy is at its maximum (before the mass goes down).

The first possible synchronization happens when we fit one quarter of oscillation at every period \mathcal{T}_1 and \mathcal{T}_2 respectively (Fig 1.15). This choice can be seen as a mode $(1, 1)$ and it represents the first possible parametric modulation to pump a dynamical response. This is the case of our experimental response in Fig 1.11.a where we trigger the primary instability region $k = 1$. However, it is also possible to attempt to fit more than one quarter of period during \mathcal{T}_1 and \mathcal{T}_2 respectively. This generalized synchronization can be a (m, n) mode, with m corresponding to the number of times the system passes the center during \mathcal{T}_1 and n the number of times the system passes its maximum amplitude during \mathcal{T}_2 before changing to the other state. Figure 1.16 shows two possible examples for this synchronization.

a) Mode: $m = 3, n = 2$



b) Mode: $m = 4, n = 1$

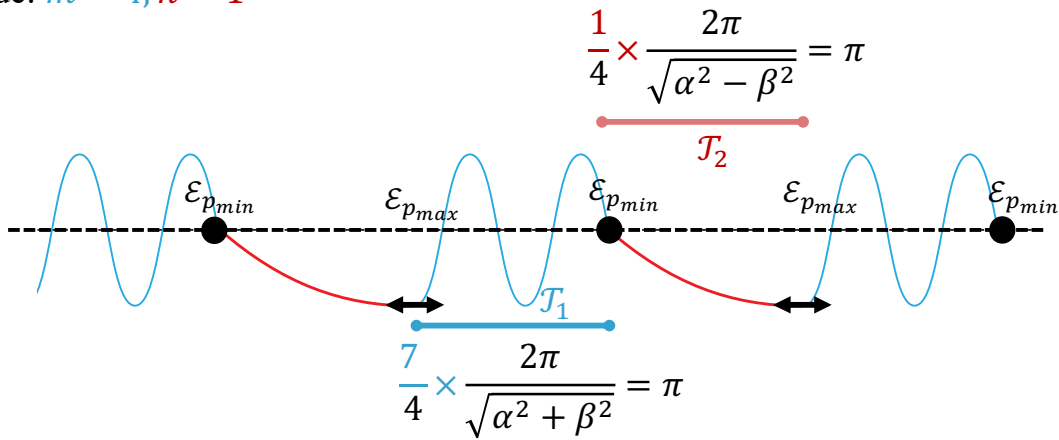


Figure 1.16: Representation of two possible synchronizations to amplify the response of a system using a 2π -periodic square modulation. a) Representation of the $(m = 3, n = 2)$ mode. The system does 5 quarter periods of oscillations during \mathcal{T}_1 and 3 quarter periods of oscillations during \mathcal{T}_2 . b) Representation of the $(m = 4, n = 1)$ mode. The system does 7 quarters and 1 quarter of periods of oscillations during \mathcal{T}_1 and 1 and \mathcal{T}_2 respectively.

The synchronization presented in Fig 1.16.a is a $(m = 3, n = 2)$ mode. So the system passes $m = 3$ times the center (minimum value of the potential energy) during \mathcal{T}_1 and does 5 quarter periods of oscillations before turning ON the electromagnets (blue line in Fig 1.16.a). Then while the electromagnets are ON during \mathcal{T}_2 (red line in Fig 1.16.a), the system reaches its maximum amplitude $n = 2$ times (maximum value of the potential energy) and does 3 quarter periods of oscillations before turning OFF the electromagnets. Figure 1.16.b shows

a (4, 1) mode. This means that during \mathcal{T}_1 (electromagnets OFF) the system crosses $m = 4$ times the value $\theta = 0$ before turning ON the electromagnets and it does 7 quarter of oscillations (blue line in Fig 1.16.b). The $n = 1$ means we are letting the system reach only one time its maximum amplitude during \mathcal{T}_2 before turning OFF the electromagnets, i.e it does 1 quarter of oscillations (red line in Fig 1.16.b).

We know that during \mathcal{T}_1 the period of the system is $2\pi/\sqrt{\alpha^2 + \beta^2}$ and during \mathcal{T}_2 the period of the system is $2\pi/\sqrt{\alpha^2 - \beta^2}$ (Fig 1.13). Then, with Fig 1.16 we infer that the number of quarter of oscillations the system does only depends on the values of the (m, n) mode. So combining both observations we deduce the following relation:

$$\left\{ \begin{array}{l} m = 3 \Rightarrow \frac{5}{4} \frac{2\pi}{\sqrt{\alpha^2 + \beta^2}} = \pi \\ n = 2 \Rightarrow \frac{3}{4} \frac{2\pi}{\sqrt{\alpha^2 + \beta^2}} = \pi \end{array} \right. \quad \text{and} \quad \left\{ \begin{array}{l} m = 4 \Rightarrow \frac{7}{4} \frac{2\pi}{\sqrt{\alpha^2 + \beta^2}} = \pi \\ n = 1 \Rightarrow \frac{1}{4} \frac{2\pi}{\sqrt{\alpha^2 + \beta^2}} = \pi \end{array} \right. \quad (1.12)$$

where we can deduce that the number of quarter periods we can fit during the modulation period \mathcal{T}_1 is equal to $(2m - 1)$ and equal to $(2n - 1)$ during \mathcal{T}_2 . So, this synchronisation can be rationalized and we can infer a new discrete design rule in the (α^2, β^2) as the mode numbers (m, n) are varied:

$$\frac{(2m - 1)2\pi}{4\sqrt{\alpha^2 + \beta^2}} = \pi \quad \text{and} \quad \frac{(2n - 1)2\pi}{4\sqrt{\alpha^2 - \beta^2}} = \pi. \quad (1.13)$$

In Fig 1.17a. we superpose the values of (α^2, β^2) calculated using this new geometric law Eq (1.13) with the extended stability diagram of the Meissner equation. This simple design rule gives the correct values of (α^2, β^2) (grey dots) to be in the (m, n) instability pockets. The value of (m, n) and the k^{th} instability region are numbered as follows $k = m + n - 1$. Finally this geometric rule is only valid for $m > n$ which is translated by $\alpha^2 > \beta^2$, as we can see in Fig 1.17.a

Exploring the stability diagram using the number of modes (m, n) is easier than having to compute the entire stability diagram. The value of m corresponds to the instability region counting from the origin and going over the $\alpha^2 = \beta^2$ curve. Once the value of m is fixed, the value of n corresponds to the number of pocket we are counting down from the $\alpha^2 = \beta^2$ curve. For example in the stability chart in Fig 1.17 a) we have the mode (15, 7) which corresponds to the 15th region counting from the origin and we go down to the 7th pocket. This means we are at the $k = 15 + 7 - 1 = 21^{\text{th}}$ instability tongue.

Using this new notation, we are able to rationalize our previous experimental results of Fig 1.11, which are again represented in the stability diagram in Fig 1.17 with green crosses. The first experimental response in Fig 1.11.a is a $(m, n) = (1, 1)$ unstable parametric mode correctly placed in the $k = 1$ unstable tongue (green cross in inset in Fig 1.17). The second experimental response in Fig 1.11.b is a $(m, n) = (2, 1)$ unstable parametric mode correctly placed in the $k = 2$ instability region (green cross in inset of Fig 1.17). The experimental response in Fig 1.11.c is the mode (15, 7) located in the $k = 21^{\text{th}}$ instability region and

represented by a green cross in Fig 1.17. It does 7.5 oscillations during T_1 (OFF in blue) meaning it passed 15 times the minimum value of the potential energy before turning ON the electromagnets and does 3.5 oscillations during T_2 (ON in red) meaning it passed 7 times the maximum value of the potential energy before turning OFF the electromagnets. The reported experimental data (green crosses) in the stability diagram of Fig 1.17 have an excellent agreement with the expected (m, n) parametric pumping mode.

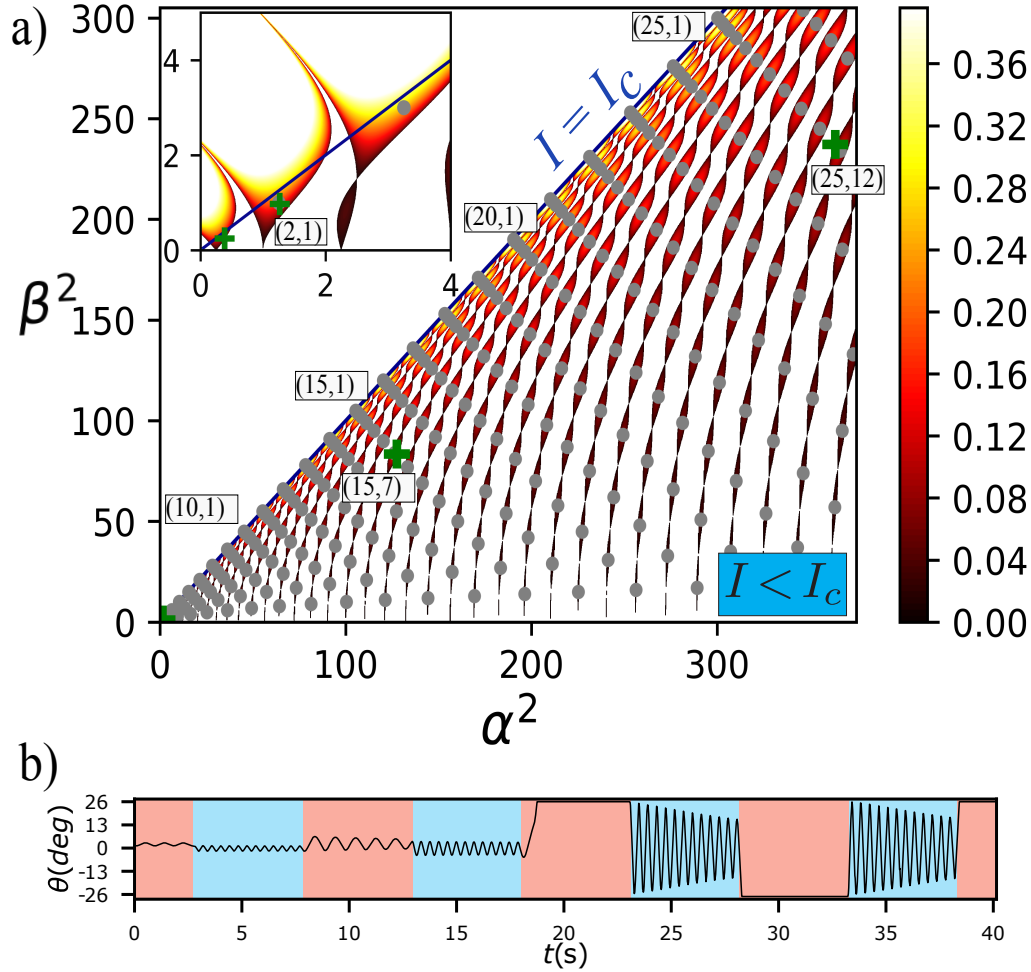


Figure 1.17: Controlling extreme parametric instabilities. a) Stability diagram of the Meissner equation in the extremely extended (α^2, β^2) space. Gray dots (m, n) represent the discrete geometrical relation of Eq (1.13). Inset zooms on the classic first instability regions. Green crosses represent the experimental parameters expressed in the (α^2, β^2) space shown in Fig 1.11 and Fig 1.17b). b) Experimental response of the $(25, 12)$ parametric amplification obtained using the geometrical relation of Eq (1.13). The experimental parameters are $\omega(0) \approx 15.15 \text{ rad.s}^{-1}$, $\omega(I) \approx 7 \text{ rad.s}^{-1}$ and $T \approx 10.16\text{s}$.

So, with the geometrical rule of Eq (1.13) we can trigger a precise parametric instability. One can choose the number of oscillations of the system during \mathcal{T}_1 (related to the value of m) and the number of oscillations during \mathcal{T}_2 (related to the value of n) and the values of (α^2, β^2) are deduced using Eq (1.13). Finally having the corresponding values of (α^2, β^2) , the values

of the experimental parameters can be deduced.

To show the use of the geometric rule of Eq (1.13) as a tool to trigger extreme parametric modulations we are using our electromagnetic pendulum. We fix the value of $m = 25$ and the value of $n = 12$. Using Eq (1.13) we deduce the corresponding values of $(\alpha^2 = 366.25, \beta^2 = 234.0)$. Then using Eq (1.11) we deduce the value of the experimental parameters ($T = 10.15\text{s}$, $\omega^2(I) = 50.6 \text{ (rad.s}^{-1}\text{)}^2$) which using Fig 1.9 correspond to $I \approx 0.62\text{A}$. We use these experimental parameters and we are able to obtain an extreme parametric response for $T = 10.16\text{s}$, $\omega^2(I) \approx 49 \text{ (rad.s}^{-1}\text{)}^2$. The experimental response is shown in Fig 1.17.b and the dimensionless experimental point $(\alpha^2 = 365.7, \beta^2 = 235.16)$ is represented with a green cross in Fig 1.17.a. We have a perfect agreement between the experimental values and the theoretical values of (α^2, β^2) . In the stability diagram in Fig 1.17.a the experimental point is perfectly placed in the instability pocket $(25, 12)$. Furthermore the experimental response in Fig 1.17.b shows that while the electromagnets are OFF (blue background) the response passes 25 times the minimum value of the potential energy (the zero axis) and while the electromagnets are ON (red background) the responses passes 12 times the maximum value of the potential energy before turning OFF the electromagnets again. Finally, this parametric pumping triggers a $2T$ -periodic limit cycle. Knowing there is an alternation between $2T$ and T periodic instability tongues, we infer that a $2T$ -periodic limit cycle is triggered when m is odd. This is validated with the experimental responses in Fig 1.11.a, Fig 1.11.c and Fig 1.17.b where we respectively have $m = 1, 15, 25$. Whereas in Fig 1.11.b $m = 2$ is even and we trigger a T -periodic limit cycle. Finally, since the instability region number follows $k = m + n - 1$, the response in Fig.1.11.b is actually located in the 36^{th} instability tongue as shown in Fig 1.11.a. An achievement since, to our knowledge, the record $k = 28$ was observed in a MEMS in 2016 [73].

3.2 Triggering and sustaining a natural oscillation

The previous study has been conducted with the assumption that $T_1 = T_2 = T/2$, i.e the periodic system spends the same amount on each oscillatory state. Instead of using this classical square wave modulation, we send an ‘‘impulse train’’ to trigger the system’s motion. This type of signal is illustrated in the sketch in Fig 1.18. This time the system is a longer time in its natural state defined by $\omega^2(0)$. Only at precise periods the electromagnets are turned ON during T_2 and the system is at the modulated frequency $\omega^2(I)$.

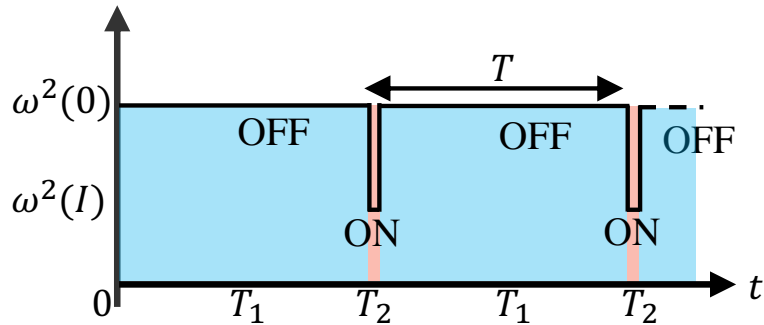


Figure 1.18: The square function as an ‘‘impulse train’’ with $T_1 = 0.98T$ and $T_2 = 0.02T$.

We still have a square wave modulation, thus the Meissner equation can still be used to define the stability diagram for this modulation [53]. The analytical resolution of the Meissner equation [77] takes in consideration the change of values for (T_1, T_2) so the stability diagram will adapt to the giving square wave modulation. The stability diagram for this type of modulation is presented in Fig 1.19.

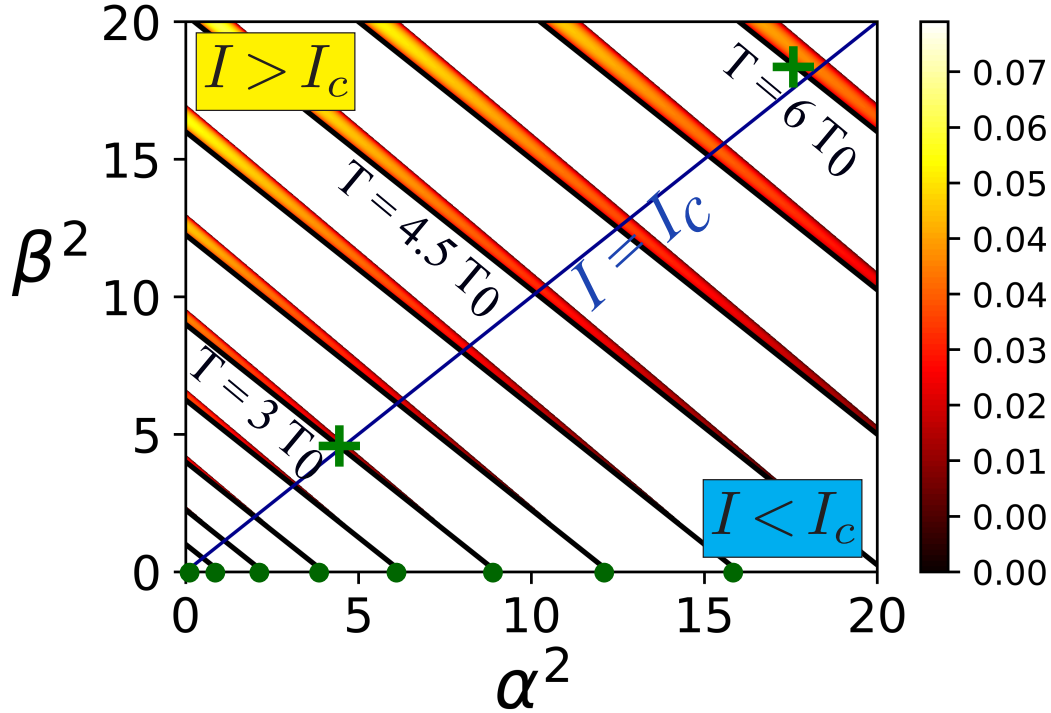


Figure 1.19: Stability diagrams for an “impulse train” with $T_1 = 0.98T$ and $T_2 = 0.02T$. Black lines show $T = 0.5kT_0$ and green dots show $\alpha^2 = (0.5k)^2$ where k is a positive integer. Green crosses represent the experimental modulation parameters associated with the response of Fig 1.20 and Fig 1.21.

Figure 1.19 displays the stability diagram for $T_1 = 0.98T$ and $T_2 = 0.02T$ (which corresponds to the square wave function represented in Fig 1.18). In particular when $T_1 \rightarrow T$, the instability pockets disappear and we have thin parallel lines for each instability parametric tongue with their tips still at $\alpha^2 = 0.5k$ as can be seen with the green dots [46] (Figure 1.19). Since the Meissner equation has an analytical resolution [77], the definition of the edge of the lines can be derived theoretically. By introducing the limits $T_1 \rightarrow T$ and $T_2 \rightarrow 0$ in the analytical calculation of the trace of the monodromy matrix ($Tr(\Phi)$) for the Meissner equation, we are able to deduce that the bottom edge of instability regions correspond to $\sqrt{\alpha^2 + \beta^2} = 0.5k$. They are represented by black lines in Fig 1.19. Physically, these black lines show that to parametrically amplify a giving system with a natural period T_0 , the period of modulation should be $T \approx 0.5kT_0$, where k is a positive integer representing the k -instability region. Figure 1.19 shows a perfect agreement between the black lines and the edges for every k unstable region. To amplify a response using an impulse train, we can use the defined black lines to deduce the value of the period of modulation T . However, when $T_1 \rightarrow T$ and $T_2 \rightarrow 0$ the growth rate (colour bar in Fig 1.19) decreases considerably if we

compare it with the stability diagram for the classic square wave modulation (Fig 1.17). To trigger parametric amplifications experimentally, we have to be close or even over the limit $I = I_c$, i.e we are making our system slightly divergent during a short period T_2 .

We put this theory to the test using our experimental setup: the electromagnets are almost continuously OFF ($T_1 \approx T$) and are turned shortly ON during T_2 with an electrical current I (Fig 1.18). The system is a locally stable pendulum, characterized by a harmonically damped oscillating response with natural period $T_0 = 2\pi/\omega(0)$, except every period T_2 where the local evolution function of the pendulum is shortly but drastically changed. The local evolution of the system was characterized in Fig 1.9.

First, we impose $T_1 = 3T_0 \approx 1220$ ms (with T_0 the natural period of the pendulum: $T_0 = 2\pi/\sqrt{g/l} = 412$ ms and its natural frequency $f_0 = 1/T_0 = 2.43$ Hz). Our camera records a maximum of 70 frames per second so the minimum value to assure a good recording of the period is 20 milliseconds. Also, it is important to point out that, to give enough time to the electromagnets to be turned ON and have an electromagnetic field surrounding the pendulum while ON, we cannot have $T_2 < 20$ ms. While testing the setup, we observed that below this value the electromagnetic field was not acting on the pendulum. Taking these considerations, we ensure $T_2 \approx 25$ ms which means we have $T_1 = 0.98T$ and $T_2 = 0.02T$ (the corresponding stability diagram is the one presented in Fig 1.19). Finally, we impose $I = 1.2$ A to have a positive growth rate. The experimental response and its corresponding FFT are shown in Fig 1.20.

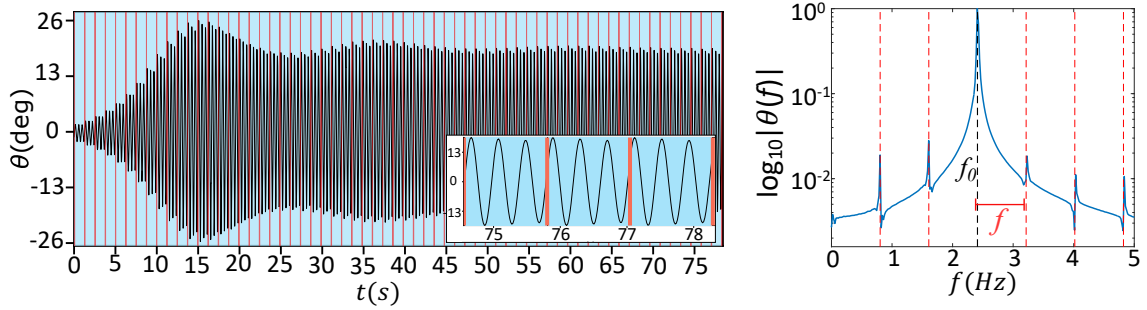


Figure 1.20: Triggering and sustaining a “natural oscillation” using parametric instabilities. Experimental response and the corresponding FFT of the permanent regime observed when the electromagnetic pendulum is OFF during $T_1 \approx 1.22$ s (blue background) and ON during $T_2 \approx 0.025$ s (red lines) with $I \approx 1.2$ A. Inset zooms on the T -periodic limit cycle. Black dashed line in the FFT represents the value of the natural frequency of the pendulum when the red ones represent the secondary harmonics $f_0 \pm hf$, where $f = 1/T$ and h is an integer.

The experimental response in Figure 1.20 shows that we are capable of parametrically amplify a response using an experimental “impulse train”. We have a transient regime during the first forty seconds of the response; after which we enter a permanent regime with a limit cycle highlighted in the inset in Fig 1.20. To understand this limit cycle we express the experimental parameters $\omega(0) = 2\pi f_0$, $\omega(I)$ and $\omega = 2\pi/T$ in the dimensionless space

(α^2, β^2) using Eq (1.11) and we report the experimental data (green cross) in the stability diagram in Fig 1.19. We find that the limit cycle of Fig 1.20 results from a parametric resonance of order $k = 6$, which is expected since the applied modulation period T is six time slower than half the natural period of the pendulum. Since k is even, we expect to trigger a T -periodic limit cycle. This is confirmed by the FFT of the experimental permanent regime in Fig 1.20 that shows spectral rays located every $f_0 \pm hf$ with h an integer and $f = 1/T$. Interestingly, the limit cycle is very close to a purely sinusoidal motion with a fundamental frequency f_0 since the amplitude of the secondary harmonics are no more than 3% of the fundamental one. As illustrated by the inset in Fig 1.20 that displays the last three periods of the recorded experimental response, the triggered limit cycle is nothing else but the free damped oscillation of the pendulum with natural period T_0 that is “reset” every $3T_0$ thanks to the synchronized impulse of input energy represented by red vertical lines.

To verify the robustness of this parametric pumping phenomenon, we now impose $T_1 = 6T_0 \approx 2463$ ms, $T_2 \approx 25$ ms and $I = 1.25$ A. The experimental response as well as the FFT of the permanent regime are presented in Fig 1.21.

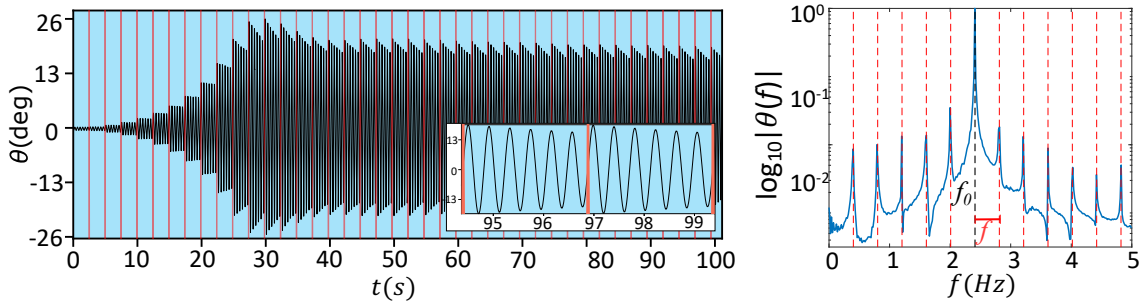


Figure 1.21: Triggering and sustaining a “natural oscillation” using parametric instabilities. Experimental response and the corresponding FFT of the permanent regime for $T_1 \approx 2.5$ s (blue background) and $T_2 \approx 0.025$ s (red background) with $I \approx 1.25$ A and an inset zooms on the T -periodic limit cycle. Black dashed-line in the FFT represents the value of the natural frequency of the pendulum and the red ones represent the secondary harmonics $f_0 \pm hf$, where $f = 1/T$ and h is an integer.

Same as for $T_1 = 3T_0$, we were capable to parametrically amplify the response. The response requires more time to be amplified because the value of T_1 is considerably larger than before, but once it has done so, a limit cycle can be maintained with a minimal input of energy. We are sending an electrical current during 25 ms every 2.5 s. Looking at the inset and the FFT in Fig 1.21 we see that the triggered limit cycle is the free damped oscillation of the pendulum with a natural period T_0 that is “reset” every $6T_0$. Because we let the system do more oscillations between every impulse, the damping on the response is much more noticeable. Also, in order to trigger the response we had to use an even larger value of the electrical current that for $T = 3T_0$, $I = 1.25 > I_c$. This is explained by the fact that the growth rate of the transient oscillations decreases with k , as mentioned in the stability diagram in Fig 1.19. This creates a limitation of the maximal k region we can trigger, because at one point the growth rate will not be enough to produce a proper exchange of energy and the instability

will not trigger.

We have experimentally demonstrated that a “natural limit cycle” can be triggered using parametric instabilities with an impulse with $T_1 \approx 0.5kT_0$. To increase the maximum order of observed parametric resonance k , one could increase the Q factor in the setup or in our case the value of electrical current I . Interestingly, unlike the classic resonance phenomenon, the bandwidth of this parametric resonance, i.e. the width of the instability region of Fig. 1.19 depends on the “width” of the imposed impulse train (value of T_2) and not on the Q factor. The shorter the impulse train, the shorter the periodic energy exchange (spend less energy) and the thinner the instability region. This is an exciting idea because if the period of modulation is slightly changed then the response is no longer amplified. This could be used to precisely trigger the response of a system or use it as an atomic scale.

Another useful property is the tuning capabilities offered by this concept. As presented by the experimental diagram in Fig 1.9, by externally modulating the system we can explore the full stability diagram (cases $A - D$ in Fig 1.4). We have shown that we are able to trigger and sustain the natural oscillation of the system by sending a modulation between $\omega^2(0)$ and $\omega^2(I)$ (Fig 1.18). If we modulate the system between two different values of the electrical current (I_1 and I_2), we obtain a modulation between $\omega^2(I_1)$ and $\omega^2(I_2)$. By doing so, theoretically, one could efficiently trigger and sustain any sinusoidal oscillation. Experimentally, the range of frequencies will be delimited by $\omega(0)$ (the geometry of the system) and almost 0, as suggested by the characterization done in Fig 1.9.

For systems like MEMS that are tiny beams or plate resonators with very large Q factors (because they operate in Ultra High Vacuum [72, 73, 75]) and driven by periodic electrostatic fields, an application of this particular parametric pumping could allow to efficiently generate highly super-harmonic sinusoidal signals with extremely tunable fundamental frequencies.

2| Anti-resonance tongues: stabilising in synchrony a naturally unstable system

Contents

1	Physical framework: systems with a naturally unstable equilibrium	49
1.1	Linear stabilization using parametric modulations	49
2	Classical attempts to stabilize a natural equilibrium system using parametric modulations	51
2.1	Macroscopic example: inverted pendulum	51
2.2	Microscopic example: Ion trap	53
2.3	Discussion	55
3	Experimental stabilization beyond the Kapitza approach	56
3.1	Experimental setup	56
3.2	Experimental stabilisation	61
4	Numerical study of the tip of the stability regions	64
4.1	Basin of attraction	64
4.2	Study of the responses	65
4.3	Resolution in a unit cell	67
5	Pseudo-analytical solutions at the tip of the stability tongue	69
5.1	Analog problem	69
5.2	Pseudo-analytical solutions near the tip of the stability tongue	72
5.3	Re-introducing the second time scale to the master curves	73
6	Experimental validation of the master curves: synchronized dynamical stabilization	75
6.1	Experimental stabilization at $T_D = 25\%T$	76
6.2	Experimental stabilization at $T_D = 70\%T$	77

In this chapter we study the second main functionality of parametric instabilities: the dynamical stabilization of a naturally unstable system. To do so, we focus on the study of the stability tongues (anti resonance tongues).

One of the most famous system showcasing the use of a parametric modulations to stabilize a naturally unstable system is the study of Kapitza's inverted pendulum [65]. He showed that by vertically vibrating the inverted pendulum, stabilization can be achieved if the frequency of oscillation is sufficiently fast as compared to the natural time scale of the system. This study also gives a theoretical limit to deduce the parameters to dynamical stabilize a system [65]. This concept can be apply in a plethora of physical systems: from the study of the levitation of fluids [78] and the suppression of flutter in airplanes [40] to the trapping of particles [67, 79] or atomic clocks [80].

These systems employ the theoretical Kapitza limit, which is located at the bottom edge of the first stability region and is therefore only valid for small amplitudes of modulations (Fig 8 of the Introduction). Moreover, the Kapitza limit is only valid for fast frequencies of modulations, i.e the system receives a large amount of energy per period to be stabilize. If we leave the Kapitza approach, stabilization could be achieved at lower frequency of modulation and the spending of energy should decrease. The modulation is sent at precise times to ensure stabilization. So, exploring beyond the Kapitza limit means we could dynamically stabilize a system spending the least amount of energy.

To investigate this idea of going beyond the Kapitza limit, we are conducting a theoretical and experimental study. First, we establish the physical systems we are analysing. Following it, an analysis of the implementation of dynamical stabilization in a couple of mechanical systems is presented. One case at the macroscopic scale with the Kapitza's pendulum [65, 66] and one example at the microscopic scale with the use of ion traps [67, 79]. Studying the similarities of these experiments and with our experimental knowledge of the previous chapter, we developed an experimental setup to go beyond the Kapitza approach.

We achieved experimental stabilization of a natural unstable system beyond the Kapitza limit. Nevertheless, leaving the Kapitza limit means we have thinner stability regions making it complicated to reach the tip of the stability regions experimentally. These are regions of interest because at the tips we spend the least amount of energy to stabilize a system. At this point we do a numerical study of the response at the tip of the stability region. This numerical analysis demonstrates that our system's response can be analysed as a unit cell with boundary conditions. These observations allow us to deduce a pseudo-analytical solution to deduce the parameters to stabilize the system without having to use the stability diagrams, avoiding the difficulty of the thin size of the regions. With this theoretical study we develop pseudo analytical solutions (master curves), that are valid in the entire stability regions, not only at the tip.

Finally, these theoretical master curves are validated with our experimental proof of concept. We can stabilize a system with parameters closer to the tip of the stability region and spending the least amount of energy. This new approach of dynamical stabilization could open the door to new functionalities in mechanics and in our reasoning of thinking experimental setups to use parametric instabilities.

1 Physical framework: systems with a naturally unstable equilibrium

Physically, any nonlinear dynamical system having a natural unstable equilibrium can be defined by having a potential energy with at least a negative curvature [81, 82]. For example, an inverted pendulum is a nonlinear system with a natural unstable equilibrium. The evolution of this potential is presented in Fig 2.1. The equilibrium position of the mass is unstable because a perturbation will make it depart from the original position and not be able to come back, goes down the hill.

We can also be interested in the linear study of this potential, i.e the small perturbations. The linear study is represented by the zoom near the mass in Fig 2.1. In this scenario we suppose the curvature (curve of the hill) is $-\alpha^2$. Our goal is that after applying a small perturbation to the natural equilibrium, we use parametric modulations to keep the mass on top of the hill (near its equilibrium position).

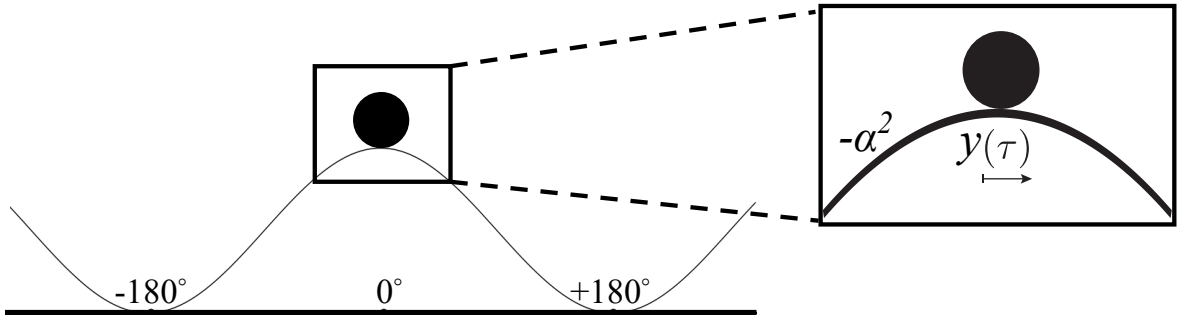


Figure 2.1: Schematic representation of the nonlinear potential of a system with a natural unstable equilibrium. We zoom in the closest region of the unstable equilibrium (small displacements) where the linear analysis take place. $-\alpha^2$ represents the negative value of the curvature.

With the linear approximation we can use Floquet theory to deduce the stability diagram of the system and obtain the anti-resonance tongues to stabilize the system [54]. However, the linear study only presents the existence of some initial conditions or perturbations for which the true nonlinear system will be stable. Linear analysis is necessary but not sufficient to know whether the true system will be stable because we need to know what size of imperfection or perturbation is acceptable (basin of attraction) [3]. Thus, in this Chapter we are conducting a linear and nonlinear study.

1.1 Linear stabilization using parametric modulations

We have a system with an unstable equilibrium. The curvature is negative, and its value is defined by $-\alpha^2$, represented by a black line in Fig 2.2. A periodic function $g(\tau)$ is used to modulate this curvature and the parametric amplitude is β^2 . The system is then periodically modulated between $-\alpha^2 + \beta^2$ and $-\alpha^2 - \beta^2$ respectively represented by a red dashed line and a blue dashed line in Fig 2.2.

To stabilize the system, the curvature of the potential needs to be positive during the modulation. If the curvature is positive then the system is an oscillatory system where the equi-

librium point is stable [81]. A positive curvature can occur only if $\beta^2 > \alpha^2$, meaning $-\alpha^2 + \beta^2 > 0$ (dotted red line in Fig 2.2). In this case, if the mass is disturbed it will oscillate and come back to the equilibrium position. During the other part of the modulation the system is a diverging system when $-\alpha^2 - \beta^2$ (dotted blue line in Fig 2.2).

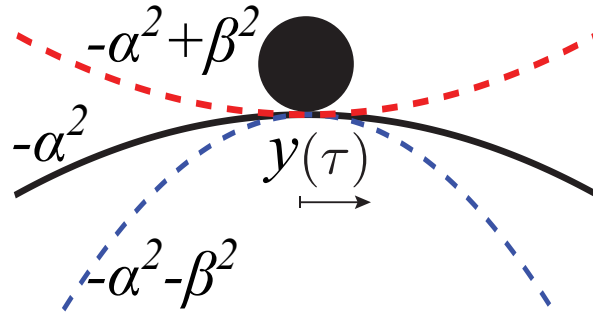


Figure 2.2: Schematic representation of the linear potential of a mass in an unstable equilibrium stabilized using parametric modulations. The black line represents the natural negative curvatures of the system $-\alpha^2$, blue dashed line shows the modulation at $-\alpha^2 - \beta^2$ and red dashed line shows the modulation $-\alpha^2 + \beta^2$ which can have a positive curvature if $\beta^2 > \alpha^2$.

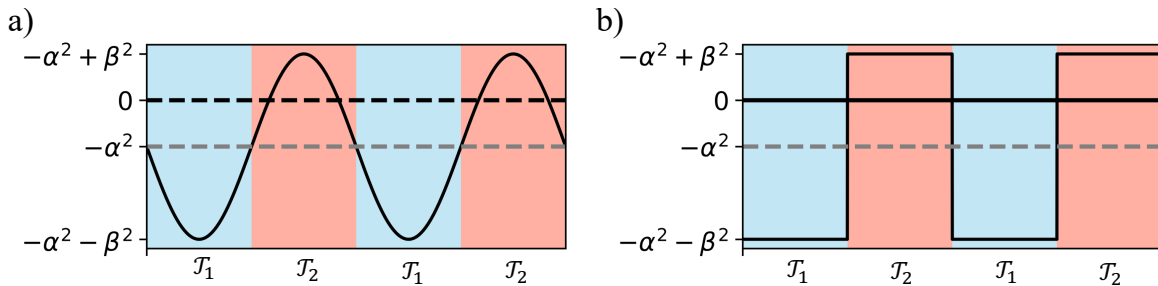


Figure 2.3: Shape of two different parametric modulation functions to stabilize an unstable equilibrium. To have a positive curvature we need $\beta^2 > \alpha^2$. a) 2π -periodic harmonic modulation of the shape $g(\tau) = -\beta^2 \cos \tau$. b) 2π -periodic square wave modulation equal to $-\beta^2$ during $\mathcal{T}_1 = \pi$ and equal to $+\beta^2$ during $\mathcal{T}_2 = \pi$.

Figure 2.3 represents how different periodic functions can physically stabilize a natural unstable equilibrium. Figure 2.3.a shows the modulation of the curvature of the potential using a harmonic modulation and Fig 2.3.b shows the modulation with a square wave function. Here $\beta^2 > \alpha^2$ so $-\alpha^2 + \beta^2 > 0$. It is interesting to observe that no matter the used value for β^2 , the diverging state will always have a steeper curvature. This is seen by the distances to the zero value in the y -axis (black dotted line in Fig 2.3). In the examples in Fig 2.3 we have $-\alpha^2 = -1$ and $\beta^2 = 2$ giving us $-\alpha^2 + \beta^2 = 1$ (oscillatory state) and $-\alpha^2 - \beta^2 = -3$ (diverging state). This can also be seen in Fig 2.2 where the blue dotted line (diverging state) is sharper than the red dotted line (oscillatory state). Thus, we find that the stabilization of a natural unstable system is possible but difficult.

The system described in Fig 2.2 is a linear time-varying periodic system with an unstable equilibrium. The equation to describe its motion can be written:

$$\frac{d^2 y(\tau)}{d\tau^2} + (-\alpha^2 + \beta^2 g(\tau)) y(\tau) = 0, \quad (2.1)$$

which is the general dimensionless expression of an ordinary differential equation with a parametric coefficient [46]. With this equations we can use Floquet's theory [54] and have the stability diagram of the system. Figure 2.4 shows the stability diagram of the Mathieu equation focusing on the first stability regions with also negative values of $-\alpha^2$. As we have seen with Fig 2.2 and Fig 2.3, to stabilize the system, we need to have $\beta^2 > \alpha^2$ which is the case "B" of the stability diagram in Fig 2.4.

The theoretical Kapitza limit [65] is defined as $\beta^2 = \sqrt{2\alpha^2}$ and it is represented by a green line in Fig 2.4. It is an indicator for small values of β^2 , it correctly follows the lower edge of the first stability region until $\beta^2 \approx 0.5$. This theoretical limit is no longer valid for larger values of the modulation. Nevertheless, Kapitza's theoretical limit has been applied in various systems. So, we want to understand how different dynamical systems can use parametric modulation to stabilize their naturally unstable equilibriums.

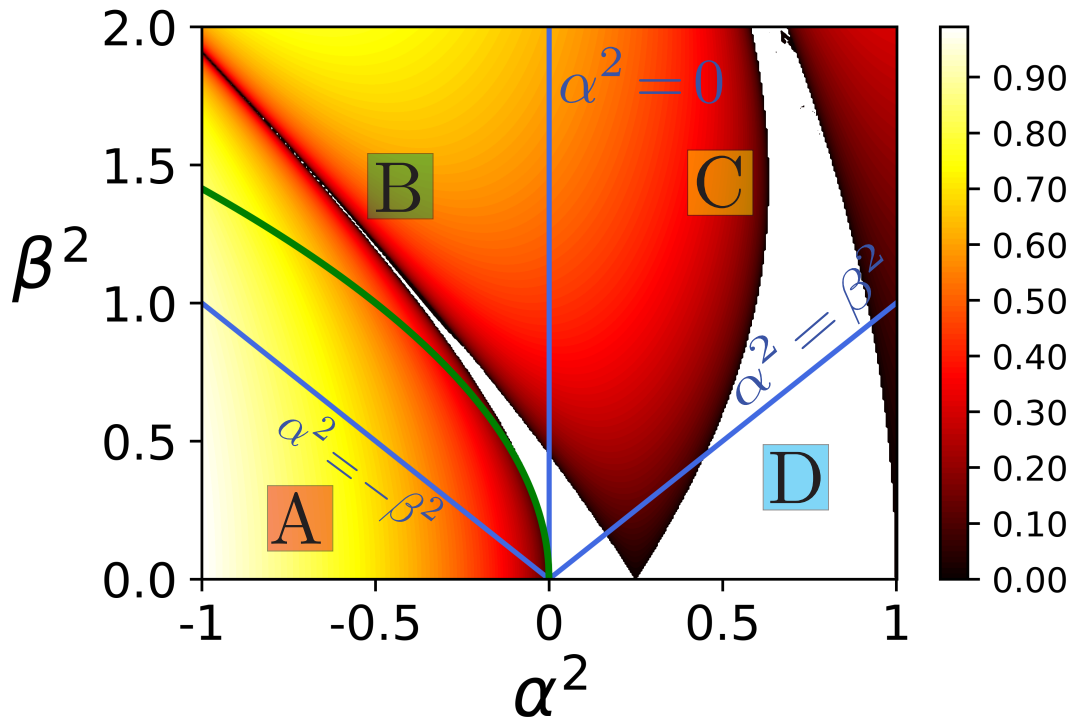


Figure 2.4: Linear stability diagram for the Mathieu equation, representing the evolution of the maximum value of the real part of the Floquet exponent. Coloured regions are the instability tongues and white regions are the stability tongues. Green line represents the Kapitza limit $\beta^2 = \sqrt{2\alpha^2}$.

2 Classical attempts to stabilize a natural equilibrium system using parametric modulations

2.1 Macroscopic example: inverted pendulum

The first study is on the famous Kapitza's pendulum [65]. We are interested in this experiment not only because it is a pioneer work of the domain but because the physical insights

are applicable in a variety of systems. The idea presented by Kapitza is to stabilize an inverted pendulum by vertically oscillate the pivot point at a fast frequency of oscillation larger than the natural time scale of the system. A schematic representation of the current setup is presented in Fig 2.5, where the inverted pendulum is vertically modulated by a driving frequency ω and an acceleration of excitation Γ .

This concept can be applicable in a plethora of systems. For example Apffel et. al [78] adapted this physical insights to levitate a fluid. They use the Rayleigh–Taylor instability, which occurs at the interface between two fluids whenever a denser fluid is placed over a lighter one [83, 84], and by vertically oscillate the system with a fast frequency they achieved dynamical stabilization of the lower horizontal interface of the liquid.

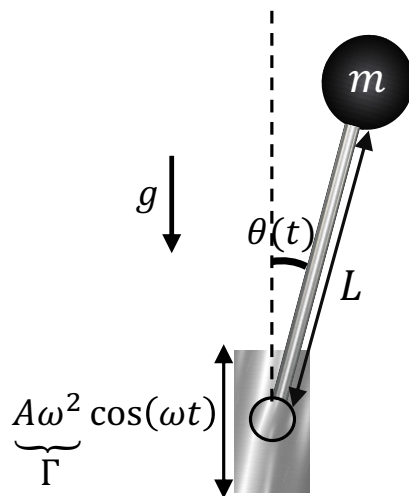


Figure 2.5: Schematic representation of the experimental setup of an inverted pendulum. The inverted pendulum is placed over a shaker with a frequency of excitation ω , an amplitude of excitation A and an acceleration of excitation $\Gamma = A\omega^2$. The pendulum is characterized by its length L , mass m and $\theta(t)$ is the angular displacement measured from the vertical position. The gravitational acceleration is g

Based on the multiple work conducted on the inverted pendulum [46, 65, 85], the undamped equation of motion is well established and reads

$$I \frac{d^2 \theta(t)}{dt^2} - mL (g + A\omega^2 \cos \omega t) \sin \theta(t) = 0, \quad (2.2)$$

where $\theta(t)$ is the angular displacement measured from the vertical position, L is the length of the pendulum, m the mass and I the moment of inertia. The external modulation is characterized by the frequency of modulation ω , the amplitude of modulation A and the acceleration of modulation $\Gamma = A\omega^2$. Eq (2.2) can be linearised near the equilibrium position, the moment of inertia is approximated as $I \approx mL^2$ and upon the change of variable $\tau = \omega t$, Eq (2.2) can be written in the standard dimensionless form of Eq (2.1) with a harmonic modulation, giving us the Mathieu equation [48, 46]

$$\frac{d^2 \theta}{d\tau^2} + (-\alpha^2 - \beta^2 \cos(\tau)) \theta(\tau) = 0 \quad (2.3)$$

where $\alpha^2 = \frac{g}{L\omega^2}$, and $\beta^2 = \frac{\Gamma}{\omega^2} \frac{1}{L}$.

For this system, an experimental example is presented in the work of Smith [66]. In this setup Smith opted to use a small pendulum due to some experimental limitations: difficulties with the transducer (too powerful and noisy) and easy to disturb the system using the operator's finger[66]. The setup consists on a pendulum with length $L = 8 \times 10^{-3}$ m, mass $m = 0.19 \times 10^{-3}$ kg and the gravitational acceleration is $g = 9.81$ m.s⁻². The experimental parameters used by Smith [66] can be translated into the dimensionless space (α^2, β^2) . They are presented in Table 2.1 and the experimental point is reported in the stability diagram in Fig.2.7.

Table 2.1: Experimental parameters used by Smith [66] and the corresponding values of the dimensionless modulation parameters α^2 and β^2 . This experimental data is presented in Fig.2.7.

Experimental parametric parameters	α^2	β^2
$f = 157.17$ Hz ; $\Gamma = 61.3$ m.s ⁻²	0.05	0.31

2.2 Microscopic example: Ion trap

The idea of implementing dynamical stabilization into microscopical systems was just a matter of time. During the 1950s Wolfgang Paul developed the technique and developed the first experiments on trapping atoms and charged particles using electric quadrupoles fields [67]. This work awarding him, Norman F. Ramsey and Hans G. Dehmelt the Nobel prize in physics in 1989 [86]. These concepts lunched a great number of experimental studies. Some of the most famous ones are the experimental measurements of Serge Haroche [87, 88]: they control and measure trapped photons or particles of light by sending atoms through a trap. We can also name the experimental work of David J. Wineland [89, 90], who takes the opposite approach: he traps electrically charged atoms, or ions, controlling and measuring them with light or photons. They were awarded the Nobel prize in physics in 2012 “for ground-breaking experimental methods that enable measuring and manipulation of individual quantum systems” [91]. This theory has applications in ion traps and mass spectrometry [41] and more recently in the entanglement of electrons in quantum computers [92, 93] and the development of atomic clocks [80].

In the following study, we describe a Paul's trap (ion trap) [67] which consists on isolating a particle using an electric field. To achieve it, an average confining force around the particles is imposed by periodically changing the sign of the electric field. This is a quadrupole ion trap and a sketch is presented in Fig 2.6. A quadrupole can be created by using four hyperbolically shaped electrodes linearly extended where the opposite one has the same sign but different from the one besides it (Fig 2.6).

In cylindrical coordinates and taking in consideration the Laplace condition [67], the expression of the potential is

$$\phi = \frac{\phi_0 (r^2 - 2z^2)}{r_0^2 + 2z_0^2}. \tag{2.4}$$

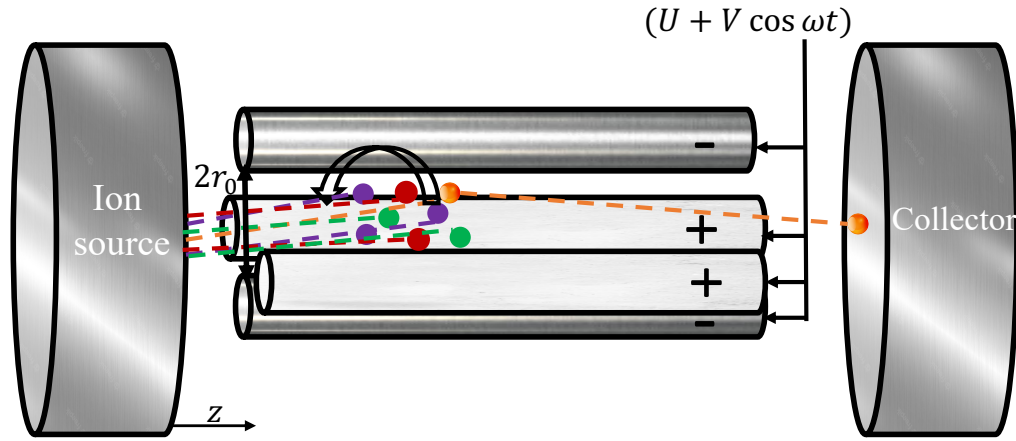


Figure 2.6: Schematic view of the quadrupole mass spectrometer or ion trap. Four quadrupoles of opposite signs which have a dc voltage U are periodically modulated by a rf voltage V with driving frequency ω . With a particular value of ω we can filter and collect a particular particle (orange one in this example) or we can trap a particular particle.

ϕ_0 is the voltage applied between the electrode pairs, r_0 is the radius of the particle and $2z_0 = r_0$. A periodic voltage of the shape $\phi_0 = U + V \cos \omega t$ is applied where U is the dc voltage, V is the rf voltage and ω is the driving frequency. Based on the work of [67, 79], the differential equations of the motion of a particle of a charge-to-mass ratio e/m under this periodic potential field read

$$\begin{aligned} \frac{d^2 z(\tau)}{d\tau^2} + \frac{e U}{m z_0^2} z - \frac{e V}{m z_0^2} z \cos \omega t &= 0, \\ \frac{d^2 r(t)}{dt^2} - \frac{e U}{m z_0^2} r - \frac{e V}{m z_0^2} r \cos \omega t &= 0. \end{aligned} \quad (2.5)$$

The motion of the particles is over the (z, r) plane and Eq (2.5) shows that their motion on each direction is independent from each other. For each component, by introducing the change of variable $\tau = \omega t$, Eq (2.5) can be reduced in the dimensionless form of the Mathieu equation [48, 46]:

$$\begin{aligned} \frac{d^2 z(t)}{dt^2} + (\alpha^2 - \beta^2 \cos \tau) z(\tau) &= 0, \\ \frac{d^2 r(t)}{dt^2} + (-\alpha^2 - \beta^2 \cos \tau) r(\tau) &= 0, \end{aligned} \quad (2.6)$$

where $\alpha^2 = \frac{Ue}{mr_0^2\omega^2}$, and $\beta^2 = \frac{Ve}{mr_0^2\omega^2}$.

The expressions of α^2 and β^2 in Eq (2.6) show us that if we work at fixed values of r_0, U, V, ω the ratio $\beta^2/\alpha^2 = V/U$ is independent of the mass of the particle m . So the different ions with a same mass have the same value β^2/α^2 in the (α^2, β^2) stability diagram [67]. If U and V are simultaneously and proportionally changed in a way that the ratio β^2/α^2 remains constant, we can browse the different masses of the particles and filter the one we wish to trap. Thus, by varying the imposed voltage, we have a mass spectrometer or an ion trap. In this case

the motion is in 2D, along the z -axis and the r -axis, and the motion of both axis are defined by the Mathieu equations (Eq (2.6)), so the stability region to stabilize this system is the superposition of the two diagrams, as it can be seen in [41, 67].

An experimental study of an Ion trap is presented in the work of Wuerker [41]. The particles he used are charged iron and aluminium particles. The particles have a radius of $r_0 \approx 7.23 \mu\text{m}$ and the charge-to-mass ratios e/m are between 5.3×10^{-3} and $6.25 \times 10^{-3} \text{ C.kg}^{-1}$. The rf voltage $V = 500\text{v}$ is fixed but the driving frequency ω and the dc voltage U can be varied. The experimental parameters used can be translated into the dimensionless space (α^2, β^2) using Eq (2.6). These experimental values are presented in Table 2.2 and are reported in the stability diagram in Fig.2.7 by blue triangles.

Table 2.2: Experimental parameters used by Wuerker [41] and the corresponding values of the dimensionless modulation parameters α^2 and β^2 . This experimental data is presented in Fig.2.7.

Experimental parametric parameters	α^2	β^2
$U = 0.0 \text{ V} ; \omega = 1256 \text{ rad.s}^{-1} ; e/m = 5.3 \times 10^{-3} \text{ C.kg}^{-1}$	0.0	0.232
$U = -77 \text{ V} ; \omega = 930 \text{ rad.s}^{-1} ; e/m = 6.25 \times 10^{-3} \text{ C.kg}^{-1}$	-0.045	0.50
$U = -45 \text{ V} ; \omega = 930 \text{ rad.s}^{-1} ; e/m = 6.25 \times 10^{-3} \text{ C.kg}^{-1}$	-0.072	0.50

2.3 Discussion

As presented in the two previous examples, the dynamical stabilization of a naturally unstable system using parametric modulation is possible in multiple domains in physics. We presented one at the macroscopic scale with Kapitza's pendulum and one at the microscopic scale with an ion trap. The experimental results are translated into the dimensionless space (α^2, β^2) and are presented in the stability diagram in Fig 2.7. As expected, the experimental points are in a stable region (white region) and, more precisely they are in the first stability region. Moreover, we do have negative values of α^2 and we have $\beta^2 > \alpha^2$, correctly placing us in the case "B" of the stability diagram. Furthermore, we know that for this specific region of the stability diagram, stabilizing a naturally unstable system is challenging. As we can observe in Fig 2.7, the experiments achieve stabilization only at the first stability region and close to the theoretical Kapitza limit [65], represented by a green line in Fig 2.7.

Finally, it is interesting to observe that in both experimental setups the dynamical stabilization is obtained by modulating the system using an external field (different from Chapter one where they also use geometrical modulation to enhance a response). We have seen that modulating using an external field (electrical field, electromagnetic field) is the most advantageous technique to achieve further regions. So, it is interesting that in neither example they leave the Kapitza limit (first stability region). This means that to explore further stability regions, we need to try new frequencies of modulation that are closer to the natural time scale. Also, we need to be able to do strong modulations of the natural time scale of the system. Using our experimental knowledge developed in the first Chapter, we present a new experiment to explore dynamical stabilization beyond the Kapitza approach.

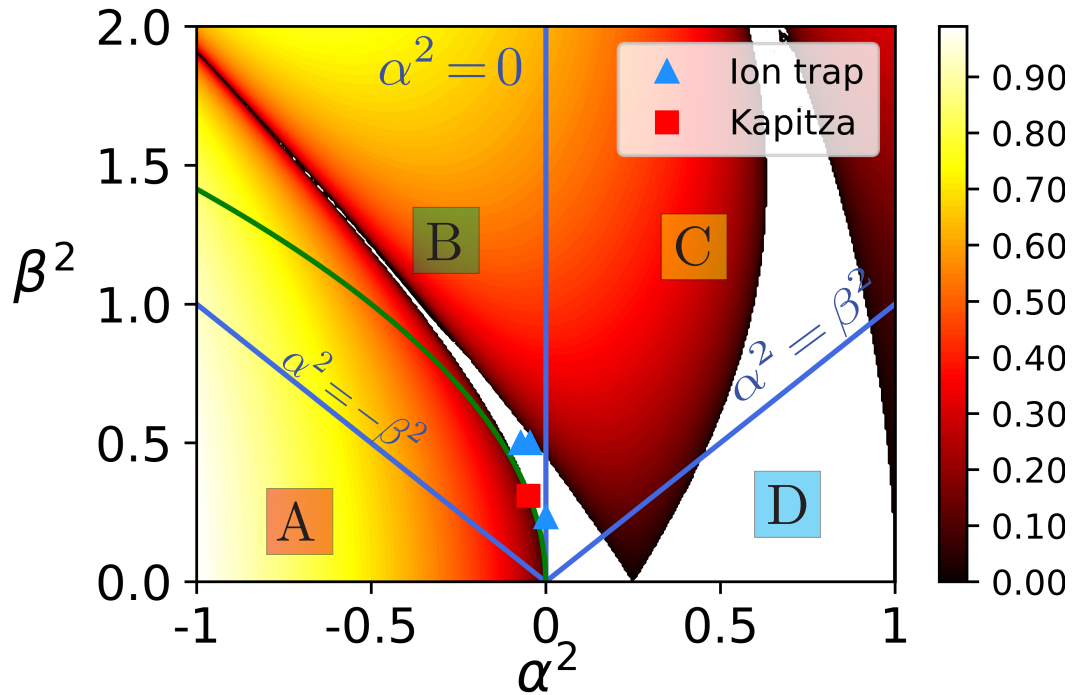


Figure 2.7: Linear stability diagram of the Mathieu equation in the dimensionless modulation space (α^2, β^2) with experimental data points trying to stabilize a natural unstable system. Blue triangles represent the experimental result of the Wuerker [41] and red square is the experimental results of the inverted pendulum done by Smith [66]. Green line represents the Kapitza limit $\beta^2 = \sqrt{2\alpha^2}$ for $\alpha^2 < 0$.

3 Experimental stabilization beyond the Kapitza approach

Our goal is to experimentally stabilize a macroscopic system beyond the theoretical Kapitza limit [65], i.e. with a frequency of modulation close to the natural time scale of the system. To do so, first the experimental setup is presented with the different parametric parameters used for the stabilization. In our case it is an electromagnetic inverted pendulum modulated by a square wave function, and the parametric parameters are the electrical current I and the period of modulation T . Then we characterize how the electrical current I affects the natural time scale of the system. Once this is properly understood, we fix a value of the electrical current I and we send different T -periodic square wave modulations to try to stabilize the system. Finally, we define a numerical model, and we compare them to validate our experimental results and we analyse the frequency of modulation used and observe that the value of the electrical energy on the system decreases the further we are from the Kapitza approach.

3.1 Experimental setup

With Chapter 1, we now know that to take advantage of high order parametric tongues (either stable or unstable) we need a system where the dynamics and the modulated parameter have an uncomplicated relationship. Most importantly we need a system where the natural time scale of the system can be drastically varied with ease and without modifying the geometry. To honor one of the pioneers of this domain we use an inverted pendulum. However, instead

of using a shaker like Kapitza's pendulum, our pendulum has a metallic marble symmetrically placed under an attracting electromagnet. The experimental system and a schematic representation of the electromagnetic inverted pendulum are represented in Fig 2.8. The metallic marble has a radius of 0.95 cm and it is attached to a rod of length $l = 5.2$ cm. The rod is then connected to another rod allowing him to oscillate from left to right. The marble is centred with the electromagnet (with typical holding force of 1000 N) at a distance $h = 6$ mm. By means of a Controllino card we can turn ON and OFF the electromagnet by sending a T -periodical square wave function. For the recording of the experimental responses, we place the electromagnetic inverted pendulum in front of a white LED to enhance the contrast and record the motion of the metallic marble with a Basler camera CMOS capable to record until 220 frames per second.

The electromagnet is connected to a generator where we can select the value of the electrical current I . The electrical current is responsible of the intensity of the electromagnetic force near the inverted pendulum. The stronger the value of I the stronger the electromagnetic field. We know the typical diverging time scale of the system is defined as $2\pi/\omega_0 = 2\pi/\sqrt{g/l}$ where g is the gravitational acceleration and l it is the length of the rod. By turning ON the electromagnet, the electromagnetic force will modify the effective gravitational field near the inverted pendulum, directly affecting the natural time scale of the inverted pendulum.

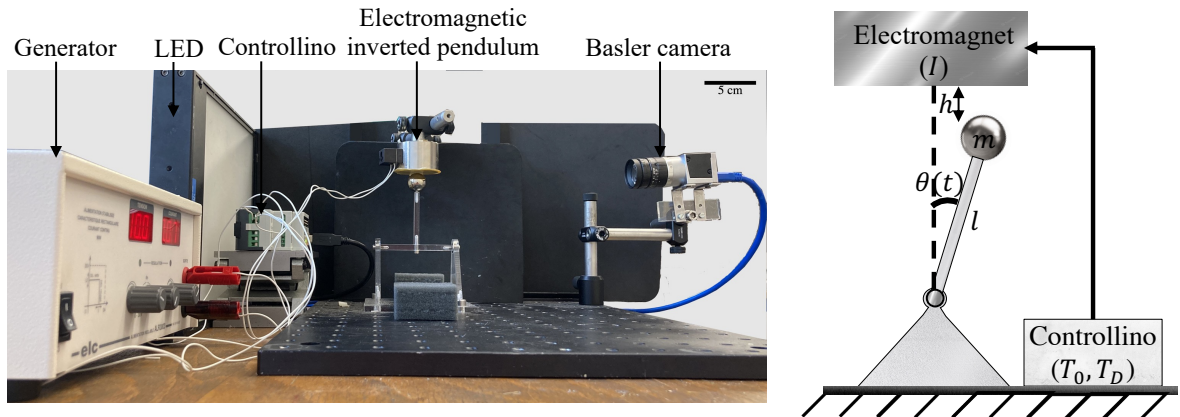


Figure 2.8: Experimental macroscopic setup. The system is a planar inverted pendulum of length l with a metallic marble that is symmetrically placed under an attracting electromagnet whose attracting force depends on the imposed electrical current I . An Arduino card allow us to send a T -periodic function to turn ON and OFF the electromagnet during T_O and T_D respectively.

Characterization of the system

We first need to characterize how the electromagnetic field affects the natural frequency of the system, i.e how the control parameter I affects the system. By varying the electrical current I the inverted pendulum is under various electromagnetic fields. This is translated as an effective gravitational field g_{eff} surrounding the inverted pendulum. This effective gravitational field will then change the curvature of potential energy of the system (Fig 2.9). When the electrical current is close to zero ($I = 0$), Fig 2.9.a, the system has a natural negative

curvature: any perturbation will make the mass go down the hill and cannot come back to its equilibrium, the system diverges. While the electromagnet is ON, there is a competition between the electromagnetic force (pulling up) and the gravitational force (pulls down). This is translated by a smoother curvature of the potential as presented in Fig 2.9.b. Then at some critical value $I = I_c$, the electromagnetic force is larger than the gravitational force and the system will have a positive curvature: a small perturbation will make the system oscillates near this equilibrium position and does not leave it (oscillatory system), as shown in Fig 2.9.c.

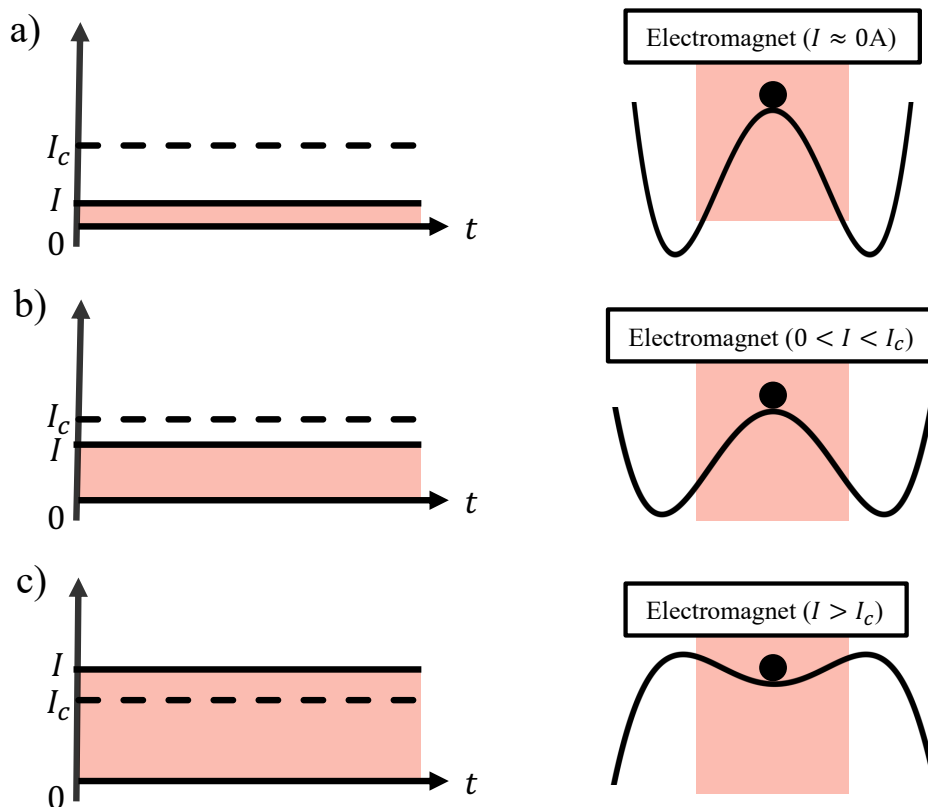


Figure 2.9: Three continuous signal with different values of the electrical current I and a sketch of the corresponding shape of the potential energy modulated by the electromagnetic field. After a critical value I_c the electromagnetic force is stronger than the gravitational force. a) $I \approx 0$ A the system has a natural negative curvature. b) $0 < I < I_c$ the negative curvature is less steep; the electromagnetic force is stronger. c) $I > I_c$ the system has a positive curvature; the system has a stable equilibrium with an oscillatory response.

With the parameter I we can change the effective gravitational field near the pendulum. We introduce the scalar $\omega(I) = \sqrt{g_{eff}}/l$ to characterize the experimental evolution of the frequency of oscillation for a giving value of I . This scalar represents the natural time scale of the electromagnetic inverted pendulum and give us the effect of the modulation of the local gravitational field in our system.

To characterize the evolution of $\omega(I)$ we use the Controllino card to send a continuous signal (electromagnet is ON) (Fig 2.8). We fix a value of the electrical current I and we keep the inverted pendulum at its unstable equilibrium by holding it from the rod. We let the pendulum go and we record the response of the system. The recording and post processing of

the motion of the metallic marble are the same as the one used in Chapter 1. Finally, it is important to always stay under the electromagnet, so that the electromagnetic force is as uniform as possible over the inverted pendulum. To do so the initial condition must be smaller than 10° . Different experimental responses are presented in Fig 2.10 and every response is recorded using 150 frames per second.

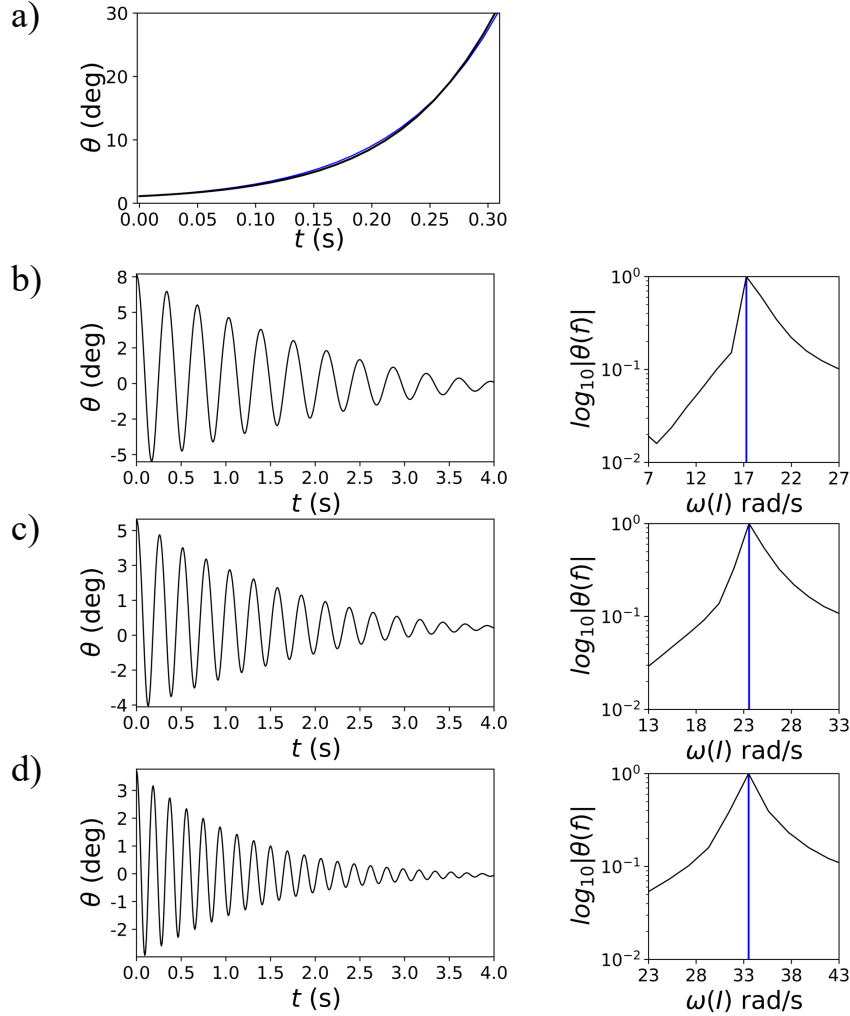


Figure 2.10: Experimental responses of the inverted electromagnetic pendulum for different values of the control parameter I . a) $I = 0$ A: diverging response characterized by the natural frequency $\omega(0)$. We fit an exponential to deduce its value, $\omega(0) \approx -11$ rad.s $^{-1}$. b) $I = 0.45$ A: oscillatory response, i.e we have crossed the I_c limit. We have $\omega(0.45) \approx 17$ rad.s $^{-1}$. c) $I = 0.55$ A: faster oscillatory response with $\omega(0.55) \approx 23$ rad.s $^{-1}$. d) $I = 0.70$ A: even faster oscillatory response, we have $\omega(0.70) \approx 33$ rad.s $^{-1}$.

Fig 2.10.a shows the experimental response for the natural case: when the local gravitational field is not modulated, i.e there is no electrical current $I = 0$ A (there is no local electromagnetic field). The system should be an inverted pendulum diverging with a natural frequency $\omega_0 = \sqrt{g/l} \approx 12$ rad.s $^{-1}$. As expected, we observe a diverging response. The experimental response is close to an exponential, thus we deduce $\omega(I)$ fitting an exponential

of shape $\theta(0)e^{\omega(I)t}$. We deduce that $\omega(I = 0) \approx -11 \text{ rad.s}^{-1}$ which is in good agreement with the value calculated with the geometrical parameters of the system. We then modulate the local gravitational field surrounding the pendulum $I \neq 0$ (Fig 2.10.b-d). The experimental response for $I = 0.45 \text{ A}$ is presented in Fig 2.10.b. We have an oscillatory response meaning the electromagnetic force is stronger than the gravitational force. So, the inverted pendulum is stabilized and the shape of the local potential energy is the one described in Fig 2.9.c (positive curvature). Doing a Fast Fourier Transformation (FFT) of the experimental response we observe that $\omega(0.45) \approx 17 \text{ rad.s}^{-1}$ which is higher than $\omega(0)$. For larger values, the system should continue to have an oscillatory response. And because the electromagnetic field is stronger when I increases, the value of the positive curvature of the potential should increase which this is translated by an increase of $\omega(I)$. This is validated in Fig 2.10.c-d, where respectively the electrical current is $I = 0.55 \text{ A}$ and $I = 0.70$ and $\omega(I)$ increases from $\omega(0.55) \approx 23 \text{ rad.s}^{-1}$ to $\omega(0.70) \approx 33 \text{ rad.s}^{-1}$. Experimentally the increase of $\omega(I)$ allows the system to resist a more important perturbation and still holds the upward position without diverging. It also shows that the system will come back faster to the centre. This is also controlled by the damping on the system. So, with the control parameter I it is possible to stabilize the natural unstable equilibrium of the inverted pendulum.

To have a proper evolution of the impact of the control parameter I on the system we repeat this study for multiple values of I and the corresponding values of $\omega(I)$ are presented in Fig 2.11. Indeed, it exists a critical value I_c of the electrical current for which the system is no longer diverging but it is now an oscillatory system (Fig 2.11). As presented in Fig 2.10.b-d, when $I > I_c$ we have an oscillatory response with an increasing $\omega(I)$. This is the domain we are interested to be able to stabilize the inverted pendulum. By modulating the negative curvature of the potential into a positive one periodically we could stabilize the system.

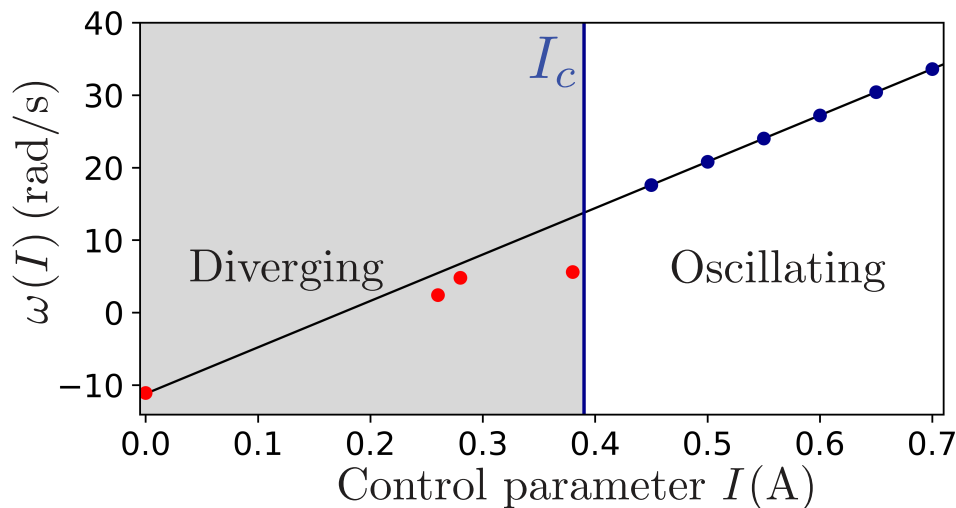


Figure 2.11: Characterization of the system as a function of the control parameter I . The scalar $\omega(I)$ characterize the local evolution function of the electromagnetic inverted pendulum. There is a specific value of the electrical current I_c where we change from a diverging system ($I < I_c$) to an oscillatory system ($I > I_c$).

3.2 Experimental stabilisation

Physical model

The electrical current I is the appropriate parameter to have a varying effective gravitational field on our system. To try to stabilize the experimental system we modulate the system in a square wave fashion (Fig 2.12.b). We can turn the electromagnets OFF (naturally divergent: $I = 0$) and ON (oscillatory $I > I_c$) during T_D and T_O respectively. The diverging system is now a periodically oscillatory-divergent system: the four parameters of the system are the natural time scale of the diverging state $-\omega(0)$, the frequency of the oscillatory state $\omega(I)$, T_O and T_D which are respectively the period for which the system is in the oscillatory state and in the diverging state (Fig 2.12.b).

Physically, the system can be interpreted in terms of the evolution of the potential energy. The potential energy of this periodic oscillatory-divergent system can be defined as $\mathcal{V}(\theta, t) = f(\theta)\mathcal{V}(t)$ where $f(\theta) = \cos(\theta)$ is a curvature function of the position θ and $\mathcal{V}(t)$ is a piecewise potential function of time, as presented in Fig 2.12.a and Fig 2.12.b respectively. We are focused on the evolution of the curvature and the period of the modulation, so we assume we have a system with a unitary inertia ($ml^2 = 1$).

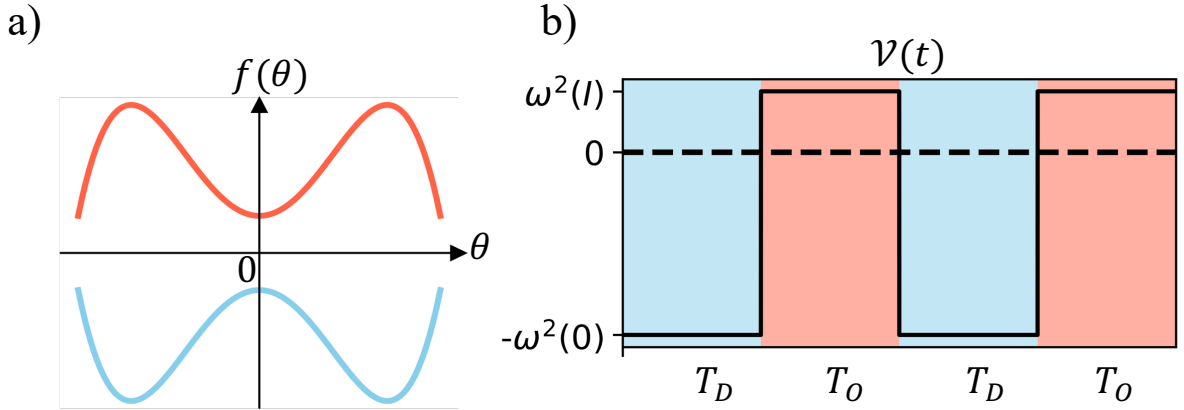


Figure 2.12: Potential energy of a periodically oscillating-diverging system defined by the function $\mathcal{V}(\theta, t) = f(\theta)\mathcal{V}(t)$ where $f(\theta) = \cos(\theta)$ is the curvature function of the position θ and $\mathcal{V}(t)$ is a square wave potential function of time. a) Curvature function $f(\theta) = \cos \theta$. Red line is the oscillatory state and blue line is the natural diverging state. b) Experimental T -periodic square wave modulation used to stabilize the electromagnetic inverted pendulum. The electromagnet is turned ON during T_O and the system is characterized by $\omega(I)^2$ (oscillatory state) and it is turned OFF during T_D characterized by the natural $-\omega(0)^2$ (natural divergent state). Blue background is used in all the figures to showcase the divergent state and red to showcase the oscillatory state.

The kinetic energy of the system is $\mathcal{T}(p) = \frac{1}{2}p^2$ with p the momentum. Having the kinetic energy and the potential energy we express the Hamiltonian of our system: $\mathcal{H}(\theta, \frac{d\theta}{dt}, t) =$

$\mathcal{T}(p) + \mathcal{V}(\theta, t)$. Using the Hamiltonian we deduce the Hamiltonian equations [94]:

$$\begin{cases} \frac{dp}{dt} = -\sin(\theta)\mathcal{V}(t), \\ \frac{d\theta}{dt} = p. \end{cases} \quad (2.7)$$

From the Hamiltonian equations (2.7) one can deduce the dynamical equations of the periodic oscillatory-diverging system. They read

$$\frac{d^2\theta(t)}{dt^2} + \mathcal{V}(t)\sin\theta(t) = 0 \quad \text{during } T \iff \begin{cases} \frac{d^2\theta(t)}{dt^2} - \omega(0)^2\sin\theta(t) = 0 & \text{during } T_D, \\ \frac{d^2\theta(t)}{dt^2} + \omega(I)^2\sin\theta(t) = 0 & \text{during } T_O, \end{cases} \quad (2.8)$$

where $\mathcal{V}(t)$ is the square wave modulation defined in Fig 2.12.b.

Finally, a first approach to stabilize the system is to study the linearised system. We approximate $\sin\theta(t)$ in Eq (2.8) near the equilibrium position, so the linear equation of motion of the electromagnetic inverted pendulum reads

$$\frac{d^2\theta(t)}{dt^2} + \mathcal{V}(t)\theta(t) = 0 \quad \text{during } T \iff \begin{cases} \frac{d^2\theta(t)}{dt^2} - \omega(0)^2\theta(t) = 0 & \text{during } T_D, \\ \frac{d^2\theta(t)}{dt^2} + \omega(I)^2\theta(t) = 0 & \text{during } T_O. \end{cases} \quad (2.9)$$

Experimental investigation to stabilize the inverted pendulum

To try to experimentally stabilize the system with a period of modulation closer to the natural time scale of the system we have to vary the value of the period of modulation $T = T_O + T_D$. The experimental protocol to explore this idea is the following: we fix a value of the electrical current I and the values of T_D and T_O will be varied. For a given set of parameters, we do a small perturbation to the system, and we observe if the inverted pendulum stays in the upward position. The different experimental observations are represented in Fig 2.13. If the system stays in the upward position the response is considered stable (blue squares in Fig 2.13) and if the system falls down the response is considered unstable (white squares in Fig 2.13). Finally, Eq (2.9) is a linear ordinary differential equation with a periodic coefficient, it is the Meissner equation [53, 77]. We can study the linear stability of the system using Floquet's theory [54]. We superpose the corresponding stability diagram to our experimental observations in Fig 2.13.

Figure 2.13 shows we can stabilize the inverted pendulum for multiple values of (T_O, T_D) . We also have an excellent agreement between the experimental results and the theoretical stability diagram: we have a good superposition of the experimental points with the corresponding stable or unstable region. We observe we were able to achieve the 5th stability region (blue regions). This is already an achievement knowing that in the previous setups they were limited to the first stability region (Fig 2.7). Then, we now the natural time scale of the system is $T_0 = 2\pi/\omega(0) \approx 0.57$ s. The maximum period of modulation we were capable to achieve to stabilize the system is for $T_D = 40\%T$ and $T_O = 0.1$ s, i.e the period of

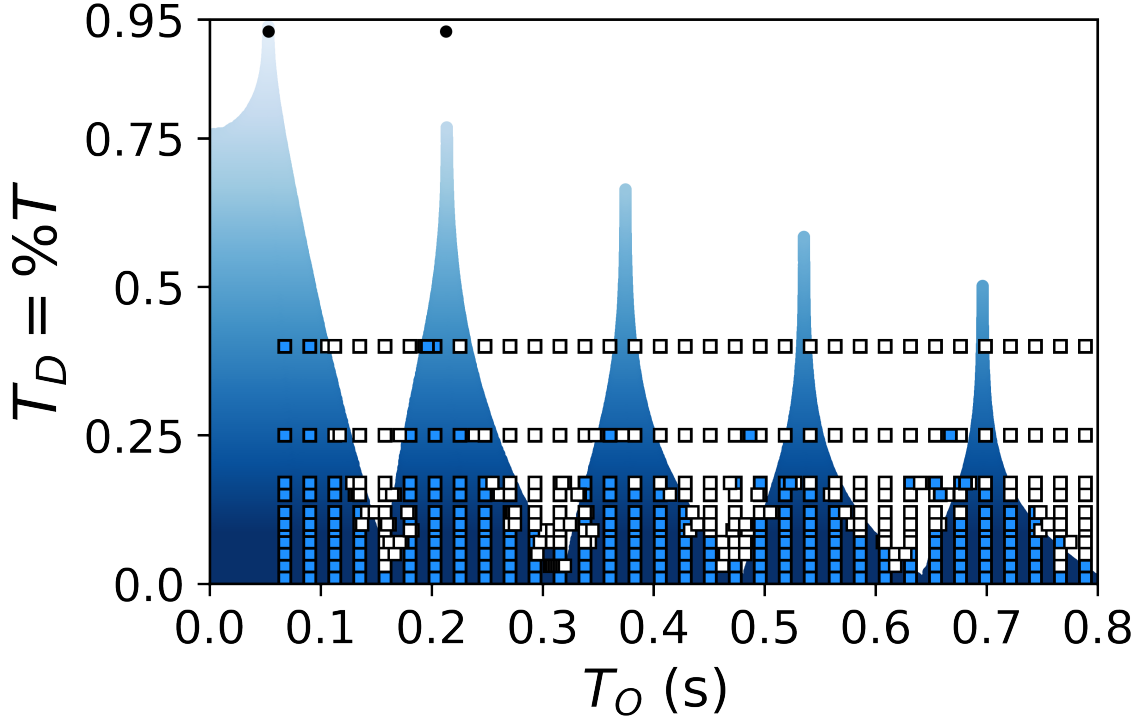


Figure 2.13: Experimental investigation to dynamical stabilize an inverted pendulum on the (T_O, T_D) space with the electrical current fixed at $I = 0.48$ A. Blue squares are the experimental stable responses and white squares are the experimental unstable responses. We superpose the stability diagram where the stability regions are in blue, and the instability regions are in white. Black dots used for the numerical simulations at $T_D = 95\%T$: First stability tongue: $T_O \approx 0.053$ s. Second stability tongue: $T_O \approx 0.213$ s

modulation is $T = 0.17$ s. We have a modulation with the same order of magnitude than the natural frequency of the system. As comparison, in the experiment conducted by Smith [66], the natural time scale of their system is $T_{smith} \approx 0.18$ s and the period of modulation is $T = 6.4 \times 10^{-3}$ s (Table 2.1) they do have a much faster modulation compared to the natural time scale of their system. This shows that we have achieved dynamical stabilization without using the Kapitza approach. To keep going further away from the Kapitza limit, we should try to be the closest possible to the tip of the stability regions. The periods of modulations will be larger, and we can continue to study this new approach for stabilization.

As we get closer to the tip of the stability region, the value of T_D is closer to the value of the period of modulation T and T_O is closer to impulses as presented in Fig 2.14. This is physically interesting because the electrical energy used during a period to stabilize the system is defined as $E_{elec} = RI^2T_O$ with R the resistance of the generator. So, when we are closer to the tip of the stability region, T_O decreases so the electrical energy spend E_{elec} decreases too. Physically this means we are spending more time in the natural diverging state (T_D takes more “place” in the period T) and at precise periods T_O we send an impulse of energy E_{elec} to change to the oscillatory state and periodically stabilize the system. For example, if we had stabilized the inverted pendulum during one hour with a continuous

signal (first case in Fig 2.14) we would have spent $E_{elec0} = 5.35$ W.h. Now if we do it with our best case $T_D = 40\%T$, the energy spent will be $E_{elec} = 60\%E_{elec0} = 3.2$ W.h.

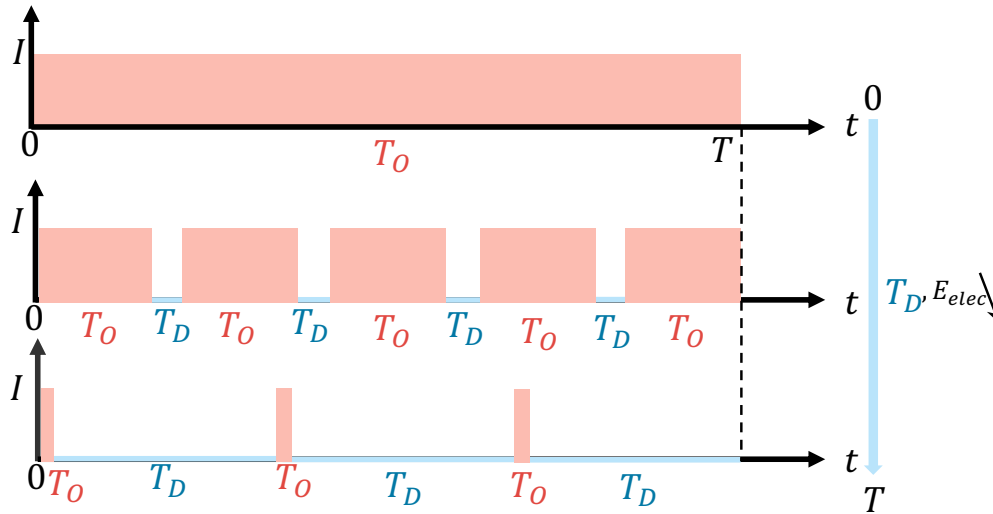


Figure 2.14: Schematic representation of the evolution of the shape of the square modulation function. To decrease the value of E_{elec} and still be stable the period T_D should take more “place” in the period T than T_O .

4 Numerical study of the tip of the stability regions

Dynamical stabilization using a period of modulation close to the natural time scale of the system is not only possible (Fig 2.13) but it can even be more energetically advantageous (Fig 2.14). However, access them with the current approach is difficult and experimentally challenging, the stability regions are thinner close to the tip. Our goal is to analyse the numerical responses in this particular region and try to deduce some characteristics helping us to reach them in an easier way.

4.1 Basin of attraction

The linear analysis is necessary but not sufficient to know whether the true system will be stable. We need to know what size of imperfection or perturbation is acceptable (basin of attraction). To have this information we need to study the attractor of the nonlinear system at the tip of the stability region. So, we use Eq (2.8) to perform this numerical study.

For this numerical study at the tip of the stability region we fix a point at $T_D = 95\%T$, $T_O = 0.053$ s. It is represented by a black dot in the stability diagram in Fig 2.13 and Fig 2.15a), showing how near the tip the region gets thinner and thinner. To deduce the basin of attraction we analyse the response for multiple initial conditions $((d\theta/d\tau)|_0, \theta_0)$. The criteria to define if a couple of initial conditions returns to a stable response is if the absolute value of the response is smaller than two times the initial condition θ_0 (blue dots in Fig 2.15.b). If the numerical response is over this limit the response is considered unstable (grey dots in Fig 2.15.b) and each response is calculated for one hundred periods.

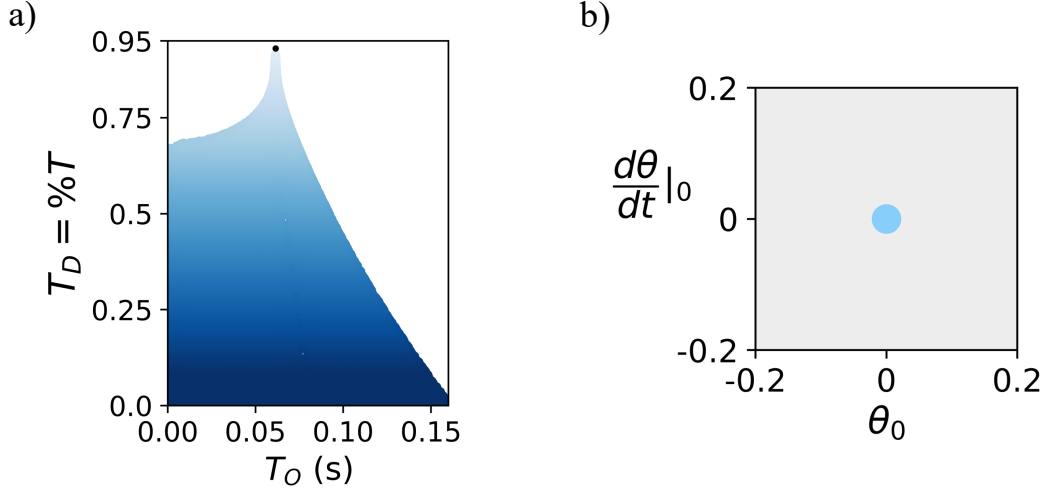


Figure 2.15: Study of the tip of the first stability region. a) Linear stability diagram of the first stability region showed in blue. Black dot is the point near the tip of the stability region we use for our numerical study ($T_O = 0.053$ s, $T_D = 95\%T$). b) Shape of the basin of attraction at the tip of the stability region. Blue region shows the stable initial conditions.

Figure 2.15.b shows that at the tip of the stability region the basin of attraction is small and centred at the $(0, 0)$ point. This means that to be stable at the tip of the stability region the system cannot resist large initial conditions. This agrees with the fact that at the tip of the stability region we are a longer amount of time, during the period T , in the natural diverging state (unstable) and only a small time in the oscillatory state (stable). So, any strong perturbation will make the inverted pendulum to fall from the upward position (diverge). This physical behaviour is characteristic of being close to the tip of the stability region, and independent of the choice of the stability region. So, we can assume that this basin of attraction is the same for the others stability regions near the tip. Now that we know which initial conditions are acceptable to have a stable response, we can analyze the numerical nonlinear responses.

4.2 Study of the responses

We study the evolution of the nonlinear response near the tip of the first stability tongue using the nonlinear equation described with Eq (2.8) and we use the parameters defining the black point in Fig 2.15.a ($T_O = 0.053$ s, $T_D = 95\%T$). The initial conditions are chosen randomly from the basin of attraction in Fig 2.15.b. We run one hundred periods of the response and we present the first twenty-five periods in Fig 2.16.

First of all we observe a stable response. Then, by introducing black dotted horizontal lines at each $t = nT + T_D/2$, with n the number of the period, we observe that between two consecutive black dotted lines the response can always be decomposed in three parts: an exponential diverging motion, followed by exactly one oscillation during T_O and finally an exponential convergent motion towards the x -axis. Let's denominate the domain between two consecutive black dotted lines a unit cell. Between two consecutive unit cells the local maximum does not have the same value. This maximum is noted ρ_n . By colouring coding each maximum inside the unit cells (chronologically ordered from white to black) and connecting them by an interpolation, we observe that the evolution of ρ_n follows a harmonic

evolution over time (Fig 2.16.b). Finally, for the same set of parameters we observe the corresponding linear response defined by Eq (2.9) and it is superposed with a dashed white line to the nonlinear response in Fig 2.16.a. We observe that the linear response perfectly describes the evolution of the nonlinear response near the tip of the stability region.

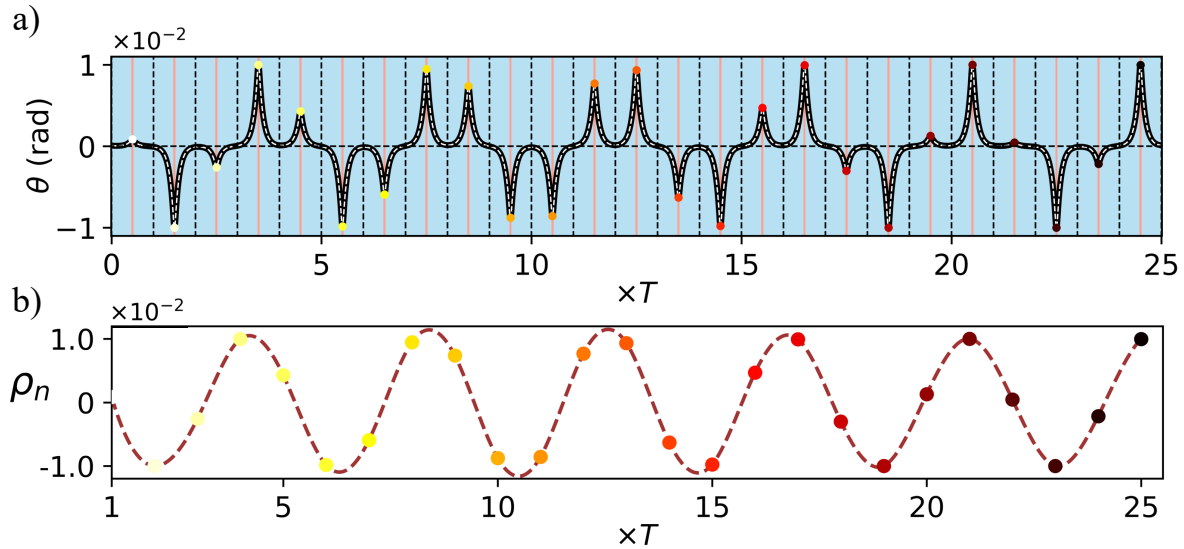


Figure 2.16: Numerical nonlinear response for the first stability region for $(\omega(0), I = 0.48 \text{ A}, T_O = 0.053 \text{ s}, T_D = 95\%T)$, black dot in Fig 2.13). a) Black line represents the nonlinear system. Black dotted lines represent the boundaries of a unit cell defined at $t = nT + T_D/2$, with $n \in \mathbb{N}$. Coloured points are the maximum of the response at each unit cell (chronologically ordered from white to black). White dashed line is the linear response for the same set of parameters. b) Evolution of the maximum amplitude ρ_n at each unit cell. Red dashed line is an interpolation of ρ_n showing a harmonic motion.

So, the complete nonlinear response near the tip of the stability region can be interpreted as a particular mode in a unit cell with different amplitudes ρ_n . Fig 2.17.a shows the first 25 periods of the response in the corresponding unit $-T_D/2$ to $T_D/2$. The coloured lines correspond to the given period T chronologically ordered from white to black and following the same colours as in Fig 2.16). Then, Fig 2.17.b shows the 25 first periods of the nonlinear response near the tip of the second stability region (black dot in Fig 2.13: $T_O = 0.213 \text{ s}, T_D = 95\%T$). We observe that the response during the different periods has the same shape but not the same amplitude, the response does two oscillations during T_O .

Lastly, we have seen that the nonlinear response can be perfectly described with the response of the corresponding linear model (Fig 2.16) and Fig 2.17 shows that each stability region has a particular mode. To validate it, now that we have a linear model, we can take the linear response of Fig 2.16 (which is exactly the nonlinear response) and multiply it by the given ρ_n in Fig 2.16 b) to scale the response at each period and collapse them in the unit cell (Figure 2.18). Indeed, Fig 2.18 shows that we do have a particular mode at the tip of each stability region. At the boundaries of the unit cell the response tends towards zero, but it is not exactly zero due to the periodicity of the response.

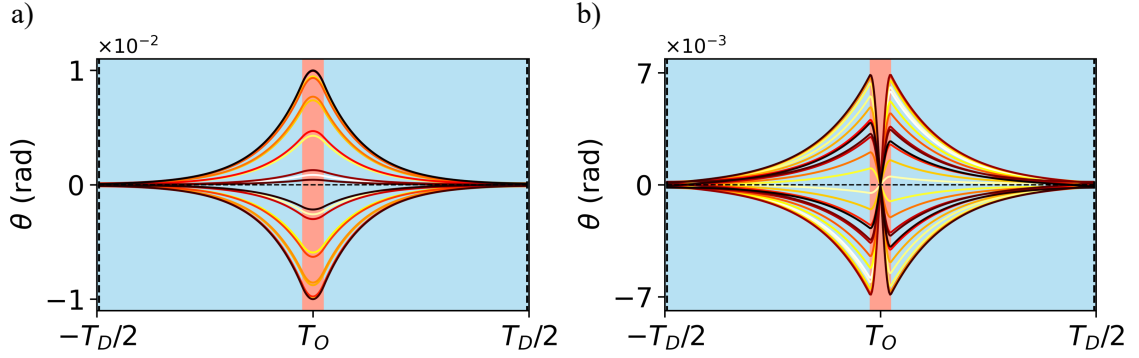


Figure 2.17: First 25 periods chronologically ordered from white to black of the nonlinear response near the tip of the stability region in a unit cell. a) First stability region characterized with one oscillation during T_O . b) Second stability region characterized with two oscillations during T_O . The parameters are the ones of the black dots in Fig 2.13.

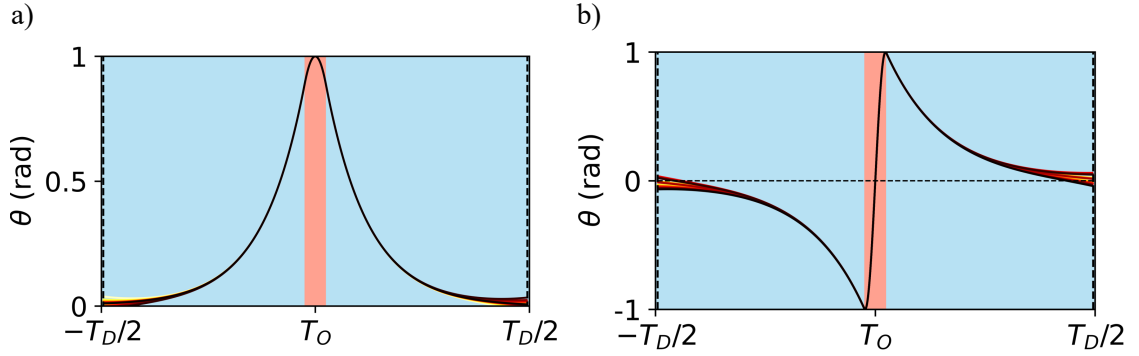


Figure 2.18: First 25 periods chronologically ordered from white to black of the nonlinear response near the tip of the stability region multiplied by the given ρ_n at each period defined in the unit cell. a) Collapse of the response of the first stability region characterized with one oscillation during T_O . b) Collapse of the response of the second stability region characterized with two oscillations during T_O . The parameters are the ones of the black dots in Fig 2.13.

4.3 Resolution in a unit cell

The previous numerical observations, conducted for the electromagnetic inverted pendulum, showed that close to the tip of the stability diagram the motion of the nonlinear periodic oscillatory-diverging system can be described by a linear combination of a particular mode in a unit cell periodically multiplied by a constant (Fig 2.18). This means, the system can be reduced to the study of the motion in the unit cell which is defined with the four parameters of the system (Fig 2.19). Moreover, the collapsing of the responses in Fig 2.18 shows at each period the response tends to 0 at the boundaries of a unit cell defined in Fig 2.19. Finally, the study of the basin of attraction in Fig 2.15.b shows that to have a stable response the perturbation needs to be small and close to the $(0, 0)$ point in the phase space. Taking in consideration these observations, we propose that the initial value problem (IVP) governing the motion of the system can be approach as a linear boundary value problem (BVP) on a unit cell (Fig 2.19). The corresponding boundary value problem reads

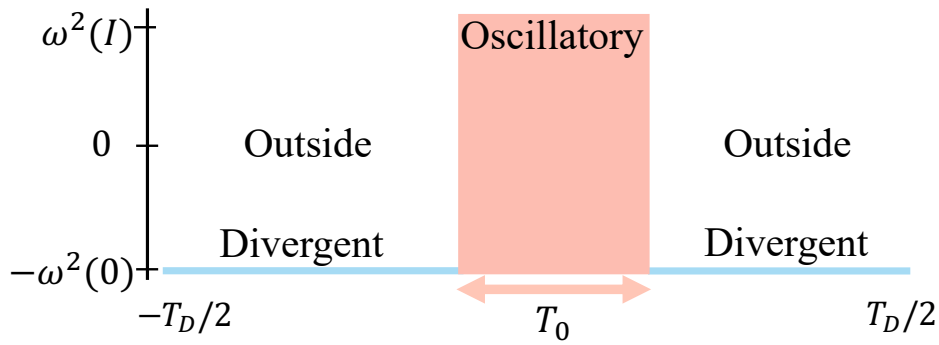


Figure 2.19: The study of the nonlinear response of the dynamical system near the tip of the stability region is approached to a boundary value problem in this unit cell defined between $-T_D/2$ and $T_D/2$.

$$\begin{cases} \frac{d^2\theta(t)}{dt^2} - \omega(0)^2\theta(t) = 0 & \text{for } t \in \text{Outside}, \\ \frac{d^2\theta(t)}{dt^2} + \omega(I)^2\theta(t) = 0 & \text{for } t \in [-T_O/2, T_O/2], \\ \theta(-T_D/2) = \theta(T_D/2) = 0, \end{cases} \quad (2.10)$$

with $\text{Outside} = [-T_D/2, -T_O/2] \cup [T_O/2, T_D/2]$.

To validate our approximation, we numerically solve Eq (2.10) using the parameters of Fig 2.18 (black dots in Fig 2.13). We superpose the nonlinear IVP response collapsed into the unit cell with the BVP solutions in Fig 2.20.

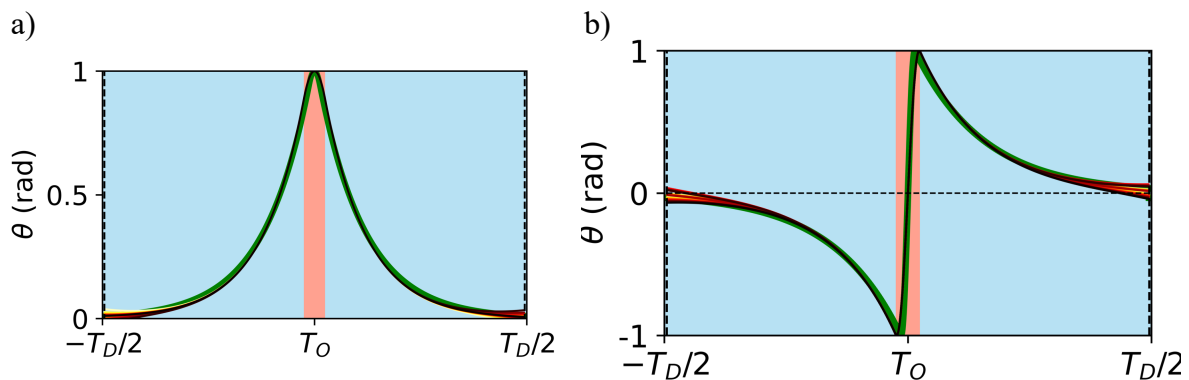


Figure 2.20: First 25 periods of IVP defined with Eq (2.8) (chronologically ordered from white to black) superposed to the solution of the BVP defined with Eq (2.10) in green calculated with the same parameters (black dots in Fig 2.13). a) First stability region near the tip ($T_O = 0.053$ s, $T_D = 95\%T$). b) Second stability region near the tip ($T_O = 0.213$ s, $T_D = 95\%T$)

Figure 2.20 shows a perfect agreement between the solution of the BVP (in green) and the nonlinear IVP in the unit cell (coloured lines). So, near the tip of the stability regions the characteristic mode defining the IVP can be deduced solving the BVP defined in Eq (2.10).

Thus, the parameters to stabilize a system near the tip of the stability tongues can be inferred with the solution of a boundary value problem. In this case it will be finding the correct values of T_O to stabilize the system at a fixed electrical current I and T_D the closest possible to the period of modulation T .

5 Pseudo-analytical solutions at the tip of the stability tongue

5.1 Analog problem

Near the tip of the stability region, we showed that the nonlinear IVP can be approximated with a linear BVP defined by Eq (2.10) (Fig 2.19). For all the stability regions, in the unit cell the response can be decomposed in the following three parts: an exponential diverging motion in $[-T_D/2, -T_O/2]$ defined by $\omega(0)^2$, followed by exactly m oscillations during T_O (with m the number of the stability region) defined by $\omega(I)^2$, and finally an exponential convergent motion towards the x -axis during $[T_O/2, T_D/2]$ defined by $-\omega(0)^2$. Interpreted in this manner, the BVP defined in Eq (2.10) has the same physical behaviour of another well-known physical problem: the problem of finding the quantised energy levels of a particle trapped under a square finite potential well [95, 96, 97]. We are interested in this problem because it is an eigenvalue problem where the eigenvalues and eigenfunctions have a pseudo-analytical solution [95, 98, 97]. The physical parameters of this problem are presented in Fig 2.21, where the motion of the particle can be decomposed in the same three parts as before (divergence, oscillation, divergence) and the motion of the particle is defined by the dimensionless time-independent Schrödinger equation that reads [95, 97]

$$\begin{cases} \frac{d^2\psi}{d\chi^2} - (u^2 - v^2)\psi(\chi) = 0 & \text{for } \chi \in \text{Outside}, \\ \frac{d^2\psi}{d\chi^2} + v^2\psi(\chi) = 0 & \text{for } \chi \in L, \\ \psi(-\infty) = \psi(\infty) = 0, \end{cases} \quad (2.11)$$

with $\text{Outside} = [-\infty, -L/2] \cup [L/2, \infty]$, $\chi = 2\pi/L$, $u = \sqrt{2mV_0}L/2\hbar$ and $v = \sqrt{2mE}L/2\hbar$.

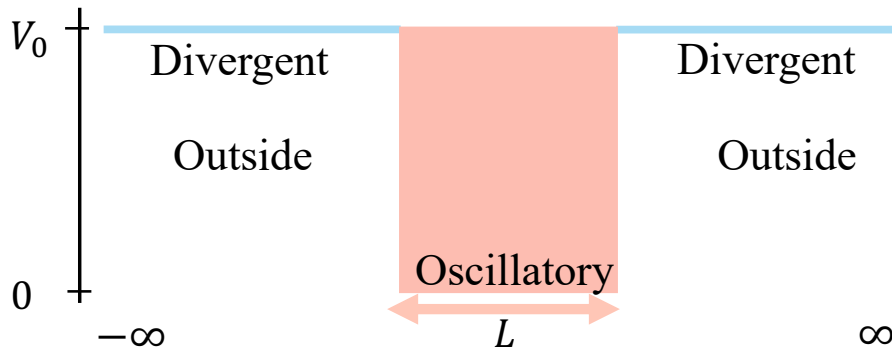


Figure 2.21: Schematic representation of the problem of a particle in a finite potential well. For a giving potential V_0 and box of length L we search the quantized energies levels E .

We need to rewrite our BVP defined in Eq (2.10) to be in the same form as the dimensionless equation of the analog problem (Eq (2.11)) to use its pseudo-analytical solutions. To do so firstly we observe that in Eq (2.11) there is only one time scale: the size of the box. To take this in consideration in our system we assume that the boundaries of the BVP are also $\pm\infty$. Thus, $T_D \rightarrow \pm\infty$. This is an important consideration because we are reducing our number of unknowns by one, we only have $(\omega(0), \omega(I), T_O)$, and physically it means we are eliminating a time scale. Secondly, we introduce the dimensionless parameter $\tau = \omega t$ into the BVP of Eq (2.10), with $\omega = 2\pi/T$ and T the period of modulation.

Finally, we observe that the shape of the unit cell defined in Fig 2.19 is not the same as the one we should have (Fig 2.21). Comparing both unit cells, we observe that at the *Outside* domain (in Fig 2.19) our system is at $-\omega(0)^2$, meaning we cross the 0 value, whereas the particle in the finite potential well does not cross the 0 value and the potential is in fact at its maximum value (Fig 2.21). Moreover, at the oscillatory state, we should be at the minimum value of the potential but instead we are at the maximum value for our case. Identifying these differences, we introduce the variable $\Delta\Omega^2 = |\omega^2(I) + \omega^2(0)|/\omega^2$ to modify our current potential and we propose a new potential $\mathcal{U}(\tau)$ represented in Fig 2.22 and defined as

$$\mathcal{U}(\tau) = -\mathcal{V}(\tau) + \omega(I)^2, \quad (2.12)$$

to have the same evolution as the analog potential in Fig 2.21.

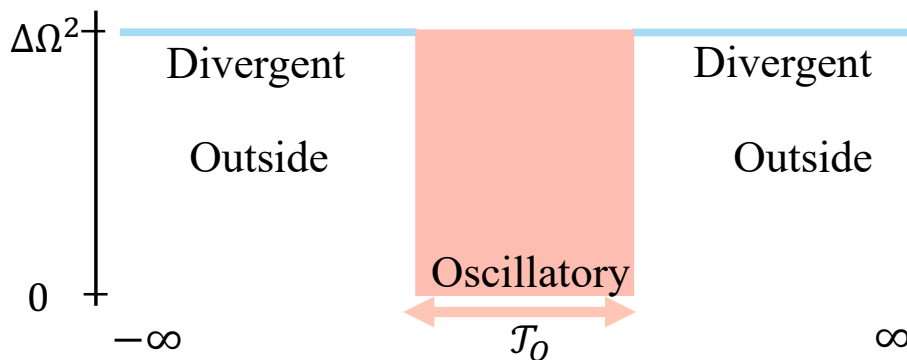


Figure 2.22: Expression of the potential $\mathcal{U}(\tau)$ at the tip of the stability region to deduce the stability parameters with a pseudo analytical relation.

Introducing the new potential $\mathcal{U}(\tau)$ (Fig 2.22) and the different observations we previously made into Eq (2.10), the new BVP reads

$$\begin{cases} \frac{d^2\theta(\tau)}{d\tau^2} - (\Delta\Omega^2 - \omega^2(I)/\omega^2)\theta(\tau) = 0 & \text{for } \tau \in \text{Outside}, \\ \frac{d^2\theta(\tau)}{d\tau^2} + (\omega^2(I)/\omega^2)\theta(\tau) = 0 & \text{for } \tau \in \mathcal{T}_O = 2\pi T_0/T, \\ \theta(-\infty) = \theta(\infty) = 0, \end{cases} \quad (2.13)$$

with $\text{Outside} = [-\infty, -\mathcal{T}_O/2] \cup [\mathcal{T}_O/2, \infty]$.

The expression of the BVP in Eq (2.13) is the same as the analog problem of Eq (2.11)

The general pseudo analytical solutions for this type of problem are [95, 98]:

$$\sqrt{\gamma_0^2 - \eta^2} = \begin{cases} \eta \tan(\eta) & \text{symmetric case,} \\ -\eta \cot(\eta) & \text{anti-symmetric case,} \end{cases} \quad (2.14)$$

where for a fixed γ_0 , the pseudo-analytical solutions η_m are the intersections between this demi-circle and these trigonometric functions. We can express these dimensionless parameters as a function of our parameters:

$$\gamma_0 = \sqrt{\omega^2(0) + \omega^2(I)T_O/2}, \quad \eta = \omega(I)T_O/2, \quad (2.15)$$

where the eigenvalue η will give the value of the period T_O needed to stabilize the system for a giving electrical current I and the corresponding eigenfunction should give the proper mode. To test if the approximation is valid, we search for the value of T_O using the same parameters we used for the stability chart in Fig 2.13 ($I = 0.48\text{A}$ and $\omega(0) \approx 11 \text{ rad.s}^{-1}$) which correspond to the parameters of the numerical simulations for the IVP of Eq (2.8) and the previous BVP of Eq (2.10), so the eigenfunction should be the same as the mode found in Fig 2.20.

We calculate the two first eigenfunctions and the eigenvalues solution of Eq (2.13), i.e we solve the two first intersections of the curves in Eq (2.14) for this set of parameters. With the two eigenvalues η_m we deduce that for the first stability region the value of T_O to stabilize the system is $T_O = 0.053014\text{s}$ and for the second stability region it is $T_O = 0.213873\text{s}$. Which are in perfect agreement with the x -coordinate of the two black points in the tip of the stability chart in Fig 2.13. The corresponding pseudo-analytical eigenfunctions are presented in Fig 2.23. They are the same solutions obtained with the BVP of Eq (2.10) showed in Fig 2.20 only this time the resolution is pseudo-analytical, and we can deduce the parameter T_O to stabilize the system.

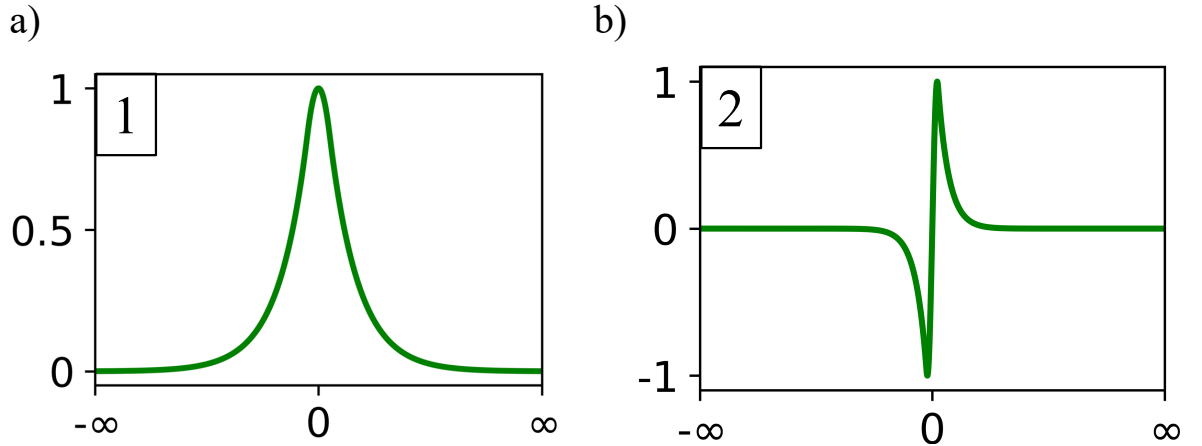


Figure 2.23: Pseudo-analytical eigenfunctions found with Eq (2.14) for $I = 0.48\text{A}$ and $\omega(0) \approx 11 \text{ rad.s}^{-1}$. a) Eigenfunction for the first intersection of Eq (2.14) with a corresponding eigenvalue $\eta_1 = 0.517683$ and we can infer $T_O = 0.053014 \text{ s}$. b) Eigenfunction for the second intersection of Eq (2.14) with a corresponding eigenvalue $\eta_2 = 2.088479$ and we can infer $T_O = 0.213873 \text{ s}$.

With this approach, the actual position of the system is not predicted by Eq (2.13). However it can be deduced from a successive repetition of the pseudo-analytical eigenfunction

(Fig 2.23) periodically scaled by the value of ρ_n in Fig 2.16.b. In Fig 2.24, we superpose the nonlinear response of Fig 2.16.a with the corresponding pseudo-analytical eigenfunctions multiplied by ρ_n and the boundaries of the eigenfunction in Fig 2.23 are scaled to match the boundaries of the unit cell defined as $\mathcal{T}_D = 95\%2\pi$. We have a perfect agreement between the nonlinear response and the scaled pseudo analytical mode.

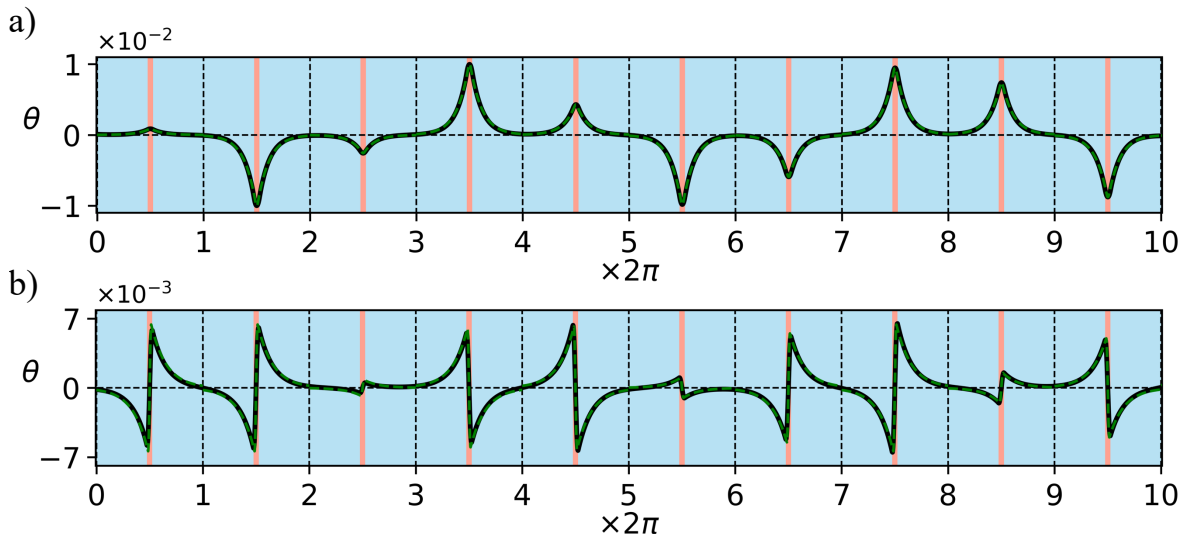


Figure 2.24: Comparison of the numerical nonlinear responses for the first two stability zones at $\mathcal{T}_D = 95\%2\pi$ in black lines (parameters used are the black dots in Fig 2.13) with the scaled pseudo-analytical eigenfunctions solution of Eq (2.14) in dashed green line.

These two numerical examples validate the pseudo-analytical solutions of Eq (2.13) as a new method to deduce the value of the period T_O to stabilize an unstable system near the tip of the stability regions and we infer the shape of the response with the eigenfunction.

5.2 Pseudo-analytical solutions near the tip of the stability tongue

Previously, we solved the pseudo-analytical equation Eq (2.14) for one value of γ_0 coming from the experimental values. Now we solve Eq (2.14) for multiple γ_0 and plot them as functions of the eigenvalues η_m . Thus, we have a direct access to the eigenvalues of Eq (2.14) to stabilize a natural unstable equilibrium. The first four curves are represented in Fig 2.25. For our stabilization problem, the red curves in Fig 2.25 correspond to the value of T_O we need to use to stabilize the inverted pendulum ($\omega(0)$ fixed) for a giving electrical current I . We can use these master curves to deduce the complete set of parameters to dynamical stabilize any natural unstable system near the tip of the stability region using a periodic square wave modulation.

For each value in the master curves presented in Fig 2.25 we have a corresponding eigenfunction. For each m -master curve the eigenfunction have the same shape, for example Fig 2.23 shows the modes for the first two intersections master curves.

We demonstrated that it exists a pseudo-analytical solution, Eq (2.14), to deduce the value of the parameters to stabilize a natural unstable equilibrium near the tip of the stability

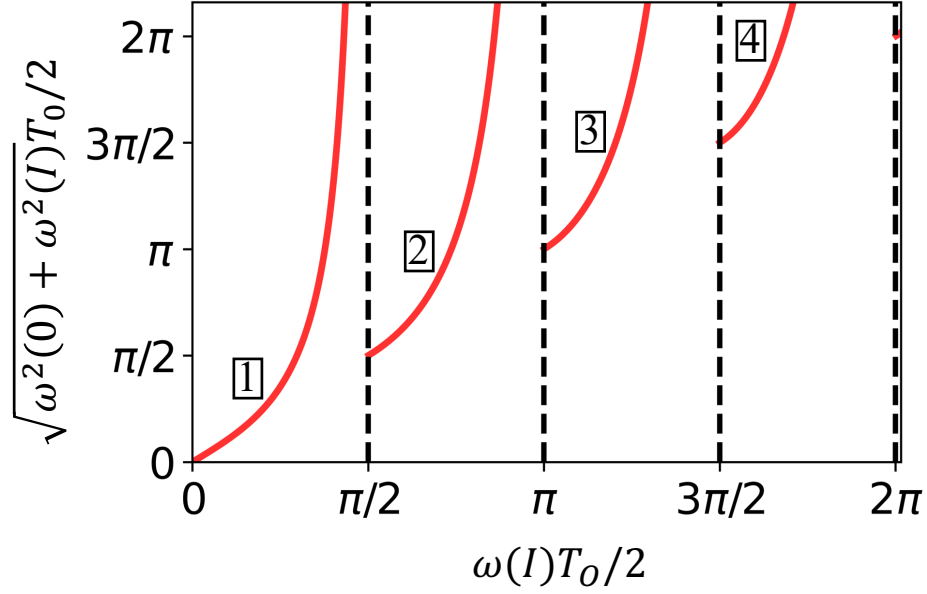


Figure 2.25: First four pseudo-analytical solutions in the (γ_0, η_m) space. Red curves are the master curves for every m -mode of the m^{th} stability region. Dotted black lines represent the solutions for the infinite potential.

regions (in our case the value of T_O). Then with the eigenfunctions of these master curves (Fig 2.25) we can have the qualitative behavior of the response which only depends on the choice of the master curve.

5.3 Re-introducing the second time scale to the master curves

To obtain these master curves (Fig 2.25), we started from the hypothesis that at the tip of the stability region the IVP can be studied as a BVP in a unit cell where the boundaries are defined at $\pm\infty$. By doing this approximation we reduced our problem from four variables to three variables. We re-introduce the time scale T_D because in a real setup we can stabilize the system far from the tip (Fig 2.13). Fig 2.26 shows that at a fixed value of T_D the stability region has a width. Because the master curves are calculated near the tip, the width is practically inexistent. However, if we get away from this limit, the width of the regions grows larger. For example, if $T_D = 25\%T$, Fig 2.13 shows that the size of this width is more important compared to the one for $T_D = 75\%T$ (green dotted lines in Fig 2.26). This width can be important experimentally because being at lower value of T_D means we have a larger width of values T_O to stabilize the system. So, we want to observe if the master curves are still good indicators far the tip of the stability region.

To analyse the impact of T_D in the master curves, we fix its value to two different percentages. For example $T_D = 25\%T$ and $T_D = 70\%T$, that way we have two very different widths. We translate the widths (green dotted lines in Fig 2.26) of the stability diagram into the dimensionless space (γ_0, η) . The pseudo-analytical master curves with the corresponding widths are represented in Fig 2.27.

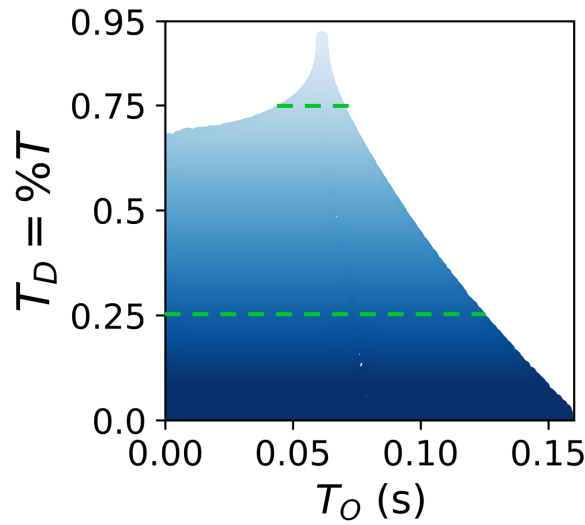


Figure 2.26: Stability diagram of the Meissner equation showcasing the first stability tongue. Two dashed green lines at $T_D = 25\%T$ and $T_D = 75\%T$ show how the width of the stability region decreases as we get closer to the tip of the stability region.

Fig 2.27.a shows a thinner colored region than Fig 2.27.b which is expected because the percentage of T_D is larger. Secondly, we observe that no matter the percentage used, the red pseudo-analytical master curves are always at the middle of the stability regions. This shows that the master curves can be used to dynamical stabilize a system for any value of T_D , not only at the tip of the stability region.

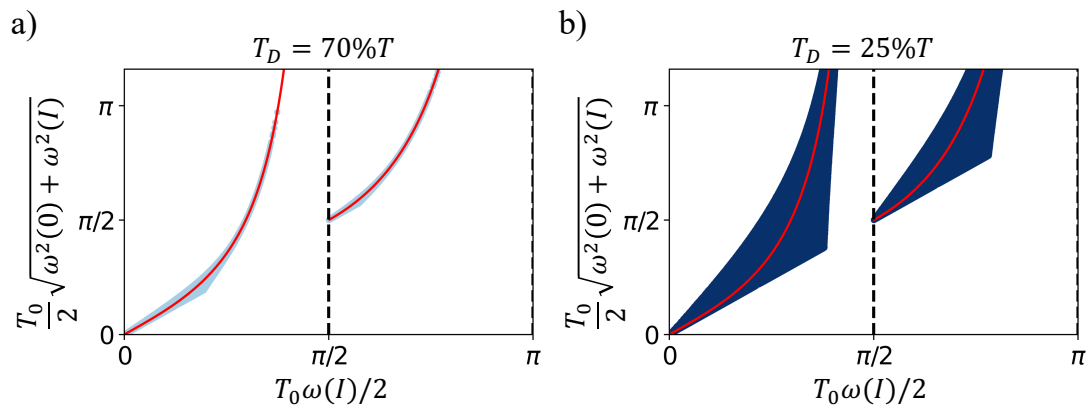


Figure 2.27: First two master curves solution of Eq (2.14) in the (γ_0, η) space with the evolution of the width of the stability region for two different values of T_D . For both cases the red curves are at the middle of the regions. a) $T_D = 70\%T$ has a more restricted area converging to the red curves showing that the stabilization can be done for values of (γ_0, η) closer to the master curves. b) $T_D = 25\%2\pi$ shows a wider region (dark blue) allowing more values of (γ_0, η) to have a stable solution.

So, the master curves defined in Eq (2.14) let us navigate all the stability tongues in a simpler way. With these approach, instead of having a continuously diagram, we have a discrete number of pseudo-analytical curves to deduce the parameters to stabilize a system

for any value of T_D . They can be a new powerful tool to explore dynamic stabilization with frequencies of modulations closer to the natural time scale of the system, giving an alternative to the Kapitza approach.

6 Experimental validation of the master curves: synchronized dynamical stabilization

We want to observe if the theoretical master curves defined in Eq (2.14) and presented in Fig 2.27 can be used to dynamical stabilize a macroscopic system. To do so we use our periodically oscillatory-divergent experimental system: the electromagnetic inverted pendulum presented in Fig 2.8 and defined by the linear model

$$\begin{aligned} \frac{d^2\theta(t)}{dt^2} - \omega^2(0) \sin \theta(t) &= 0 \quad \text{during } T_D, \\ \frac{d^2\theta(t)}{dt^2} + \omega^2(I) \sin \theta(t) &= 0 \quad \text{during } T_O. \end{aligned} \quad (2.16)$$

Without the master curves, the largest value of T_D we achieved was $T_D = 40\%T$ and we had a period of modulation of the same order of magnitude as the natural time scale of the system. This is already an achievement, however with the master curves we hope to achieve higher percentages.

During the numerical analysis we defined the dimensionless parameters (γ_0, η) as function of our experimental parameters $(\omega(I), \omega(0)$ and $T_O)$ (Eq (2.15)). The relation is :

$$\gamma_0 = \frac{T_O}{2} \sqrt{(\omega(0)^2 + \omega(I)^2)}, \quad \eta = \frac{T_O}{2} \omega(I). \quad (2.17)$$

The experimental protocol to validate the master curves is the following: we fix the value of T_D to a given percentage of the experimental period T . By doing so we can use Fig 2.27 to have the master curves with the corresponding width of the stability for this percentage of T_D . Finally, we fix the value of the electrical current I . Having a fixed framework, we can select a couple (γ_0, η) belonging to the master curves or to the coloured stability region. Having this couple, we use Eq (2.17) to deduce the value of the period T_O to have an experimental stable response (the value of $\omega(0)$ is fixed with the geometry of the system). Once the value of T_O is deduced, the value of T_D is calculated according to the selected percentage we wanted it to have in the modulation period T .

With the characterization of the system presented in Fig 2.11, we know that the minimum electrical current to stabilize the system is $I = 0.39A$. Also due to the specification of our electromagnet, the maximum voltage to avoid damages is 12V. So, we know that the maximum electrical current we should use for long recordings of a response is $I = 0.55A$. This provides us with a maximum and a minimum electrical current. For the recording of the motion of the marble, our system has a natural diverging time equal to $T_0 = 2\pi/\omega_0 \approx 0.57s$, so we use 150 frames per second i.e one image every 0.007 s to capture it. The post processing is the same one we previously used. Finally, to assure the system is stable, each experimental response is recorded during one minute, so we will record at least 200 periods for each experimental response, which we consider sufficient to confirm the stabilization of the system.

6.1 Experimental stabilization at $T_D = 25\%T$

The goal is to stabilize the system for the largest possible value of T_D because we will be able to have a frequency of modulations closer to the time scale of the system and explore a stabilization approach different from the one presented by Kapitza.

Before doing a high percentage of T_D in the period T , we want to validate the master curves of Eq (2.14) for a relatively small percentage. With a small percentage, there is a wider value of T_O to stabilize the system (Fig 2.27). We choose to have $T_D = 25\%T$. Then, we choose to work with the minimum possible value of I , but still having an oscillatory system during T_O . In our case we fix $I = 0.40A$. Finally we use the master curves in Fig 2.27.b and take multiple values of (γ_0, η) and deduce the corresponding period T_O . The experimental results for multiple (γ_0, η) are presented in Fig 2.28.

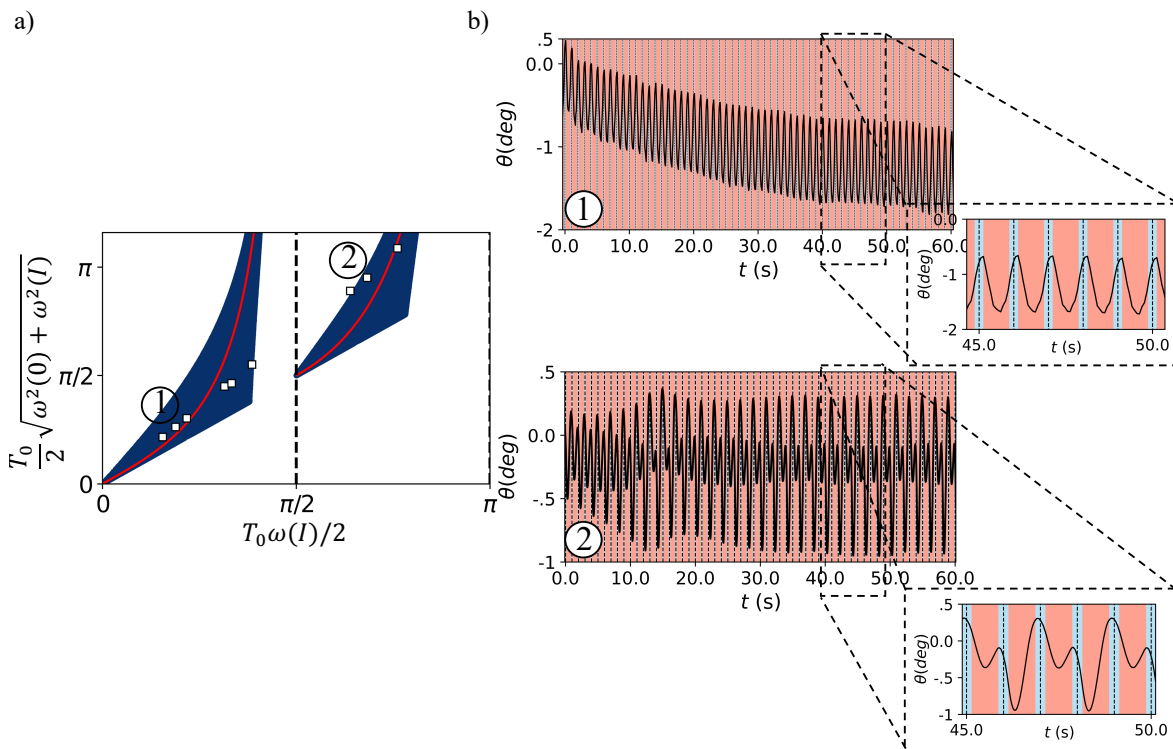


Figure 2.28: Experimental validation of the use of the master curves to stabilize a system for $T_D = 25\%T$. a) First two master curves with the corresponding width of the stability region in dark blue. White squares represent the experimental stable points. b) Two experimental responses enumerated 1 and 2 in the diagram. Point 1 is in the first stability region and the experimental parameters are $I = 0.40 A$, $T_O = 105$ ms and $T_D = 35$ ms. In the inset we observe the response has the shape of the mode 1. Point 2 is in the second stability region and the experimental parameters are $I = 0.40A$, $T_O = 309$ ms and $T_D = 155$ ms. The inset shows the response has the shape of the mode 2.

White squares in Fig 2.28.a demonstrate that we can stabilize a naturally unstable system using the theoretical master curves. We also observe that the (γ_0, η) chosen in the blue stability region give us a stable solution (Fig 2.28.a). We have obtained a general dimension-

less space to study the stabilization of a dynamical system. Furthermore, the experimental responses (Fig 2.28.b) show that when we are in the first or second stability region the shape of the response changes. As we can see in the top zoom of Fig 2.28.b the point 1 the stable response during the oscillatory state (pale red background) does one oscillation, characteristic of the mode appearing at the first stability region (see Fig 2.20.a). In the bottom zoom, the response numbered 2 which is placed in the second stability region does two oscillations during the oscillatory state (pale red background), characteristic of the mode appearing in the second stability region (see Fig 2.20.b).

These multiple experimental points prove that our theoretical study for deducing the parameters to stabilize an initial value problem with a boundary value problem in a unit cell (Eq (2.14)) is valid. Also, we can use it to experimentally explore beyond the first stability region (Fig 2.28). Finally for the top experimental response in Fig 2.28.b the period of modulation is $T = 0.14\text{s}$ and for the bottom experimental response in Fig 2.28.b the period of modulation is $T = 0.47\text{s}$. The natural period of the system is $T_0 = 0.57\text{s}$. So, we observe that for both experimental results we are modulating close to the natural time scale of the inverted pendulum, we are no longer on the Kapitza approach. We can stabilize a natural unstable system exploring a new approach. We are conducting a synchronized dynamic stabilization.

6.2 Experimental stabilization at $T_D = 70\%T$

We now choose $T_D = 70\%T$. A larger percentage means the width of the stability region is going to be smaller and the values of (γ_0, η) will be limited and closer to the red master curves (Fig 2.27.a). This means that it will be more difficult to stabilize the experimental system. Most of the the values of (γ_0, η) with $I \approx 0.40$ are no longer in the light blue stable region: for a higher percentage of T_D we need a stronger electric current. Indeed, if T_D gets larger it means the system has more time to diverge (fall down) and in order to bring it back up we need a stronger electromagnetic field and thus a higher value of the electrical current I (Fig 2.11).

We follow the same protocol described previously for the case $T_D = 25\%T$. The only difference is that for this experimental study we use $I = 0.55\text{ A}$ (the maximum experimental value for I). The different values of (γ_0, η) experimentally observed are shown in Fig 2.29. White squares represent stable responses and black crosses represent unstable responses. The values of (γ_0, η) over the red curve as well from the stability region (light blue) do stabilize the system (white squares in Fig 2.29.a). However, when we step out of the region the inverted pendulum falls down, the system is no longer stabilized (black crosses in Fig 2.29.a.) We observe a perfect agreement between the experiments and the theoretical stability regions.

Figure 2.29 b) presents two different experimental stabilization showing we can stabilize the system using a large percentage of T_D . We also observe the response does one oscillation, characteristic of the mode appearing in the first stability region as observed in Fig 2.20. For the top experimental response in Fig 2.29.b the period of modulation is $T = 0.12\text{s}$ and for the bottom experimental response in Fig 2.29.b the period of modulation is $T = 0.15\text{s}$.

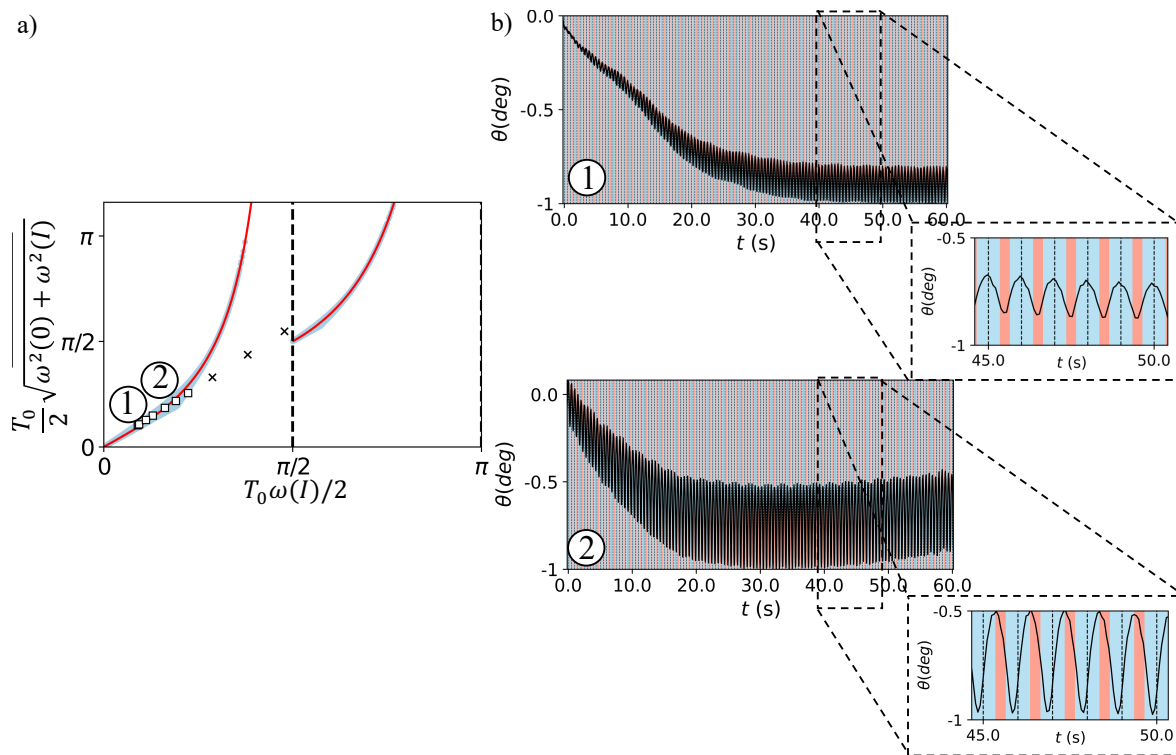


Figure 2.29: First two theoretical master curves of Eq (2.14) with the light blue region corresponding to the stability region accepted for $\mathcal{T}_D = 70\%2\pi$. White squares are the experimental stable responses for $T_D = 70\%T$. Black crosses are the chosen (γ_0, η) outside of the region and in fact do not stabilize the system. b) Two experimental stable responses enumerated 1 and 2 in the diagram. Point 1 has the experimental parameters $I = 0.55\text{A}$, $T_O = 36\text{ ms}$ and $T_D = 85\text{ms}$. Inset shows the response has the shape of the mode 1. Point 2: experimental parameters $I = 0.55\text{A}$, $T_O = 45\text{ ms}$ and $T_D = 106\text{ ms}$. Inset shows a mode 1 shape.

The natural period of the system is $T_0 = 0.57\text{s}$, so we show again that we are using periods of modulation of the same order as the natural time scale of the system. Showing once more and proving that with this new approach we are stabilizing no longer using the Kapitza approach. We can stabilize a natural unstable system doing a synchronized dynamic stabilization.

Finally we observed that the experimental point in the second stability region in Fig 2.28.a had the period of modulation closest to the natural time scale of the system and this particular point is the highest point studied in the master curves. Showing us that to have a period of modulation closest to the natural time scale of the system you do not only need large values of T_D but you also need large values of γ_0 . Experimentally, $T_D = 70\%T$ is the maximum percentage we were able to achieve to dynamical stabilize the system and these experimental points are the highest we could achieve to go in the master curves. This means we are letting the system stay a longer time per period in its natural state and sending an “impulse” of electrical energy during 30% of each period. Without the master curves for an electrical current of $I = 0.48\text{A}$ we achieved a maximum stabilization for $T_D = 40\%T$ and this gives an electrical energy spend of $E_{elec} = 3.2\text{ W.h}$. With the master curves we used a higher electrical current $I = 0.55\text{A}$ but we achieved a maximum stabilization for

$T_D = 70\%T$ and this gives an electrical energy spend of $E_{elec} = 2.1$ W.h.

So, using these discrete number of pseudo-analytical master curves defined in Eq (2.14) does not only let us deduce the experimental values of T_O to stabilize the system while having T_D the highest possible, it also let us stabilize the system with a period of modulation closer to the natural time scale of the system and the stabilization is more energy efficient. In Fig 2.28 and Fig 2.29 we presented the maximum values we could reach in the dimensionless space (γ_0, η) . We are limited by the electrical current we can use and by the geometry of the system. We believe that with another setup build to explore these master curves it can be possible to go at higher percentages of T_D and reach larger values in the master curves at the macroscopic scale. As a result, we will be able to improve the shape of the experimental responses, having better exponentials during T_D and cleaner oscillations during T_O . But also, explore new responses with this approach of synchronized dynamic stabilization, which now is an alternative to the fast frequency approach.

3 | Conclusions & perspectives

In this thesis, to obtain new physical insights on parametric instabilities we conducted an experimental and theoretical study. The first studied aspect of parametric instabilities was their use as parametric amplifiers. This involved understanding the current macroscopic limitations making us to use them only at the tip of the instability tongues. We then developed and validated a new concept to experimentally trigger high order parametric resonance and to fully control them using an original geometric relation. The second aspect of the investigation dealt with the dynamical stabilization of a system using parametric pumping. An experimental proof of concept coupled with numerical simulations and a physical comprehension of the core of the phenomenon lead to the development of a pseudo-analytical approach to dynamically stabilize a naturally unstable equilibrium. With this approach, the periods of modulations can be close to the natural time scale of the system, proposing an alternative to the current Kapitza's approach.

Parametric resonance

In the first part of the thesis, a new concept to control parametric instabilities at the macroscopic scale is presented. The proposed concept is to have a system where its natural time scale can be strongly varied in a simple manner and without modifying the geometry. To achieve this, the component providing the modulation must be symmetrically placed outside of the main mechanical setup whose responses will be amplified.

The system used as a proof of concept is an electromagnetic pendulum (Fig 3.1.a). The natural frequency of the pendulum can be drastically changed by the electromagnetic field which is controlled by the electrical current I and its evolution is characterized by the scalar $\omega(I)$ (Fig 3.1.b). With this control parameter I , it is even possible to have a diverging response after a critical value I_c , physically meaning the system is on a potential with a negative curvature (red curves in Fig 3.1.b).

By periodically modulating the electrical current I with a T -periodic square wave modulation function, it has been possible to trigger and observe high order parametric resonances (green crosses in Fig 3.2). Rationalizing the physical responses of this parametric oscillator led us to predict the location of the instabilities tongues in the modulation space (grey dots in Fig 3.2). We are no longer at the tip of the classic regions (inset in Fig 3.2), we can now explore large periods and high amplitudes of modulations. In particular it is interesting to highlight that we were able to trigger the 36th instability region at the macroscopic scale. An achievement since, to our knowledge, the record was the 28th region observed in a MEMS in 2016 [73].

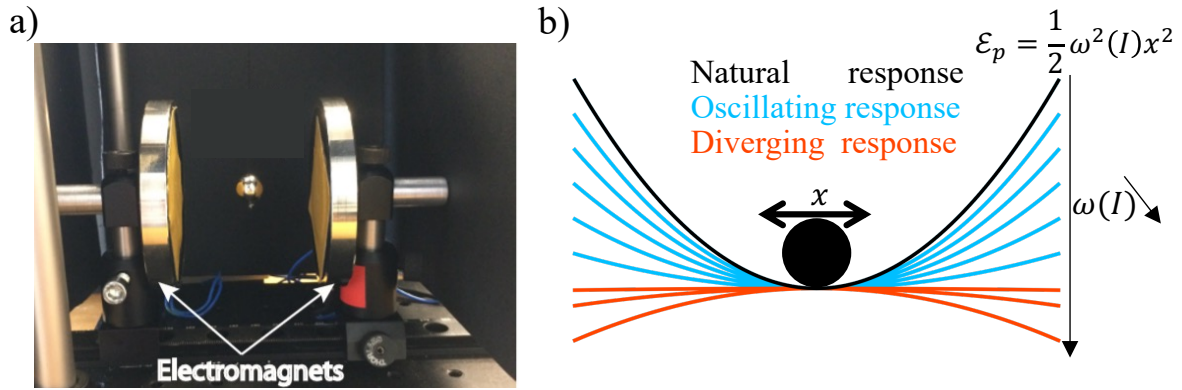


Figure 3.1: Proof of concept to better control parametric instabilities. a) Electromagnetic pendulum: a metallic marble is symmetrically placed in the middle of two attracting electromagnets controlled by the electrical current I and modulated by a T -periodic square wave function. b) Sketch of the evolution of the curvature of the potential energy \mathcal{E}_p of the linear pendulum characterized by the scalar $\omega(I)$. Black line is the natural state ($I = 0$). Blue lines are oscillating responses ($I < I_c$) and red lines are diverging responses ($I > I_c$).

Lastly, the idea of sending an “impulse” train instead of sending the classical square wave modulation was analyzed. This type of modulation can be relevant because the response of the system will be triggered using less amount of energy than a traditional modulation. Using our experimental system in Fig 3.1.a we were able to observe the outcome of this type of signal. With the experimental “impulse” train we were able to enhance the amplitude of oscillations of the electromagnetic pendulum and once at the permanent regime the system enters a limit cycle where the frequency of oscillation corresponds to the natural frequency of the pendulum. We were able to trigger a “natural oscillation” using parametric instabilities and using a low amount of electrical energy.

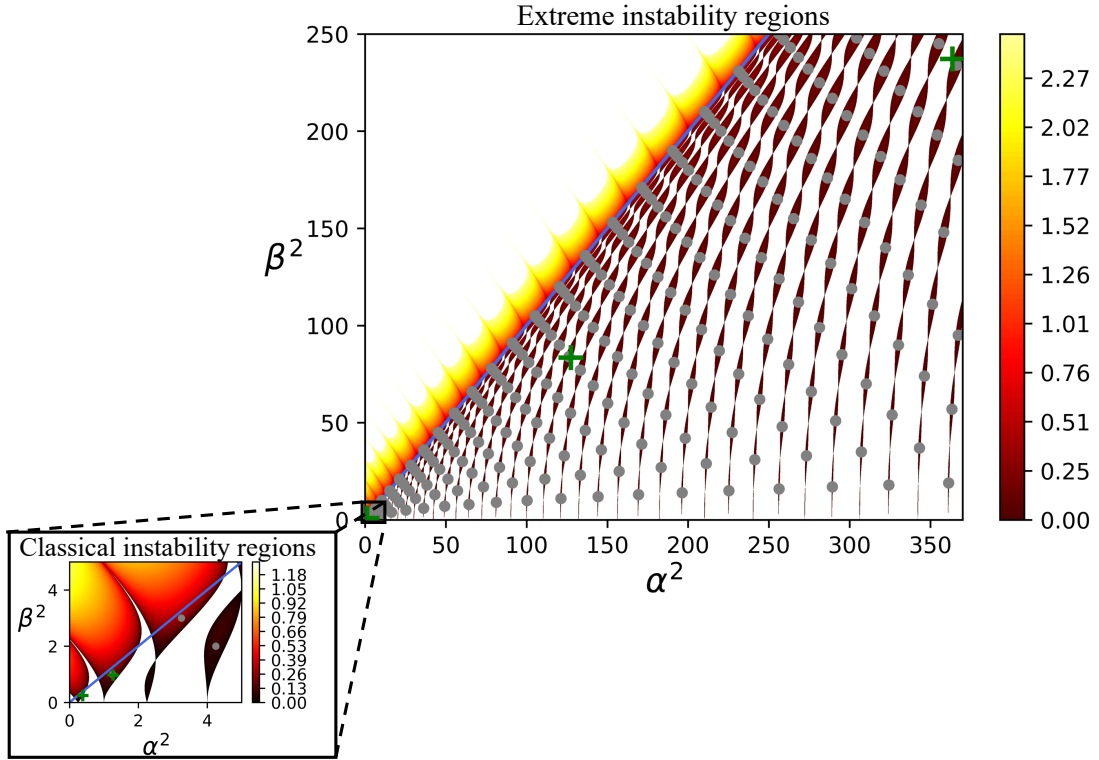


Figure 3.2: Beyond the tip of the parametric instability tongues. Stability diagram of the Meissner equation showing the evolution of the maximum value of the real part of the Floquet exponent up to 2.3 in the extremely extended (α^2, β^2) space. Gray dots (m, n) represent a new discrete geometrical relation to be at each instability pocket. Inset zooms on the classic first instability regions. Green crosses represent the instability regions reached experimentally.

Dynamical stabilization

In the second chapter of the thesis, we get new physical insights in dynamical stabilization. Unlike parametric resonance, dynamical stabilization focuses on the stability regions of the stability diagram. We revisit the concept presented by Kapitza where stabilization can be achieved if the frequency of modulation is faster than the natural time scale of the system[65]. This approach is limiting us to the bottom edge of the first stability region. An experimental and numerical proof of concept is developed to show that it is possible to stabilize a system with a driven frequency closer to the natural time scale of a naturally diverging system developing the idea of synchronized dynamical stabilization.

An experimental setup was developed to understand and observe dynamical stabilization. The system is a planar inverted pendulum with a metallic marble symmetrically placed under an attracting electromagnet whose attracting force depends on the imposed electrical current I (Fig 3.3.a). Same as before, the electromagnetic field is an efficient tool to drastically modify the natural time scale of the perturbed response and is characterized with the scalar $\omega(I)$. This time the increase of the electrical current tends to stabilize the vertical unstable equilibrium and for a critical value I_c , the system changes to an oscillatory state. Physically this can be interpreted as a change of the curvature of the potential energy varying from a negative curvature (divergent) to a positive curvature (oscillatory) (Fig 3.3.b).

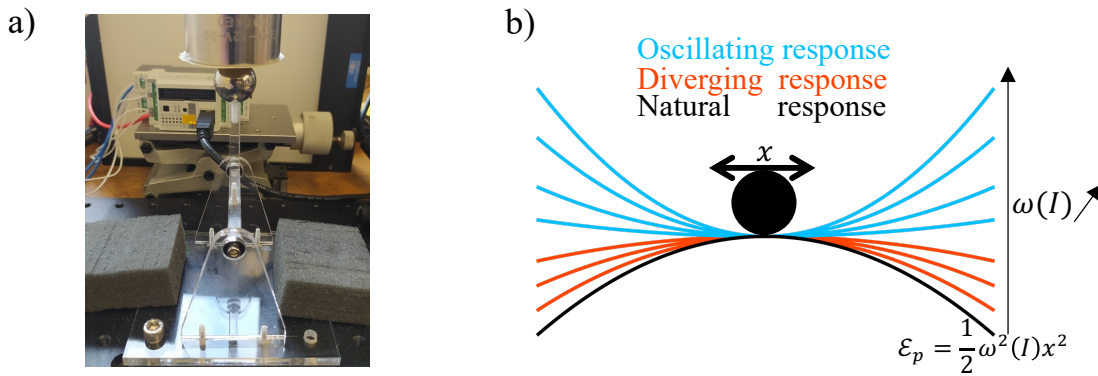


Figure 3.3: Proof of concept to dynamically stabilize a system beyond the Kapitza approach. a) Electromagnetic inverted pendulum: a metallic marble is symmetrically placed under an attracting electromagnet controlled by the value of the electrical current I . b) Sketch of the evolution of the curvature of the potential energy of the linear inverted pendulum characterized by the scalar $\omega(I)$. Black line is the natural unstable state ($I = 0$). Red lines are diverging responses ($I < I_c$) and blue lines are oscillating responses ($I > I_c$).

By periodically modulating the electromagnetic pendulum with a $(T_D + T_O)$ -periodic square wave modulation function, it has been possible to stabilize a naturally unstable equilibrium with a period of modulation close to the natural time scale of the system (Fig 3.4), proving that a synchronized dynamic stabilization can be possible by spending more time in the natural unstable state during T_D and sending short periods of electrical energy during T_O . Figure 3.4 shows that this new approach is possible and does not limit us to the first stability region since we achieved stabilization up to the fifth stability region.

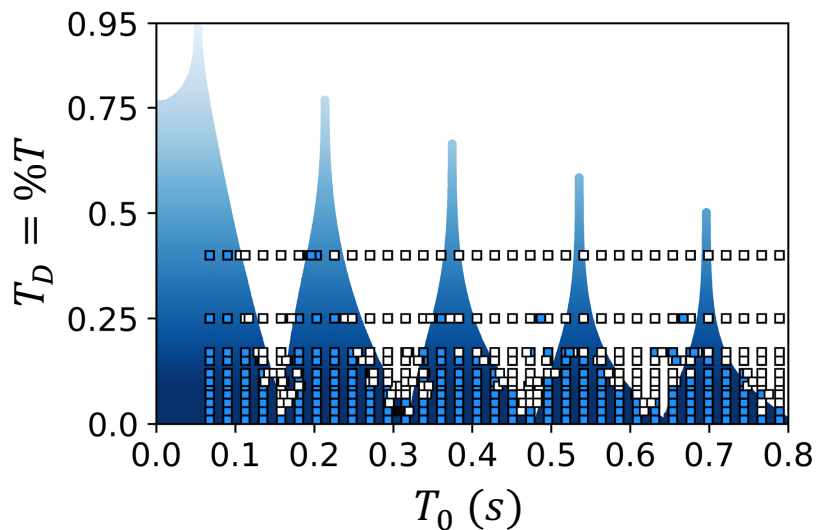


Figure 3.4: Experimental dynamical stabilization of a natural unstable system with frequencies of modulation close to the time scale of the system and reaching beyond the first stability region. Blue squares are experimental stable responses and white squares are experimental unstable responses.

By ways of a numerical study, we showed that to reach higher values of T_D we can use an analogy between initial and boundary value problems. With this approach we can develop pseudo-analytical master curves to predict the parameters to dynamically stabilize a system (Fig 3.4) and deduce the experimental values of T_O at a fixed electrical current I to stabilize the inverted pendulum for even higher values of T_D (Fig 3.5). We achieved a stabilization of $T_D = 70\%T$ with a period of modulation of the same order as the natural time scale of the system ($T = 0.15\text{s}$ and $T_0 = 0.57\text{s}$).

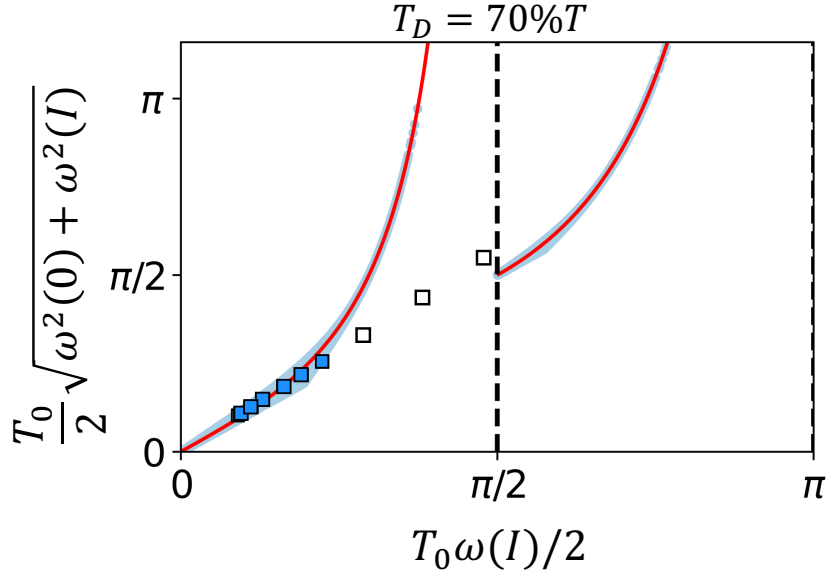


Figure 3.5: Dimensionless pseudo-analytical master curves (in red) deduced by approximating the response of the system to a fundamental unit cell. Blue and white squares represent stable and unstable experimental observations respectively. We achieved stabilization for $T_D = 70\%T$ with T the period of modulation.

Thus, we can now navigate the entirety of the stability regions in a simpler way. Instead of having a continuous diagram, we have a discrete number of pseudo-analytical curves to deduce the parameters to stabilize a system for any value of T_D . They are a new powerful tool to explore synchronized dynamical stabilization with frequencies of modulations closer to the natural time scale of the system and decreases the energy consumption for stabilization.

Perspectives

We hope our work will bring some useful insights to further studies on the control of parametric instabilities. We believe the adaptability of the presented experiments and the wide range of physical domains to which one can apply these ideas (any dynamical system with a natural time scale which could be periodically varied) makes it a formidable tool not only for research but for teaching too. In this section, we discuss a potential application for MEMS. We open the discussion to different approaches to continue the study. We propose one experimental setup to explore the idea of a system with multiple degrees of freedom under a periodic modulation. Then, we introduce an idea for an experimental setup to explore a system with one degree of freedom capable to be under multiple shapes of the same periodic modulation function.

Possible MEMS application

Concerning parametric resonance, as mentioned previously in the manuscript, a very good candidate to take advantage of our validated theory to control the instability regions are MEMS. For systems like MEMS that are tiny membranes with enormous Q factors (because they operate in Ultra High Vacuum) and driven by periodic electrostatic fields, an application of this particular parametric pumping could allow to efficiently generate highly super-harmonic sinusoidal signals with extremely tunable fundamental frequencies. A first experimental setup at the microscopic scale is developed by the team at the Laboratory for Analysis and Architecture of Systems (LAAS-CNRS) in Toulouse (Fig 3.6). They are adapting our experimental approach to their system: they symmetrically positioned a MEMS between two plates creating an electrostatic field to enhance and control extreme parametric modulations.

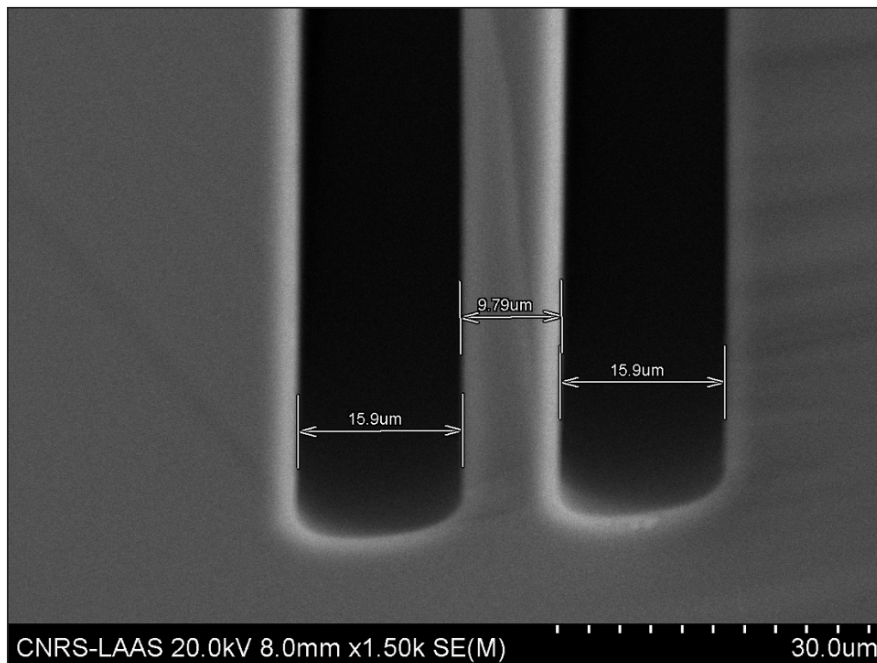


Figure 3.6: Photograph of a preliminary MEMS setup using a symmetric electrostatic fields to enhance and control the response. Image credit: LAAS-CNRS, L.Nicu and F. Mathieu.

Multi-body system under parametric modulation

Our model and theoretical design rules (for either parametric resonance or dynamical stabilization) were obtained for a system with one degree of freedom. We wonder if they are still valid for a system with multiple degrees of freedom. To investigate it, we propose to place a series of electromagnetic pendulums which metallic marbles are attached to the same beam (Fig 3.7). By changing the geometry of the beam we can change the coupling between the pendulums: the more flexible the beam the more coupled the pendulums will be.

With this setup, it could be interesting to study the transfer of information between pendulums by varying the geometrical parameters (for instance the thickness of the beam) and

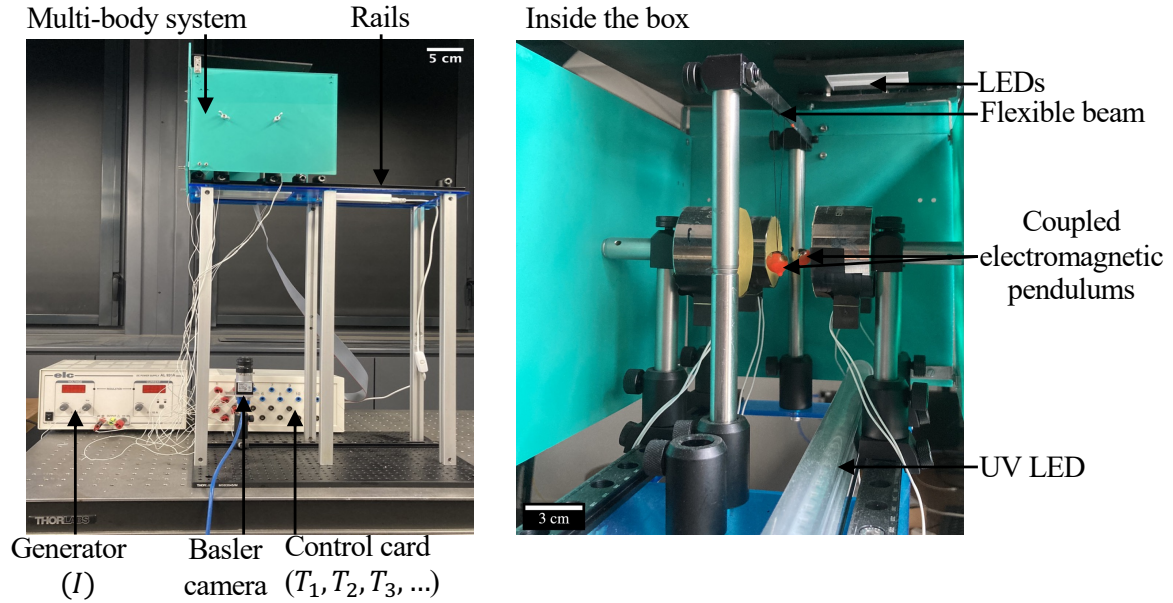


Figure 3.7: Preliminary experimental setup to study parametric instabilities in a multi-body system. Two electromagnetic pendulums coupled through a beam inside a black box for recording their motion. They are painted with fluorescent light and illuminated with a violet light.

thus observe the role of the coupling on the responses. If we send the same periodic modulation to the pendulums, do we trigger the expected instability mode? Do they enter the expected limit cycle? If they do, do they reach it at the same time? What is the impact of the number of pendulums for the previous questions? Lastly this system could be adapted to study the dynamical stabilization of a multi-body systems by exchanging the pendulums with inverted pendulums.

Finally, if we have multiple coupled pendulums and send a random signal, to be sure they are not in phase lock, could the pendulums exchange information to adapt their motions and enter a particular state? If they do enter a given particular state, could this system be use to observe the particular behaviour of a Floquet time crystal in a macroscopic system [50, 99, 100]? Of course, the coupled pendulums had an energy input to trigger the response, but at one point if they enter this “organized” state and the electromagnets are turned OFF, they could be in a state that has a motion “without energy”. Could they be seen as masses arranged periodically in both space and time? We think this would be an exciting approach to take for the study of a multi-body system under a periodical modulation function.

Multi-shaped modulation function

With our study, we were able to control and observe the shape of the response for one modulation function. However, we do not know what happens if we send a T_1 -periodic modulation function followed by a T_2 -periodic modulation function. Will the total response be the sum of the two modes corresponding to each modulation function or will a new response appear? We propose an experimental concept to explore this new question. The system is a metallic

marble symmetrically placed between a Helmholtz coil which is powered by two generators connected to a control card (Fig 3.8). With the control card we can send different periodic modulations functions at once and the multiple generators provide different intensities, i.e different thresholds, for the modulation functions. Finally, the Helmholtz coil will provide the possibility to use an attracting or repulsing electromagnetic field on the metallic marble.

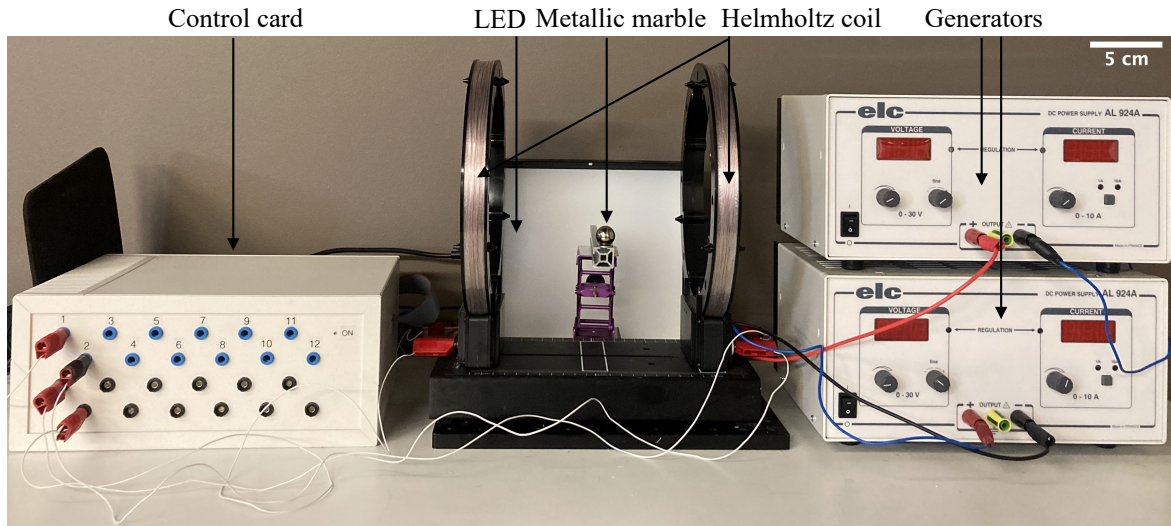


Figure 3.8: Preliminary experimental setup to study a one degree of freedom system under multiple shapes of the same modulation function. The system is a metallic marble symmetrically placed between a Helmholtz coil connected to a control card capable to send different periods of modulations functions. The multiple generators are used to have different intensities to be able to have different thresholds on the multiple modulations functions.

This system can still be seen as a mass trapped in a potential, only this time there are various potentials. The pseudo-analytical master curves we deduced to obtain the parameters to stabilize a natural unstable equilibrium came from an analogy with a quantum mechanics problem. We propose a similar approach to obtain the solution of this new problem, this time using the concept of quantum superposition. Quantum superposition is a property that affirms that quantum states can be added (“superposed”) and the result will be another valid quantum state. For the problem of a particle trapped in a potential, the quantum states are the eigenfunctions solution of the stationary Schrödinger equation. At the macroscopic scale, these eigenfunctions could represent a corresponding mode for this new system. If we add two or more different T -periodic square waves modulations, could the response be the sum of the corresponding eigenfunctions? Could we deduce the response of the system directly using this property instead of having to solve them numerically?

There have been various quantum analogs observed at the macroscopic scale. For example the use of the quantum harmonic oscillator at the macroscopic scale [101], similar observation of the phenomenon of quantum tunneling [102], the phenomenon of interference [44, 103] and the quantization of classical orbits [43]. We wonder if this new experimental setup could add quantum superposition to this list.

BIBLIOGRAPHY

- [1] I. Newton. *The Principia: mathematical principles of natural philosophy*. Univ of California Press, 1999.
- [2] H. Poincaré. Mémoire sur les courbes définies par une équation différentielle (i). *Journal de mathématiques pures et appliquées*, 7:375–422, 1881.
- [3] S.H. Strogatz. *Nonlinear Dynamics and Chaos*. Perseus Books, 1994.
- [4] E. Lorenz. Deterministic nonperiodic flow. *Journal of atmospheric sciences*, 20(2):130–141, 1963.
- [5] P. Holmes. Poincaré, celestial mechanics, dynamical-systems theory and “chaos”. *Physics Reports*, 193(3):137–163, 1990.
- [6] D. Aubin and A.D. Dalmedico. Writing the history of dynamical systems and chaos: Longue durée and revolution, disciplines and cultures. *Historia Mathematica*, 29(3):273–339, 2002.
- [7] L. A. Godoy. Buckling of vertical oil storage steel tanks: Review of static buckling studies. *Thin-Walled Structures*, 103:1–21, 2016.
- [8] D. Green and W. G Unruh. The failure of the Tacoma bridge: A physical model. *American journal of physics*, 74(8):706–716, 2006.
- [9] BBC NEWS. New-zealand oil ship leak raises questions, 9 october 2011. *BBC NEWS*, 2011.
- [10] P. Harper, H. Donnell, J. Morton, M. Theunissen, and I. Davison. Worst ever environmental disaster. *New Zealand Herald*, 2011.
- [11] S. Timoshenko. History of strength of materials. reprint 1983, 1953.
- [12] S. Timoshenko. On the correction for shear of the differential equation for transverse vibrations of prismatic bars. *The London, Edinburgh, and Dublin Philosophical Magazine and Journal of Science*, 41(245):744–746, 1921.
- [13] S. Timoshenko. On the transverse vibrations of bars of uniform cross-section. *The London, Edinburgh, and Dublin Philosophical Magazine and Journal of Science*, 43(253):125–131, 1922.
- [14] G. Domokos and P. Holmes. Euler’s problem, Euler’s method, and the standard map; or, the discrete charm of buckling. *Journal of Nonlinear Science*, 3(1):109–151, 1993.

- [15] J. Tomblin and E. Barbero. Local buckling experiments on FRP columns. *Thin-Walled Structures*, 18(2):97–116, 1994.
- [16] N. Hu, K. Nunoya, D. Pan, T. Okabe, and H. Fukunaga. Prediction of buckling characteristics of carbon nanotubes. *International Journal of Solids and Structures*, 44(20):6535–6550, 2007.
- [17] G-F Wang and X-Q Feng. Timoshenko beam model for buckling and vibration of nanowires with surface effects. *Journal of physics D: applied physics*, 42(15):155411, 2009.
- [18] A. Larsen. Aerodynamics of the Tacoma narrows bridge-60 years later. *Structural Engineering International*, 10(4):243–248, 2000.
- [19] J.R. Wright and J. E. Cooper. *Introduction to aircraft aeroelasticity and loads*, volume 20. John Wiley & Sons, 2008.
- [20] T. E. Noll, J. M. Brown, M. E. Perez-Davis, S. D. Ishmael, G.C. Tiffany, and M. Gaier. Investigation of the Helios Prototype Aircraft Mishap. *Volume I Mishap Report*, I(January):100, 2004.
- [21] C. Nitschke, A. Vincenti, and J-C. Chassaing. Influence of stochastic perturbations of composite laminate layups on the aeroelastic flutter of a cantilevered plate wing. *Composite Structures*, 220:809–826, 2019.
- [22] M. Montemurro, A. Vincenti, and P. Vannucci. A two-level procedure for the global optimum design of composite modular structures—application to the design of an aircraft wing. *Journal of Optimization Theory and Applications*, 155(1):24–53, 2012.
- [23] International Maritime Organization. Revised Guidance to the master for avoiding dangerous situations in adverse weather and sea conditions. 2007.
- [24] Y. Cai, Y. Wen, and Liji. Wu. Ship route design for avoiding heavy weather and sea conditions. *TransNav: International Journal on Marine Navigation and Safety of Sea Transportation*, 8, 2014.
- [25] N. Umeda, M. Hamamoto, Y. Takaishi, Y. Chiba, A. Matsuda, W. Sera, S. Suzuki, K. Spyrou, and K. Watanabe. Model experiments of ship capsizing in astern seas. *Journal of the Society of Naval Architects of Japan*, 1995(177):207–217, 1995.
- [26] B. C. Chang. On the parametric rolling of ships in regular seas using a numerical simulation method. *9th International Conference on Fast Sea Transportation, FAST 2007*, 35:447–457, 2007.
- [27] K. Bertoldi, P.M. Reis, S. Willshaw, and T. Mullin. Negative Poisson’s ratio behavior induced by an elastic instability. *Advanced materials*, 22(3):361–366, 2010.
- [28] J. Shim, C. Perdiguou, E.R. Chen, K. Bertoldi, and P.M. Reis. Buckling-induced encapsulation of structured elastic shells under pressure. *Proceedings of the National Academy of Sciences*, 109(16):5978–5983, 2012.

- [29] N. Hu and R. Burgueño. Tailoring the elastic postbuckling response of cylindrical shells: A route for exploiting instabilities in materials and mechanical systems. *Extreme Mechanics Letters*, 4:103–110, 2015.
- [30] A. Lazarus and P.M. Reis. Soft actuation of structured cylinders through auxetic behavior. *Advanced Engineering Materials*, 17(6):815–820, 2015.
- [31] L. Du Peloux, O. Baverel, J-F. Caron, and F. Tayeb. From shape to shell: a design tool to materialize freeform shapes using gridshell structures. In *Design Modelling Symposium Berlin*, 2013.
- [32] P.M. Reis, F. López Jimenez, and J. Marthelot. Transforming architectures inspired by origami. *Proceedings of the National Academy of Sciences*, 112(40):12234–12235, 2015.
- [33] A. Rafsanjani and K. Bertoldi. Buckling-induced kirigami. *Physical review letters*, 118(8):084301, 2017.
- [34] K. Miura. Method of packaging and deployment of large membranes in space. *The Institute of Space and Astronautical Science report*, 618:1–9, 1985.
- [35] N. Bowden, S. Brittain, A.G. Evans, J.W. Hutchinson, and G.M. Whitesides. Spontaneous formation of ordered structures in thin films of metals supported on an elastomeric polymer. *nature*, 393(6681):146–149, 1998.
- [36] J. Panetta, F. Isvoranu, T. Chen, E. Siéfert, B. Roman, and M. Pauly. Computational inverse design of surface-based inflatables. *ACM Transactions on Graphics (TOG)*, 40(4):1–14, 2021.
- [37] J. Marthelot, E.F Strong, P.M. Reis, and P-T Brun. Designing soft materials with interfacial instabilities in liquid films. *Nature communications*, 9(1):1–7, 2018.
- [38] E. Siéfert, E. Reyssat, J. Bico, and B. Roman. Bio-inspired pneumatic shape-morphing elastomers. *Nature materials*, 18(1):24–28, 2019.
- [39] S. Zaliasl, J.C. Salvia, G.C. Hill, L. Chen, K. Joo, R. Palwai, N. Arumugam, M. Phadke, S. Mukherjee, H-C. Lee, et al. A 3 ppm $1.5 \times 0.8 \text{ mm}^2$ $1.0 \mu\text{a}$ 32.768 khz mems-based oscillator. *IEEE Journal of Solid-State Circuits*, 50(1):291–302, 2014.
- [40] O. Peretz and A.D. Gat. Forced vibrations as a mechanism to suppress flutter—An aeroelastic Kapitza’s pendulum. *Journal of Fluids and Structures*, 85:138–148, February 2019.
- [41] R.F. Wuerker, H. Shelton, and R.V. Langmuir. Electrodynamic containment of charged particles. *Journal of Applied Physics*, 30(3):342–349, 1959.
- [42] S. Protiere, A. Boudaoud, and Y. Couder. Particle–wave association on a fluid interface. *Journal of Fluid Mechanics*, 554:85–108, 2006.
- [43] E. Fort, A. Eddi, A. Boudaoud, J. Moukhtar, and Y. Couder. Path-memory induced quantization of classical orbits. *Proceedings of the National Academy of Sciences*, 107(41):17515–17520, 2010.

- [44] Y. Couder and E. Fort. Single-particle diffraction and interference at a macroscopic scale. *Physical Review Letters*, 97(15):154101, 2006.
- [45] Newtonian labs. <http://newtonianlabs.com/eit/LinearTrapLine.html>.
- [46] J.A. Richards. *Analysis of periodically time-varying systems*. Springer Science & Business Media, 2012.
- [47] M. Faraday. On a peculiar class of acoustical figures; and on certain forms assumed by groups of particles upon vibrating elastic surfaces. *Philosophical transactions of the Royal Society of London*, 121:299–340, 1831.
- [48] É. Mathieu. Mémoire sur le mouvement vibratoire d’une membrane de forme elliptique. *Journal de mathématiques pures et appliquées*, 13:137–203, 1868.
- [49] W.B. Case. The pumping of a swing from the standing position. *American Journal of Physics*, 64(3):215–220, 1996.
- [50] F. Wilczek. Quantum time crystals. *Physical Review Letters*, 109(16), 2012.
- [51] G.W. Hill. On the part of the motion of the lunar perigee which is a function of the mean motions of the sun and moon. *Acta mathematica*, 8(1):1–36, 1886.
- [52] W. Magnus and S. Winkler. *Hill’s equation*. Courier Corporation, 2013.
- [53] E. Meissner. Ueber schüttelerscheinungen in systemen mit periodisch veränderlicher elastizität. *Schweizerische Bauzeitung*, 72(11):95–98, 1918.
- [54] G. Floquet. Sur les équations différentielles linéaires à coefficients périodiques. 12:47–88, 1883.
- [55] R.A. Calico and W.E. Wiesel. Control of time-periodic systems. *Journal of Guidance, Control, and Dynamics*, 7(6):671–676, 1984.
- [56] B. J. Bentvelsen. *Modal analysis of structures in time-periodic elastic state*. PhD thesis, Sorbonne Université, 2018.
- [57] A. Lazarus. *Influence des défauts sur le comportement vibratoire linéaire des systèmes tournant*. Theses, Ecole Polytechnique, December 2008.
- [58] A.M. Lyapunov. Problème général de la stabilité du mouvement, Kharkov 1892, french translation in AA Fac. Sci. Univ. Toulouse 9, 1907; reproduced in *ANN. Math. Studies*, 17, 1907.
- [59] E.L. Ince. IV.-Researches into the characteristic numbers of the Mathieu equation. *Proceedings of the Royal Society of Edinburgh*, 46:20–29, 1927.
- [60] B. Van der Pol and M.J. Strutt. On the stability of the solutions of Mathieu’s equation. *The London, Edinburgh, and Dublin Philosophical Magazine and Journal of Science*, 5(27):18–38, 1928.
- [61] N.W. McLachlan. Theory and application of Mathieu function. 1947.

-
- [62] I. Kovacic, R. Rand, and S. Mohamed Sah. Mathieu's equation and its generalizations: overview of stability charts and their features. *Applied Mechanics Reviews*, 70(2), 2018.
- [63] Y Jia, J Yan, K Soga, and A A Seshia. Multi-frequency operation of a MEMS vibration energy harvester by accessing five orders of parametric resonance. *Journal of Physics: Conference Series*, 476:012126, dec 2013.
- [64] A.V. Arefiev, B.N. Breizman, M. Schollmeier, and V.N. Khudik. Parametric amplification of laser-driven electron acceleration in underdense plasma. *Phys. Rev. Lett.*, 108:145004, Apr 2012.
- [65] P.L. Kapitza. Dynamic stability of a pendulum when its point of suspension vibrates. *Sov. Phys. JETP*, page 588–597, 1951.
- [66] H. J. T. Smith and J. A. Blackburn. Experimental study of an inverted pendulum. *American Journal of Physics*, 60(10):909–911, oct 1992.
- [67] W. Paul. Electromagnetic traps for charged and neutral particles. *Reviews of modern physics*, 62(3):531, 1990.
- [68] J.R. Sanmartín. O Botafumeiro: Parametric pumping in the Middle Ages. *American Journal of Physics*, 52(10):937–945, 1984.
- [69] Sir G. Taylor. The stability of the plane free surface of a liquid in vertical periodic motion. *Proceedings of the Royal Society of London. Series A. Mathematical and Physical Sciences*, 225(1163):505–515, 1954.
- [70] S. Douady. Experimental study of the Faraday instability. *Journal of Fluid Mechanics*, 221:383–409, 1990.
- [71] S. Protière. Gouttes rebondissantes: une association onde-particule à échelle macroscopique. *Dynamique des Fluides [physics.flu-dyn]. Université Paris-Diderot - Paris VII, Français.*, 2007.
- [72] K.L. Turner, S.A. Miller, P.G. Hartwell, N.C. MacDonald, S.H. Strogatz, and S.G. Adams. Five parametric resonances in a microelectromechanical system. *Nature*, 396(6707):149–152, 1998.
- [73] Y. Jia, S. Du, and A.A. Seshia. Twenty-Eight Orders of Parametric Resonance in a Microelectromechanical Device for Multi-band Vibration Energy Harvesting. *Scientific Reports*, 6(July):1–8, 2016.
- [74] P. Roura and J.A. González. Towards a more realistic description of swing pumping due to the exchange of angular momentum. *European journal of physics*, 31(5):1195, 2010.
- [75] M.H. Asadian, S. Askari, and A.M. Shkel. An ultrahigh vacuum packaging process demonstrating over 2 million Q-factor in MEMS vibratory gyroscopes. *IEEE sensors letters*, 1(6):1–4, 2017.

- [76] A. A Grandi, S. Protière, and A. Lazarus. Enhancing and controlling parametric instabilities in mechanical systems. *Extreme Mechanics Letters*, 43:101195, 2021.
- [77] C. Sato. Correction of Stability Curves in Hill-Meissner’s Equation. *Mathematics of Computation*, 20(93):98, 1966.
- [78] B. Apffel, F. Novkoski, A. Eddi, and E. Fort. Floating under a levitating liquid. *Nature*, 585(7823):48–52, 2020.
- [79] P.H. Dawson. *Quadrupole mass spectrometry and its applications*. Elsevier, 1976.
- [80] S. M. Brewer, J.-S. Chen, A. M. Hankin, E. R. Clements, C. W. Chou, D. J. Wineland, D. B. Hume, and D. R. Leibbrandt. $^{27}\text{Al}^+$ quantum-logic clock with a systematic uncertainty below 10^{-18} . *Phys. Rev. Lett.*, 123:033201, Jul 2019.
- [81] H. C. Corben and P. Stehle. *Classical Mechanics: 2nd Edition*. 1994.
- [82] A. Stephenson. On a new type of dynamical stability. *Mem. Proc. Manch. Lit. Phil. Sci.*, 52:1–10, 1980.
- [83] Lord Rayleigh. Investigation of the character of the equilibrium of an incompressible heavy fluid of variable density. *Proceedings of the London mathematical society*, 1(1):170–177, 1882.
- [84] D.J. Lewis. The instability of liquid surfaces when accelerated in a direction perpendicular to their planes.II. *Proceedings of the Royal Society of London. Series A. Mathematical and Physical Sciences*, 202(1068):81–96, 1950.
- [85] E.I. Butikov. On the dynamic stabilization of an inverted pendulum. *American Journal of Physics*, 69(7):755–768, 2001.
- [86] The Royal Swedish Academy of Sciences. Press release: The Nobel Prize in Physics 1989 to Norman F. Ramsey, Hans G. Dehmelt and Wolfgang Paul. <https://www.nobelprize.org/prizes/physics/1989/press-release/>.
- [87] G. Nogues, A. Rauschenbeutel, S. Osnaghi, M. Brune, J-M. Raimond, and S. Haroche. Seeing a single photon without destroying it. *Nature*, 400(6741):239–242, 1999.
- [88] Jean-Michel Raimond, M Brune, and Serge Haroche. Manipulating quantum entanglement with atoms and photons in a cavity. *Reviews of Modern Physics*, 73(3):565, 2001.
- [89] C. Monroe, D.M. Meekhof, B.E. King, and D.J. Wineland. A “Schrödinger cat” superposition state of an atom. *Science*, 272(5265):1131–1136, 1996.
- [90] D. Leibfried, R. Blatt, C. Monroe, and D. Wineland. Quantum dynamics of single trapped ions. *Reviews of Modern Physics*, 75(1):281, 2003.
- [91] The Royal Swedish Academy of Sciences. Press release: The Nobel Prize in Physics 2012 to Serge Haroche and David J. Wineland. <https://www.nobelprize.org/prizes/physics/2012/press-release/>.

-
- [92] C. Monroe, D.M. Meekhof, B.E. King, W.M. Itano, and D.J. Wineland. Demonstration of a fundamental quantum logic gate. *Physical review letters*, 75(25):4714, 1995.
- [93] R. Blatt and D. Wineland. Entangled states of trapped atomic ions. *Nature*, 453(7198):1008–1015, 2008.
- [94] W.R. Hamilton. Second essay on a general method in dynamics. *Philosophical Transactions of the Royal Society of London*, 125:95–144, 1835.
- [95] A. Messiah. *Quantum mechanics*, volume 1. North-Holland, 1961.
- [96] B.C. Hall. *Quantum theory for mathematicians*, volume 267. Springer, 2013.
- [97] D. Griffiths and D. Schroeter. *Introduction to Quantum Mechanics*. Pearson Prentice Hall, 2005.
- [98] M. Chiani. A chart for the energy levels of the square quantum well. *arXiv*, 2016.
- [99] A. Shapere and F. Wilczek. Classical time crystals. *Physical Review Letters*, 109(16):1–5, 2012.
- [100] D.V. Else, B. Bauer, and C. Nayak. Floquet time crystals. *Physical Review Letters*, 117(9):090402, 2016.
- [101] A. Lazarus. Discrete dynamical stabilization of a naturally diverging mass in a harmonically time-varying potential. *Physica D: Nonlinear Phenomena*, 386-387:1–7, 2019.
- [102] A. Eddi, E. Fort, F. Moisy, and Y. Couder. Unpredictable tunneling of a classical wave-particle association. *Physical review letters*, 102(24):240401, 2009.
- [103] J.W.M. Bush. The new wave of pilot-wave theory. *Physics Today*, 68:47–53, 2015.